Investigation of Magnetic Field Effects on Protein Photochemistry using Cavity Enhanced Spectroscopy

Tilo Zollitsch

St Hugh's College

A thesis submitted for the degree of

Doctor of Philosophy

Physical & Theoretical Chemistry Laboratory

University of Oxford

Trinity Term 2018

Abstract

Investigation of Magnetic Field Effects on Protein Photochemistry using Cavity Enhanced Spectroscopy

Submitted for the degree of *Doctor of Philosophy*
by Tilo M. Zollitsch
St Hugh's College, Trinity 2018

Some animals, such as migratory birds, are known to have the ability to sense and use magnetic fields for orientation. At the heart of this remarkable ability is believed to be a photoinduced chemical reaction taking place within a blue-light receptor protein called cryptochrome (Cry). It is hypothesised that magnetic fields can play a decisive role in determining reaction rates (and, hence, yields) by acting on the spin states of spin correlated radical pairs (RPs) formed between a flavin chromophore and a tryptophan (Trp) electron-transfer (ET) chain within Crys.

In this work, cavity ring-down spectroscopy (CRDS) has been used for the detection of magnetic field effects (MFEs) *via* small changes in the differential absorbance ($\Delta\Delta A \sim 10^{-6}$) of aqueous protein samples, with sub-microsecond time resolution. The photochemistry and effects of magnetic fields on European robin (*Er*) Cry, fruit fly Cry, and a plant Cry are characterised. In a key result for this field of research, an MFE in the photochemistry of *Er*Cry is revealed for the first time, lending considerable support to its proposed involvement in bird magnetoreception. Using Cry mutants with modified Trp ET chains, the role of individual Trps in the manifestation of MFEs was explored. Replacing the terminal (*i.e.* fourth) Trp of the ET chain in *Er*Cry with a redox inert amino acid is shown to significantly increase the optically-detected MFE, indicating that the RP formed between the flavin and the third Trp might be the primarily magnetically sensitive species.

To better understand the relevant biochemical processes in Cry, *de novo* designed artificial flavoproteins (maquettes) have been used to model the photochemistry of Cry (Chapter 4). The comparatively simple and adaptable design of these model proteins facilitates detailed MFE studies by reducing the complexity of natural Cry. In these maquettes, photoinduced ET leads to the formation of a RP which exhibits MFEs analogous to those in Crys. The profound effect of the donor-acceptor distance on the MFE is demonstrated using flavomaquettes with varying flavin-Trp distances.

The application of cavity enhanced spectroscopy to both natural cryptochromes and artificial flavoproteins, opens up new pathways for the detection and characterisation of MFEs in biologically relevant environments. The enhanced sensitivity of these approaches constitutes a significant step forward in understanding the underlying biochemical processes of animal magnetoreception.

Acknowledgments

First and foremost I want to thank my supervisors for the trust they have put in me, providing me with the opportunity to work on this fascinating project. Thank you, Professor Stuart Mackenzie, for all your advice, inspiration, and invaluable support. Thank you for your guidance throughout the last four years, which I will always remember proudly. Thank you, Professor Peter Hore, for all your support. I loved the discussions we had about spin chemistry and always finding your door open when I needed your advice. Thank you Professor Christiane Timmel for all your help, your infectious passion and enthusiasm for science related and unrelated topics, and for making me feel welcome in the Timmel side of the MacTimmel group.

Particular thanks go to Dr Lauren Jarocha. Thank you for helping me make my first steps in science and your valiant and tireless efforts to disentangle the chemistry of *simple* model systems over the last years with me. Thank you, Dr Kevin Henbest, for always being there with a helping hand, be it helping me find my ways on the first day I set foot in the ICL laboratories (and ever since), or sharing your vast experience in working with cryptochromes.

Katie, it has been great working and sharing an office with you. Thank you for sharing the pleasure and pain of looking for tiny quantum effects in noisy biology (good luck with the cells!). Special thanks also goes to my brothers in arms Dr Dean Sheppard and Marcin Konowalczyk, for trying to “square the circle” and perform condensed phase cavity enhanced spectroscopy on proteins with me. Thank you, Dean, for showing me the ropes on how to do CRDS, for sharing all your cavity wisdom over the years, and for the great time we had in India. Thank you, Marcin, for being a great guy to work with and a friend outside the lab as well. Solving riddles with you in the ocean, a Japanese sauna, and elsewhere was definitely a highlight of my time in Oxford. Jessica Walton and Thomas Spearman, I am thankful for your help and company during arguably the most exciting time of my DPhil.

During my last four years I had the great pleasure to meet and work alongside outstanding people: Dr Imogen Parry, Dr Graham Cooper, Dr Dean Sheppard, Dr Andreas Iskra, Dr Alexander Gentleman, Alice Green, Ethan Cunningham, and Hansjochen Köckert, thank you all for a great time and your witty humour that coined life in the Mackenzie office. I feel lucky to have met you.

Thank you, Jinjing Xu, Dr Chris Bialas, Professor Henrik Mouritsen, and Professor Erik Schleicher. I can only imagine how challenging it is to synthesise and purify cryptochromes and artificial proteins. Thank you very much for trusting me with your precious and glorious protein samples.

I want to thank Professor Ulrich Boesl-von Grafenstein and Professor Ueli Heiz for igniting my love for laser spectroscopy and physical chemistry and providing me the scientific foundation to build my DPhil on.

Finally, my biggest thanks go to my family. Laopo, ich kann meine Dankbarkeit kaum in Worte fassen. Danke, dass Du mich immer mit voller Kraft und ganzem Herzen unterstützt, mich motivierst und es mir möglich gemacht hast, etwas Besonderes in meinem Leben zu erreichen. Danke, dass Du immer für mich und unseren Sonnenschein Liya da bist. Mum und Dad, danke, dass ich mich immer auf Euch verlassen kann und Ihr mir alles gebt, was sich ein Sohn wünschen kann.

List of publications

Publications based on work presented in Chapter 4

[1] Zollitsch, T. M.; Jarocha, L. E.; Bialas, C.; Henbest, K. B.; Kodali, G.; Dutton, P. L.; Moser, C. C.; Timmel, C. R.; Hore, P. J.; Mackenzie, S. R.; Magnetically sensitive radical photochemistry of non-natural flavoproteins, *Journal of the American Chemical Society,* DOI 10.1021/jacs.8b03104. Publication Date (Web): June 25, **2018**.

[2] Bialas, C.; Jarocha, L. E.; Henbest, K. B.; Zollitsch, T. M.; Kodali, G.; Timmel, C. R.; Mackenzie, S. R.; Dutton, P. L.; Moser, C. C.; Hore, P. J., Engineering an Artificial Flavoprotein Magnetosensor. *Journal of the American Chemical Society* **2016,** *138* (51), 16584-16587.

Publications based on results presented in Chapter 3 are currently in preparation covering magnetic field effects on the photochemistry of European robin and *Drosophila melanogaster* cryptochrome respectively.

FÜR MENG UND LIYA

Content

Abbreviations

BBCEAS	broadband cavity enhanced absorption spectroscopy
BET	back electron transfer
BLUF	blue-light using FAD
CRDS	cavity ring-down spectroscopy
Cry	cryptochrome
Dm	*Drosophila melanogaster* (common fruit fly)
E. coli	*Escherichia coli*
Er	*Erithacus rubecula* (European robin)
ET	electron-transfer
F	flavin
FAD	flavin adenine dinucleotide
FMN	flavin adenine mononucleotide
H	histidine
His	histidine
HOMO	highest occupied molecular orbital
HT	hydrogen-transfer
ISC	intersystem crossing
L	lumichrome
LFE	low field effect
LOV	light-oxygen-voltage
LUMO	lowest unoccupied molecular orbital
MARY	magnetically altered reaction yield
MFE	magnetic field effect
OCTAS	optical cavity enhanced transient absorption spectroscopy

PL	photolyase
RF	riboflavin
RP	radical pair
S	singlet
SC	spin correlated
SC RP	spin correlated radical pair
SEM	standard error of the mean
T	triplet
TA	transient absorption
Trp	tryptophan
W	tryptophan

Chapter 1.

Introduction

It is a well-known fact that that some animals can sense and use the earth-magnetic field. Famous examples are migratory birds that are known to exploit the earth-magnetic field to navigate during migration.[1-2] But also other animals, such as for example fish,[3] amphibians,[4] and insects[5] have the ability to orient in magnetic fields.

Despite decades of research, the underlying mechanism of magnetoreception in animals is still unclear. What has been puzzling scientists for decades is the notion that a magnetic field as weak as that of the earth (50 μT) can have a significant effect on chemical reactions. The leading theory to explain this remarkable feat is based on a quantum biological effect centred around a spin correlated (SC) radical pair (RP).[6-7] It rationalizes the decisive effect of even weak magnetic fields on reaction yields, by considering the spin dynamic processes involved in radical pair chemistry. Cryptochromes (Cry) have been proposed to host this magnetically sensitive radical pair reaction *in vivo*.

A brief overview of the relevant properties of Cry, a novel protein model system for Cry (maquettes), and the relevant concepts of spin chemistry are provided in this chapter.

1.1 Cryptochromes

Cryptochromes (Cry) belong to a large family of flavoproteins which also comprise light-oxygen-voltage (LOV) proteins and blue-light using FAD (BLUF) proteins. Flavoproteins play key roles in redox reactions of living organisms thanks to the ability of their flavin (F) cofactor to undergo both one- and two-electron-transfer reactions.[8] Flavin adenine dinucleotide (FAD) and flavin adenine mononucleotide (FMN) are the most common cofactors in flavoenzymes and riboflavin (RF), also known as vitamin B2, is the most common natural precursor for both FAD and FMN. FAD, FMN, and RF share a common isoalloxazine ring and differ only in the identity of the side chain (see Figure 1-1).[9]

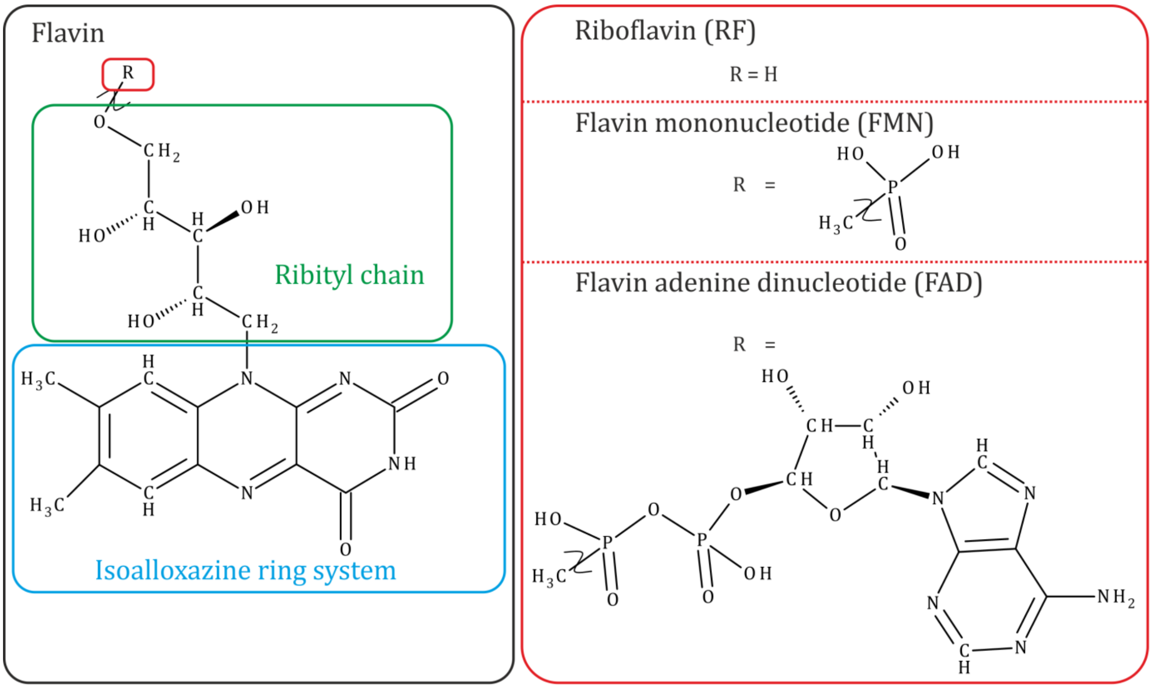

Figure 1-1: Chemical structures of riboflavin (RF), flavin mononucleotide (FMN), and flavin adenine dinucleotide (FAD) which all share a common isoalloxazine ring system (blue) and ribityl chain (green).

Cryptochromes share a high sequence homology with DNA photolyases (PL) but do not exhibit the same DNA repair functionality. They are instead often involved in regulatory mechanisms in organism, such as the light-dependent flowering response in plants and the setting of the circadian clock in animals depending on light conditions.[10-11] They are furthermore thought to facilitate the magnetic compass sense in some animals such as the

European robin (*Erithacus rubecula*, *Er*) and the fruit fly (*Drosophila melanogaster*, *Dm*) which will feature in this thesis.[5, 7, 12-13]

1.1.1 The role of cryptochromes in magnetoreception

The working hypothesis, the so called RP mechanism, is based on a photoinduced SC RP (see Section 1.2 for more detail). To date the most likely host of the RP mechanism *in vivo* are cryptochromes, which are currently the only vertebrate proteins known to form magnetically sensitive RPs via photoexcitation.[7, 12, 14-15]

Behavioural assays, in which cryptochrome deficient fruit flies did not respond to magnetic fields in contrast to wild-type fruit flies, provide strong evidence that cryptochrome plays a key role in magnetoreception.[5] Furthermore, cryptochromes have been found in the retina of migratory birds, and there is evidence that birds visualize magnetic cues for orientation using their eyes.[13, 16-17] The compass sense in migratory birds is light dependent, consistent with the proposed photochemical mechanism involving the light induced formation of a RP in cryptochromes.[2, 18-19]

Besides *Dm*Cry, which has been proven to be a key component for magnetoreception in fruit flies, *Er*Cry4 is of particular interest to elucidate the biochemical origin of the magnetic sense in the migratory European robin. While a ~24h periodic expression of *Er*Cry1 and *Er*Cry2 was observed, consistent with the usual role of cryptochromes in the night-day rhythm of the circadian clock, no ~24h periodicity of retinal *Er*Cry4 could be detected.[20] Instead *Er*Cry4 exhibits a seasonal expression pattern with increased expression during migratory seasons, which in turn *Er*Cry1 and *Er*Cry2 do not.[20] This suggests that *Er*Cry4 does not play an important role in the circadian rhythm, but instead might play a role in magnetoreception during migration.

However, none of the evidence presented above demonstrates unambiguously that cryptochrome is the immediate magnetoreceptor-molecule, and could be rationalized instead by considering that cryptochromes might play a role in the signal transduction pathway instead, either prior to or after the actual magnetic field sensitive step. To further the understanding of the sensitivity of photoinduced radical pairs in cryptochromes towards magnetic fields, the photochemistry of *Er*Cry4 and its sensitivity to magnetic fields is studied and contrasted to *Dm*Cry, the plant cryptochrome *Arabidopsis thaliana*

(*At*) *At*Cry1, and a series of non-natural flavoproteins known as flavomaquettes. In this work evidence for magnetic field effects (MFEs) on the photochemistry of a migratory bird cryptochrome is presented for the first time.

1.1.2 Photochemistry of Flavoproteins

Proteins belonging to the flavoprotein family non-covalently bind a flavin chromophore. In the dark state of the protein, the flavin is in its oxidized form (^{1}F).[21] A typical UV/VIS absorbance spectrum of a cryptochrome in its dark/ground state is shown for *Er*Cry4 representatively in Figure 1-2.

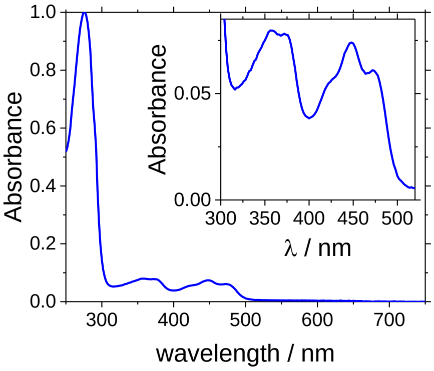

Figure 1-2: UV/VIS absorbance spectrum of *Er*Cry4 wild type.

The peak at 446 nm corresponds to an electronic $\pi \rightarrow \pi^*$ transitions between the highest occupied molecular orbital (HOMO) and the lowest unoccupied molecular orbital (LUMO) of the oxidized flavin ^{1}F. This band is attributed to the $S_0 \rightarrow S_1$ transition, where S_0 and S_1 refer to the singlet spin states of the ground state and the singlet spin state of the excited state, respectively.[8, 22] The peak at 375 nm is assigned to an electronic $n \rightarrow \pi^*$ transition and is referred to as $S_0 \rightarrow S_2$ transition.[8, 22] In flavins, the energy gaps between the S_0 and the S_1 and S_2 states, respectively, is largely defined by the isoalloxazine ring, and is therefore comparable in magnitude between different flavin homologues. The relatively strong absorbance peak in the UV (<300 nm) stems largely from the absorption of amino acids such as the aromatic amino acids Trp and tyrosine (Tyr).

From the singlet excited state, the flavin can undergo several processes commonly observed in free solution or bound inside a protein, such as fluorescence, intersystem crossing (ISC), energy transfer, photoreduction, and proton-coupled electron-transfer from the ribityl side chain attached to the N-10 of the isoalloxazine ring.[23-27] While ISC is commonly observed in flavins in aqueous solution, electron-transfer (ET) from nearby aromatic amino acids in functional cryptochromes and other flavoproteins takes place on a picosecond timescale and outcompetes ISC.[23-25, 28-29]

Proton-coupled ET from the ribityl side chain attached to the N-10 of the isoalloxazine ring leads to the loss of the ribityl chain and the formation of lumichrome (L), the smallest flavin homologue. This photodegradation process is commonly observed in flavins such as FAD, RF, and FMN in free solution.[26-27]

The capability of the flavin cofactor bound in flavoproteins to act as a redox centre is key to understanding the functionality of flavoproteins in general, and the potential role of cryptochromes in magnetoreception in particular. Although much progress has been made in predicting ET rates between cofactor and amino acid inside a protein, it continues to be a challenging task.[30] An empirical method to estimate the rate of electron tunnelling in proteins has been proposed by Moser and Dutton.[31] The so-called Moser-Dutton ruler is based on the Marcus electron transfer theory.[32] It expresses the ET rate constants for exergonic and endergonic ET processes (k_{ET}^{ex} and k_{ET}^{en}, respectively) as a function of the edge-to-edge distance between the donor and the acceptor (R), the driving force (ΔG), and the reorganization energy (λ):[31]

$$\log_{10} k_{ET}^{ex} = 13 - 0.6(R - 3.6) - 3.1(\Delta G + \lambda)^2 \frac{1}{\lambda} \tag{1.1}$$

$$\log_{10} k_{ET}^{en} = 13 - 0.6(R - 3.6) - 3.1(-\Delta G + \lambda)^2 \frac{1}{\lambda} - \frac{\Delta G}{0.06}. \tag{1.2}$$

To use Equation 1.1 and 1.2, k, R, and ΔG are given in units of 1/s, Å, and eV respectively. Note that the rate constant for electron tunnelling decreases exponentially with the distance R. From the term $0.6(R - 3.6)$, where 3.6 Å is the van der Waals distance, it follows, that the ET rate constant in-/decrease by an order of magnitude for changes in the edge-to-edge distance for each 1.7 Å. Good agreement between experimental results for the rate constants of ET in a wide range of natural and modified proteins has been found.[31]

1.2 Flavomaquettes: artificial model proteins for cryptochromes

“What I cannot create I do not understand”

Richard Feynman

Proteins are extraordinary molecular machines, usually comprised of thousands of atoms fulfilling a vast variety of complex functionalities. Reproducing or even surpassing nature’s ability in areas such as such as catalysis or immune defence, which are carried out by proteins *in vivo*, is obviously of great interest, but progress is this area has proven difficult due to the inherent complexity of proteins. Processes in proteins are subject to and governed by multiple interactions between amino acids, cofactors, and the surrounding matrix, which evolved through evolution in a complex fashion.[33-34] The complexity arises amongst others from the fact that a particular function of a protein may both be critically dependent on the role of a single amino acid, as well as the interplay of many amino acids or even assemblies of proteins at the same time.[34] To try and capture the capabilities of natural proteins in manmade molecular structures, a deeper understanding of the mechanisms behind the functionality of proteins is necessary; expressed in the words of the Noble laureate Richard Feynman, what I do not understand I cannot create. A promising approach to shed light on the principles that govern protein functionality and to harvest the potential of proteins is based on the *de novo* design and synthesis of artificial proteins.

Flavomaquettes are artificial proteins, *de novo* designed to fulfil specific functions often inspired by natural proteins.[35-36] Using a simplistic scaffold, deliberately not imitating the complex structure of the natural protein, and step wise development of the maquette, allows investigating the role of a protein’s individual components in a controlled environment. Since the pioneering work by DeGrado and Regan in 1988 to create maquettes based on a self-assembling four helical bundle, substantial progress has been made, accompanied by an ever increasing understanding of natural and non-natural proteins.[37]

The range of maquette functionalities is diverse, with light-havesting,[38] transmembrane ET,[39] and catalysis[40] as examples where recent noteworthy progress has been made. Proteins with redox functionalities are of particular interest and a series of redox active maquettes has been developed including maquettes that incorporate porphyrin-metal cluster, inorganic iron-sulfur cluster, and organic cofactors such as quinones as well as flavins which are further investigated in this thesis (see Chapter 4).[35, 41-42]

1.3 Spin Chemistry

In contrast to other intrinsic properties of the electron, such as its mass (9.1×10^{-31} kg) or charge (1.6×10^{-19} C), the spin angular momentum of the electron ($\vec{s}$) is a fundamentally quantum mechanical phenomenon and cannot be rationalized by classical physics. However, a hand-waving analogy to classical physics is that the rotation of the electron around its own axis is what creates this inherent spin angular momentum. This metaphor is helpful to visualize the spin angular momentum as a property of electrons and even allows one to understand, in a classic sense, the magnetic moment ($\vec{\mu}_e$) of the electron as a result of a rotating charged particle.

The magnitude of the spin angular momentum $\vec{s}$, *i.e.* the eigenvalue of the spin angular momentum operator ($\hat{s}$), is quantified by the spin angular momentum quantum number $s = ½$:

$$\|\vec{s}\| = \hbar\sqrt{s(s+1)}. \tag{1.3}$$

The orientation of $\vec{s}$ is defined by the magnetic quantum number, m_S, which can take on values of either $m_S = +½$ referred to as the “spin-up” or α state, or $m_S = -½$, referred to as the “spin down” or β state (see Table 1-1).

Table 1-1: Spin states of an electron as defined by the spin angular momentum quantum number *s* and the magnetic quantum number m_S.

Spin state	$\lvert s, m_s \rangle$
$\lvert \boldsymbol{\alpha} \rangle$	$\left\lvert \frac{1}{2}, +\frac{1}{2} \right\rangle$
$\lvert \boldsymbol{\beta} \rangle$	$\left\lvert \frac{1}{2}, -\frac{1}{2} \right\rangle$

The spin magnetic moment $\vec{\mu}_e$ is proportional to the spin angular momentum:

$$\vec{\mu}_e = \gamma_e \vec{s} \qquad 1.4$$

and

$$\vec{\mu}_e = \frac{g\ \mu_B}{\hbar} \vec{s}, \qquad 1.5$$

where γ_e is the gyromagnetic ratio, μ_B is the Bohr magneton, and g is the g-value of the electron ($g \approx 2.0023$ for an electron in vacuum). The g-value depends on the spin-orbit coupling and is approximately equal to 2.00 (±0.1%) for most organic radicals.[43]

1.3.1 Electrons in a magnetic field

Classically, the energy of the interaction between a magnetic moment $\vec{\mu}$ and a magnetic field $\vec{B}$ is given by:

$$E = -\vec{\mu} \cdot \vec{B} \qquad 1.6$$

and

$$E = -\mu\, B \cos \theta, \qquad 1.7$$

where μ, B, and θ are the magnitude of the magnetic moment, the magnetic field intensity, and the angle between $\vec{\mu}$ and $\vec{B}$, respectively. From Equation 1.6 follows that the orientation of the magnetic moment has a decisive effect on the interaction energy, with negative interaction energy E when $\vec{\mu}$ is parallel to $\vec{B}$ and positive E when $\vec{\mu}$ is antiparallel to $\vec{B}$.

The Hamiltonian describing the interaction of the magnetic moment of an electron with a magnetic field, *i.e.* the Zeeman interaction, is:

$$\hat{H}_{Zm} = -\hat{\vec{\mu}}_e \cdot \vec{B} = -\frac{g\,\mu_B}{\hbar}\,\hat{\vec{s}} \cdot \vec{B}, \qquad 1.8$$

where $\hat{\vec{\mu}}_e$ and $\hat{\vec{s}}$ are the magnetic moment operator and spin angular momentum operator. In sufficiently strong magnetic fields, the spin angular momentum is quantized along the direction of the magnetic field. Considering the interaction of the spin angular momentum with a magnetic field $\vec{B}_0$ parallel to the quantization axis, conventionally the z-axis, $\hat{H}_{Zm}$ can be expressed as:

$$\hat{H}_{Zm} = -\frac{g\,\mu_B}{\hbar}\,\hat{s}_{\mathrm{z}}\,B_0, \qquad 1.9$$

where $\hat{s}_{\mathrm{z}}$ is the operator for the projection of $\vec{s}$ onto the z-axis. $|\alpha\rangle$ and $|\beta\rangle$ are eigenstates of $\hat{s}_{\mathrm{z}}$ and the eigenvalues are

$$\hat{s}_{\mathrm{z}}\,|s, m_s\rangle = m_s\hbar|s, m_s\rangle. \qquad 1.10$$

Hence the Zeeman interaction energy is

$$E_{Zm} = -m_s g\,\mu_B B_0. \qquad 1.11$$

The difference in energy of the $|\alpha\rangle$ and $|\beta\rangle$ spin states in a magnetic field B_0 is therefore:

$$\Delta E = g\mu_B B_0. \qquad 1.12$$

The splitting of the energy levels of different spin states in a magnetic field is known as the Zeeman effect.

Note that so far we have only considered an isolated electron in an externally applied magnetic field. For this work, as is the case for most studied systems, the interactions of electrons with other electrons and nuclei have to be considered.

1.3.2 Spin correlated radical pairs in a magnetic field

In a radical only the unpaired electron contributes to the overall spin angular momentum, since the magnetic moments of paired electrons cancel each other out. Therefore, an isolated radical possesses an overall electron spin angular momentum quantum number of S = ½. In a radical pair (RP) comprised of two radicals, each of which has an unpaired electrons, the overall spin state has to be considered. The overall electron spin angular momentum S and the resulting overall magnetic quantum number M_S of a RP can be obtained using the Clebsch-Gordan series ($S = s_1 + s_2,\ s_1 + s_2 - 1, \ldots, |s_1 - s_2|$), where s_1 and s_2 are the spin angular momentum quantum numbers of the two unpaired electrons, respectively: S = 0, 1 and $M_S = S$, S−1, …, −S. The result is four spin states differing in S and/or M_S, listed in Table 1-2.

Table 1-2: Coupled representation of the four spin states of a radical pair based on their overall spin quantum number S and magnetic quantum number M_S.

Spin state	$\boldsymbol{|S; M_S\rangle}$
$|\mathbf{S}\rangle$	$|0{,}0\rangle$
$|\mathbf{T_0}\rangle$	$|1{,}0\rangle$
$|\mathbf{T_+}\rangle$	$|1{,}1\rangle$
$|\mathbf{T_-}\rangle$	$|1,-1\rangle$

The spin states of a RP are illustrated in Figure 1-3 using a vector model. Each of the arrows represents the spin angular momentum vector $\vec{s}_1$ and $\vec{s}_2$ of the two individual electrons of the RP. Note that both $\vec{s}_1$ and $\vec{s}_2$ are of length $\hbar\sqrt{3}/2$ (see Equation 1.3) and have a z-component of magnitude $m_s\hbar$. The vector model captures the overall spin multiplicity. In the three triplet spin states, T_+, T_- and T_0, the overall electron spin angular momentum quantum number is S = 1, and hence M_S = 1, −1, and 0, respectively. The length of the vector sum of $\vec{s}_1$ and $\vec{s}_2$ is $\hbar\sqrt{2}$ and the z-component ($\mathrm{S_z} = \mathrm{M_S}\hbar$) is $\hbar$, $-\hbar$, or 0 for T_+, T_- and T_0 respectively. In the state with S = 0 and M_S = 0, both the vector sum and the z-component are 0.

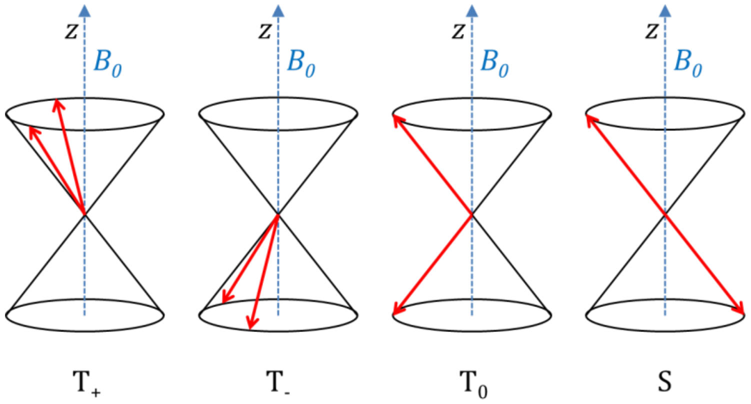

Figure 1-3: Vector model of the four coupled spin states in a RP quantized along a common axis of a magnetic field B_0.

RPs can either exist in a spin correlated (SC) or uncorrelated state, which means that the two electron spins of the individual radicals are either oriented with respect to each other (*e.g.* preferentially parallel, or antiparallel) or oriented randomly. Spin correlation of the RPs is a necessity for the manifestation of magnetic field effects in RPs observed in this thesis, as will become clearer in the following sections. RPs formed through photoinduced ET, such as the RPs investigated in this thesis, are produced as SC RPs in pure singlet (S) or pure triplet (T) states, conserving the initial spin state of their precursors. The pure S (or T) state of the SC RP is not generally a stationary state, and several coherent and non-coherent mechanisms outlined in the following subsections drive S-T interconversion.

1.3.2.1 *Hyperfine mechanism*

The spin angular momentum of an unpaired electron precesses around the direction of a magnetic field $\vec{B}$ at the Larmor frequency:

$$\omega_0 = g\mu_{\mathrm{B}}B/\hbar. \tag{1.13}$$

For example, the Larmor frequency of an electron (with $g = 2$) in a magnetic field of $B = 30$ mT is $\omega_0 \approx 5.3$ GHz, and is approximately 8.8 MHz at 50 µT, which is a typical value for the Earth's magnetic field. The magnetic moment of an electron can interact with the magnetic moments of atomic nuclei through dipole-dipole interactions. One distinguishes between direct dipolar interaction and Fermi-contact interaction. The direct dipole interaction is anisotropic while the Fermi-contact interaction is isotropic and only relevant for electrons with a finite probability to be found at the nucleus (*e.g.* in s-orbitals).

Nuclei with non-zero spin angular momentum relevant for this work and abundant in most biological systems, are hydrogen ^{1}H and nitrogen ^{14}N. Note that the carbon nucleus ^{12}C, with a natural abundance of 99%, has no spin angular momentum.

The magnetic field experienced by an electron can be approximated as the vector sum of *i* externally applied magnetic fields $\vec{B}_{0,\mathrm{i}}$ and the magnetic field induced by hyperfine coupling $\vec{B}_{\mathrm{hf},n}$ with *n* nuclei:[44-45]

$$\vec{B} = \vec{B}_0 + \vec{B}_{\mathrm{hf}} = \sum_i \vec{B}_{0,i} + \sum_n \vec{B}_{\mathrm{hf},n}. \qquad 1.14$$

The magnitude ($B_{\mathrm{hf},n}$) of $\vec{B}_{\mathrm{hf},n}$ is proportional to the nuclear magnetic quantum number $m_{I,n}$ and the isotropic hyperfine coupling constant a_n of the surrounding *n* nuclei:

$$B_{\mathrm{hf},n} = m_{I,n} a_n. \qquad 1.15$$

It becomes clear from Equation 1.13 that a difference (ΔB) in the magnitudes of $\vec{B}$ experienced by the individual unpaired electrons of a RP, causes a difference in their Larmor frequencies ω_1 and ω_2:

$$\Delta\omega_0 = \omega_1 - \omega_2 = \frac{g\mu_B}{\hbar}\Delta B. \qquad 1.16$$

This in turn leads to a change in the phase relation of the electron spins, and thus coherent interconversion between the S and T_0 states at a frequency dependent on the hyperfine interactions. The processes governing S-T interconversion and their dependence on external magnetic fields can be qualitatively understood by considering the vector model introduced above (see Figure 1-3), where the S and T_0 states differ only in the phase relation of the spin angular momenta of the individual electrons.[46]

The electron spin angular momenta, illustrated in Figure 1-3 by the red arrows, precess around a common axis defined by a sufficiently strong external magnetic field ($B_0 \gg B_{hf}$). However, in zero or weak external magnetic fields ($B_0 \lesssim B_{hf}$) the electron spins are likely to precess around different axes at different frequencies influenced by their respective local $\vec{B}_{\mathrm{hf}}$. This facilitates interconversion between all four states (S, T_+, T_-, and T_0). The interconversion of S and $T_{+/-}$ is different from the interconversion of S and T_0 as it involves a so-called spin-flip transition between T_0 and $T_{+/-}$.

Spin-flip transitions via the hyperfine mechanism can be restricted through application of external magnetic fields. Application of an external magnetic field B_0 much stronger than B_{hf} leads to the precession of the electron spin around a common axis defined by $\vec{B}_0$.

1.3.2.2 Δg mechanism

It is clear from Equation 1.13 that the Larmor frequency (ω_0) of an electron spin depends not only on the local magnetic field, but also on the g-values of the individual electrons. Consequently, the spins of electrons with different g-values precess at different Larmor frequencies. Analogous to the process of the hyperfine mechanism, a difference in ω_0 induces S-T_0 interconversion. Given the similarity of g-values (±0.1%) typically observed in organic radicals, S-T_0 interconversion via the Δg mechanism is negligible at the field strengths relevant to magnetoreception and the MFEs studied in this work ($B \leq 30$ mT). The Δg mechanism is dominant in organic SC RPs only at relatively high magnetic field strengths ($B > 1$ T).

1.3.2.3 Relaxation mechanism

The hyperfine mechanism and Δg mechanism both describe coherent spin evolution leading to S-T interconversion. In contrast, spin relaxation is an incoherent mechanism of S-T interconversion.

Spin relaxation is driven by random modulation of interactions of the electron spin with its environment. At high fields, spin-lattice relaxation, also known as T_1-relaxation, describes the relaxation between S/T_0 and T_+/T_- states and spin-spin relaxation (T_2-relaxation) drives the non-coherent interconversion of S and T_0. Common sources of random modulation of the anisotropic interactions of the electron spin with its environment are thermal motion and rotational tumbling.

Chemical or photoinduced SC RPs conserve the spin state of their precursors upon formation, and are prime examples of RPs formed with spin states far from thermal equilibrium. Modulation of anisotropic hyperfine interactions works towards restoring thermal equilibrium. Using the point dipole approximation, the spin-lattice relaxation time T_1 is proportional to the mean square value of the local fluctuating field ($\langle B_{loc}^2 \rangle$) acting on the electron spin of an isolated radical at high fields and the probability of finding a component of random fluctuation at the Larmor frequency ($J(\omega_0)$):[47]

$$\frac{1}{T_1} = \gamma_e^2 \, \langle B_{\mathrm{loc}}^2 \rangle \, J(\omega_0). \qquad 1.17$$

$J(\omega_0)$ is proportional to the probability of finding a component of random fluctuation at the Larmor frequency and can be expressed as:

$$J(\omega_0) = \frac{2\tau_c}{1 + \omega_0^2 \tau_c^2}, \qquad 1.18$$

where τ_c is the rotational correlation time and reflects the rotational frequency, *i.e.* the time it takes for a root-mean-square deflection of a molecule by 1 radian as a result of random molecular tumbling.

The Larmor frequency (ω_0) of the electron spin depends on the magnitude of the local magnetic field (see Equations 1.13 and 1.14). Modulation of the local magnetic field through random molecular motion works to destroy the phase coherence of the electron spins and leads to T_2-relaxation. The spin-spin relaxation time T_2 time is given by:[47]

$$\frac{1}{T_2} = \frac{1}{2}\frac{1}{T_1} + {\gamma_e}^2 \, \langle B_{\mathrm{loc}}^2 \rangle \, 2\tau_C. \qquad 1.19$$

Like T_1, the T_2-relaxation time depends on γ_e, $J(\omega_0)$, $\langle B_{\mathrm{loc}}^2 \rangle$, and τ_C and becomes similar in magnitude to T_1 for small τ_C, *i.e.* fast tumbling.

The magnitude of the fluctuation of the local magnetic field is strongly dependent on the distance between the electron and the nucleus ($B_{\mathrm{loc}} \sim r^{-3}$) and hence

$$\frac{1}{T_1} \sim r^{-6}. \qquad 1.20$$

It is clear from Equation 1.17 and 1.18 that in order for T_1 to be at a minimum, the anisotropic interaction needs to be modulated at the Larmor frequency ω_0:

$$\omega_0 = \gamma_e B = \omega_0(B = 30mT) = 5.30 \times 10^9 \mathrm{s}^{-1}. \qquad 1.21$$

As molecular vibrations are usually much faster than ω_0, molecular tumbling is often the source of the modulation of anisotropic hyperfine interactions and thus spin-lattice relaxation.

Considering Equation1.18, the spin-lattice relaxation rate induced by molecular tumbling is maximum for

$$\omega_0 = \frac{1}{\tau_C}. \qquad 1.22$$

To get an idea of the T_1 spin-relaxation rates relevant to the radicals investigated in this thesis, a rough estimate of τ_C for proteins can be obtained by assuming[47]

$$\tau_C \approx M \times \frac{\mathrm{ps}}{\mathrm{Da}}, \qquad 1.23$$

where M is the molecular mass. For cryptochromes with a molecular mass of 63 kDa the rotational correlation time is estimated to be $\tau_C \approx 63 \times 10^{-9}$ s. Since $1/\tau_C \approx 1.6 \times 10^7$ s^{-1} is much smaller than ω_0 (see Equation 1.21) the T_1-relaxation induced by molecular rotation is expected to be slow in aqueous solution. The T_1-relaxation in the artificial flavomaquettes used in this work (M = 15 kDa, $\tau_C \approx 15 \times 10^{-9}$ s and $1/\tau_C = 6.7 \times 10^7$ s^{-1}) is expected to be slow for the same reason. An interesting implication of this result is that for both the cryptochromes and flavomaquettes used in this work the, T_1-relaxation time is expected to increase with increasing rotational correlation time. In other words, slower tumbling is expected to lead to slower spin-lattice relaxation. Experimentally, slower tumbling of the proteins can easily be achieved by increasing the viscosity of the solution. Note however, that T_1-relaxation in Cry can also be induced by internal motions, which can be much faster than the molecular tumbling.

1.3.3 Electron-electron interactions in radical pairs

Besides the interactions of the electron spin with external magnetic fields and the magnetic moments of atomic nuclei, the electron spins of a RP interact with each other through exchange and dipolar interactions. Although the dipolar and exchange interactions are not measured directly in this thesis, they can have an effect on the manifestation of MFEs and will be discussed briefly in this section. For example, at short distances, for which the magnetic interaction energy between the electrons is much larger than the hyperfine interactions, spin mixing through the hyperfine mechanism may be suppressed. Furthermore, modulation of the exchange and dipolar interactions may contribute to spin-relaxation analogous to the spin-relaxation induced by random modulation of the anisotropic hyperfine interaction described in Section 1.3.2.

1.3.3.1 Exchange interaction

Electrons are fermions with s = ½ and are described by antisymmetric wavefunctions with regard to the interchange of a pair of electrons. Therefore, according to the Pauli exclusion principle, two electrons cannot be described by the same set of quantum numbers. Hence, if two electrons occupy the same orbital, *e.g*. their principle and angular momentum quantum numbers are the same, than they must differ in their spin magnetic quantum number. This leads to a decrease in the overall repulsion between electrons with the same spin and an increase for electrons with antiparallel spin. The Hamiltonian for the exchange interaction $\widehat{H}_J$ can be written as[48]

$$\widehat{H}_J = -J\left(\hat{S}^2 - \hat{1}\right), \tag{1.24}$$

where $\hat{S}$ is the sum of the spin angular momentum operators of radicals A and B ($\hat{S} = \hat{S}_A + \hat{S}_B$) and J the magnitude of the exchange interaction. The singlet and triplet states are eigenstates of $\widehat{H}_J$ and the exchange interaction energy can be calculated as:

$$\langle S|\widehat{H}_J|S\rangle = J \tag{1.25}$$

and

$$\langle T_m|\widehat{H}_J|T_m\rangle = -J \tag{1.26}$$

for the S and T_m spin states (m = −1, 0, +1). The magnitude of the exchange interaction J depends approximately exponentially on the radical pair separation (r)

$$J(r) \approx J_0 e^{-\beta r}, \tag{1.27}$$

where J_0 can be positive or negative and $\beta > 0$.[48] The degeneracy of T and S spin states is therefore lifted even at zero external magnetic field. The difference in energy between S and T states due to the exchange interaction is referred to as the exchange energy (ΔE_{Ex}):

$$\Delta E_{Ex} = 2\,J. \tag{1.28}$$

1.3.3.2 Dipolar interaction

The dipolar interaction is akin to the anisotropic contribution of the hyperfine coupling and describes the through-space interaction between two electron spins. The dipolar Hamiltonian can be written as:

$$\hat{H}_{\mathrm{D}} = \hat{D}_x\hat{S}_x^2 + \hat{D}_y\hat{S}_y^2 + \hat{D}_z\hat{S}_z^2 \qquad 1.29$$

where $\hat{S}_i$ and $\hat{D}_i$ are the x, y, and z-components of $\hat{S}$; and the dipolar interaction tensor **D**, respectively.

Treating electrons as point magnetic dipoles, the dipolar interaction is:[48]

$$D(r) = -\frac{3}{2}\frac{\mu_0}{4\pi}\frac{\gamma_e^2\hbar^2}{r^3}, \qquad 1.30$$

where μ_0 is the magnetic constant, γ_e is the gyromagnetic ratio, and r the radical pair separation. As mentioned before, the dipolar interaction has the potential to significantly reduce the effects of weak magnetic fields (*i.e.* $B_0 < B_{\mathrm{Ex}}$, B_{D}), such as the earth magnetic field, on the S-T interconversion. Furthermore modulation of dipolar and exchange interaction can induce spin relaxation.

Although the magnitude of the dipolar interaction decreases with increasing RP separation ($\sim r^{-3}$) it is usually stronger than the exchange interaction at large RP separations ($r > 2$ nm) but weaker at small RP separations. Furthermore, molecular tumbling of RPs in free solution can cause the anisotropic dipolar interaction to average out.

1.4 Magnetic field effects via the radical pair mechanism

The radical pair mechanism describes a chemical reaction proceeding via a SC RP and its sensitivity to applied magnetic fields. An outline of the theoretical background of the relevant spin dynamic processes is given in the previous Section 1.3, and more extensive descriptions can be found in the literature.[7, 44, 49-51]

The magnetically sensitive SC RPs investigated in this thesis are created through photoinduced ET.[a] A schematic of the relevant processes is shown in Figure 1-4. After light excitation the primary photoexcited state ($^1A^*$) can either undergo direct ET or intersystem crossing (ISC), following either the pathway indicated in blue or orange in Figure 1-4, respectively.[b] Depending on the spin multiplicity of the radical precursor, the radical pair is either formed in a singlet state $^1[A^{\bullet -}\ B^{\bullet +}]$ (*i.e.* singlet-born) or in a triplet state $^3[A^{\bullet -}\ B^{\bullet +}]$ (*i.e.* triplet-born). The ratio of initial S to T population depends on the reaction rates of the two competing mechanisms for ISC and ET. Back electron-transfer (BET) is only allowed from the singlet state, but other processes such as for example (de-) protonation are not spin selective and can lead to the formation of a photoproduct C (green reaction pathway in Figure 1-4).

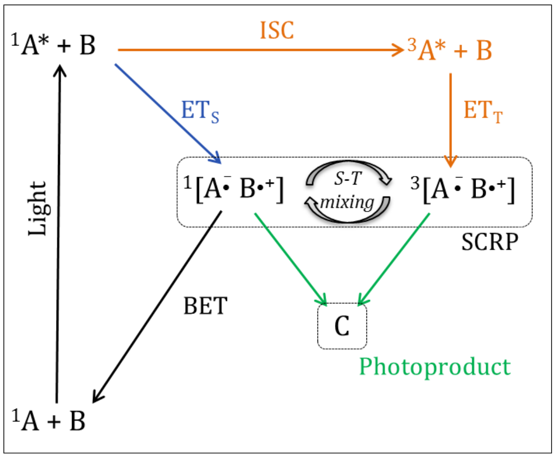

Figure 1-4: Schematic representation of the RP mechanism of a photo-induced SC RP. The SC RP is produced either directly from the singlet $^1A^*$ (blue pathway) or following ISC from the triplet (orange pathway) precursor. The photoproduct C can be formed from both S and T states (green pathway), while BET is spin selective, *i.e.* only allowed from the S state. See text for more details. Note that other processes, *e.g.* fluorescence, are common in such photoreactions, but not shown here, since they are not important for the understanding of the RP mechanism relevant for this thesis.

Let us for now imagine a case where the ET from the singlet state (ET_S) vastly outcompetes ISC, and the SC RP is therefore almost exclusively formed in the S-state, conserving the spin state of its molecular precursor. Note that the principles outlined

---

[a] Other processes such as homolytic bond cleavage, H-abstraction, or spin selective charge recombination are also known to produce SC RPs.

[b] Other processes such as fluorescence from the $^1A^*$ state are often observed in such photocycles, but since they are not of great relevance for this chapter they are not included here for clarity.

below apply equally to both singlet- and triplet-born RPs, and the implications for triplet-born RPs are outlined in subsection 1.4.1.2.

After formation, the singlet-born RP ($^1[A^{\bullet-}\ B^{\bullet+}]$) undergoes S-T interconversion driven by hyperfine interactions (see Section 1.3.2). Externally applied magnetic fields may affect the S-T interconversion and therefore the overall population difference of the S and T spin states (ΔP) and its temporal evolution. Since BET is only allowed from the S state and is spin forbidden from the T-state, a change in ΔP alters the fraction of the SC RPs to which the BET pathway is available. This directly affects the lifetime of the SC RP but also the relative yield of the product, C. Relevant processes that affect the S-T interconversion and thus the reaction yield via the RP mechanism are outlined in the following section, and the effects of magnetic fields on downstream products and methods for the detection of magnetically altered reaction yields are described in Sections 1.4.2 and 1.4.3.

1.4.1 Magnetic field effects on the S/T fraction via the hyperfine mechanism

The energy diagram shown in Figure 1-5 illustrates the energy levels of the S and T spin states of the SC RP in an external magnetic field B. In cases where the hyperfine coupling strength (E_{Hf}) exceeds the energy separation of the spin states, S and T-states can interconvert efficiently. The interaction of the magnetic moment of the unpaired electron with the magnetic field leads to an energetic separation of the T_+ and T_- states from the T_0-state by the Zeeman energy ΔE_{Zm} (see Figure 1-5) which reduces the interconversion efficiency between the S and T_0 states and the T_+ and T_- states.

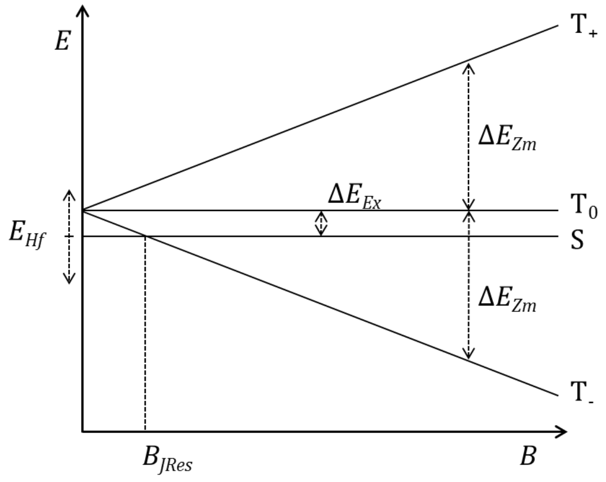

Figure 1-5: Energy diagram illustrating the effect of a magnetic field on the S and T spin states of a SC RP. The magnitudes of the hyperfine, Zeeman and exchange interactions are represented by dashed arrows labelled E_{Hf}, ΔE_{Zm} and ΔE_{Ex} respectively. B_{JRes} marks the intersection of the T₋ and the S-state.

The exchange interaction separates the S and the T-states energetically by ΔE_{Ex}. If the hyperfine coupling strength (E_{Hf}) driving S-T interconversion does not exceed ΔE_{Ex}, S-T interconversion is limited or inhibited even at zero external magnetic field (B = 0). In such cases an increase in S-T interconversion is expected, with a maximum for $B = B_{\mathrm{JRes}}$. B_{JRes} marks the magnetic field strength at which the S and T_- states are degenerate.

1.4.1.1 Saturation effect

As explained above, the S-T interconversion efficiency decreases with increasing energetic separation of the S and $T_{+/-}$ spin states through the Zeeman interaction of the electron spins. The decrease in mixing efficiency however saturates when ΔE_{Zm} becomes much larger than the hyperfine coupling that drives S-T interconversion. Consequently a change in B in a range where $\Delta E_{\mathrm{Zm}} \gg E_{\mathrm{Hf}}$ is not expected to have a tangible effect on the S/T fraction via the hyperfine mechanism and is therefore is not expected to lead to MFEs on the reaction yield. This saturation effect is commonly observed experimentally when the MFE is measured as a function of B, as a plateau for magnetic fields where $\Delta E_{\mathrm{Zm}} \gg E_{\mathrm{Hf}}$.

Note that MFEs induced by the Δg-mechanism (see section 1.3.2.2), which are of opposite sign to MFEs induced by the hyperfine mechanism, become relevant at very large B only, (*i.e.* >1 T) for the organic radicals investigated in this thesis. Hence in this work the plateauing of the MFE due to the saturation effect is observed without evidence for MFE induced by the Δg mechanism

1.4.1.2 Magnetic field effects on triplet-born SC RPs

The RP mechanism explaining the origin of the MFE on triplet-born SC RPs follows the same principles as the mechanism for singlet-born SC RPs described above.

In short, the application of a sufficiently strong external magnetic, field may “trap” the triplet-born SC RP in its triplet state by reducing the hyperfine driven S-T interconversion due to the increased energy gap between the T states induced by the Zeeman effect (see Figure 1-5). That way the fraction of SC RPs with S character, to which the BET pathway is available, is decreased. This leads to an increase in the overall observed lifetime of the SC RP as long as the relative fraction of the T-state population is increased.

Note that the MFE induced through the hyperfine mechanism is of opposite sign for singlet-born and triplet-born SC RP. This allows one to draw conclusions from the sign of the MFE regarding the spin state of the initially formed SC RP.

1.4.1.3 Relaxation effects

As described in Section 1.3.2.3, spin correlation is lost due to spin relaxation. Any change in the concentration of the SC RP induced by the hyperfine mechanism is only expected to be significant for cases, where spin selective BET of the SC RP is not much slower than the loss of spin correlation. Otherwise the vast majority of the RPs will undergo BET only after the spin correlation has been lost and equilibrium reached. Externally applied magnetic fields do not affect the S/T-fraction of RPs at equilibrium and therefore do not alter their reaction rates through the hyperfine mechanism once thermal equilibrium has been established.

Spin correlation of RPs in proteins is expected to be lost within ~1 μs.[7, 52] This effectively limits the lifetime of the magnetically sensitive species, *i.e.* sets a minimum for the rate constant describing the spin selective BET.

1.4.1.4 Low field effects

In weak magnetic fields, where the external magnetic field *B* is on the same order of magnitude as the average hyperfine interaction or smaller, an additional mechanism may lead to the manifestation of an MFE, the so called low field effect (LFE).

Upon application of even weak magnetic fields, the degeneracy of spin states, which have the same energy in zero external magnetic field, is lifted, causing additional S-T interconversions at frequencies corresponding to the difference in energy of the spin states. Note that in this way the application of a weak magnetic field can lead to an increase in S-T interconversion. Hence the LFE manifests itself as an MFE opposite in sign to the "normal" MFE discussed previously in this section.

Such LFEs were first predicted in 1976 by Brocklehurst[49] and have since been detected in Cry and non-biological model systems at magnetic fields of only B = 1 mT and 0.05 mT, respectively.[14-15] LFEs can in principle give rise to MFEs in Crys at magnetic fields as low as the Earth's magnetic field (0.05 mT) *in vivo* although there is so far no experimental evidence for MFEs in Crys at magnetic fields smaller than 1 mT.[7] LFEs were not observed in this work and in the remainder of this thesis "MFE" refers to the "normal MFE".

1.4.2 Magnetic field effects on downstream photoproducts

It has been shown in the previous subsection (Section 1.4.1) that magnetic fields can have an effect on S-T interconversion and hence the S/T-fraction in SC RPs. For singlet-born (triplet-born) SC RPs a decrease in S-T interconversion leads to a decrease (or increase) in the yield of the photoproduct C (see Figure 1-4). That way, the effects of magnetic fields, which evolve in the SC RP, can be passed on to the photoproduct C and a magnetically altered reaction yield (MARY) can be observed on downstream photoproducts as well as on the SC RP.

This has important implications, since a prerequisite for the manifestation of an appreciable MFE induced by the hyperfine mechanism is that the spin selective BET of the initially formed RP should not be much slower than the processes leading to the loss of its spin correlation (see Section 1.4.1.3 for more detail). This limits the lifetime of that RP to not be much larger than its correlation lifetime in order to observe MARYs.

In contrast to the lifetime of the initially formed RP, the lifetime of C can greatly exceed the spin correlation lifetime without diminishing the effect of magnetic fields on its concentration. That way the MFE can be effectively stored in C after manifestation in the SC RP. This storage mechanism for the MFE might play an important role in magnetoreception, since under continuous illumination longer lived species, whose concentrations are dependent on magnetic fields, are more likely to accumulate and reach concentration thresholds required for the signalling state or its precursors. This storage effect has been previously observed in cryptochromes *in vitro*.[15]

1.4.3 Methods for the detection of MFEs in flavoproteins

Transient absorption spectroscopy (TA) and fluorescence spectroscopy are frequently employed to characterise MFEs in flavoproteins.[15, 29, 42, 53-55] While fluorescence spectroscopy exhibits remarkably high sensitivity, it is limited to the detection of only a selection of species with sufficiently high fluorescence quantum yield. This includes the excited flavin singlet state ($^1F^*$), which facilitates the detection of MFE in flavin-based RPs with high sensitivity. But information on the concentration of the downstream photoproducts, including the SC RP, and their temporal evolution remains elusive.[29, 55-56]

In contrast, TA experiments can be used efficiently to track the concentration changes of individual species thanks to their time resolution and the distinct absorption properties of transient species, but conventional single pass TA often lacks the necessary sensitivity to characterize small MFEs in proteins.[15, 53, 57-60]

A series of condensed phase cavity enhanced transient absorption techniques are being developed in our group to detect small changes in differential absorbance upon application of magnetic fields. They include TA techniques without time resolution, such as broadband cavity enhanced absorption spectroscopy (BBCEAS), and with time resolution, such as optical cavity enhanced transient absorption spectroscopy (OCTAS) and cavity ring-down spectroscopy (CRDS). The advantage of using cavity enhanced TA techniques is their high sensitivity (compared to conventional single pass TA techniques), while also being sensitive to a large number of relevant species, including the transient species predominantly involved in the photocycle of flavoproteins (*e.g.* $^3F^*$, $F^{\bullet-}$, $FH^{\bullet}$ and $WH^{\bullet+}$).[59-61] The remainder of this thesis focuses on the application of CRDS measurements to study MFEs on the concentration of transient species after photoexcitation of flavoproteins.

Chapter 2.

Experimental approach and data analysis

MFEs on plant and insect cryptochromes have been previously studied extensively using conventional single pass TA and fluorescence spectroscopy.[15, 29, 42, 53-55, 62] To overcome some of the limitations of fluorescence and conventional single pass TA, outlined in the previous section (Section 1.4.3), a cavity enhanced variety of TA spectroscopy, cavity ring-down spectroscopy (CRDS), which has been developed for the purpose of MFE measurements in our group, is used in this work.[60] An introduction to CRDS and details of the specific experimental methods and parameters used in this thesis is presented in Section 2.1. The global target analysis method used to extract detailed insight into the dynamic photochemical processes from the CRDS data is explained in Section 2.2 and methods for the quantification and characterization of MFEs are described in Section 2.3.

In Section 2.4 the approach to furthering the understanding of the complex photochemistry and MFEs in cryptochromes using both selectively mutated cryptochromes as well as *de novo* designed maquette proteins is explained. Section 2.5 describes the employed methods of sample preparation.

2.1 Detection of MFEs in flavoproteins using cavity ring-down spectroscopy

Magnetic fields can have a decisive effect on the lifetime of SC RPs and the yield of downstream products by affecting the difference in S and T spin state population (ΔP) of the SC RP. This effect of magnetic fields can be quantified as a change in the lifetime of transient species and as magnetically altered reaction yield (MARY). The change in concentration associated with the effects of external magnetic fields (B) can be readily determined using sensitive spectroscopic techniques such as TA or fluorescence spectroscopy, which allow the concentrations of transient species to be directly observed as a function of B.

What makes the detection of a MFE of only a few percent or less in proteins a formidable challenge is, that: A) the costs and difficulties associated with flavoprotein production and their tendency to aggregate in aqueous solution restrict the sample concentration feasible for MFE measurements in aqueous solution to less than ~100 µM; and B) the light sensitivity of flavoproteins and their tendency to photodegrade limits the photoexcitation power.

In TA experiments on flavoproteins, both factors A and B lead to a differential absorbance of realistically $\lesssim 10^{-3}$ on which a small change (~1%) upon application of a magnetic field is required to be detectable. The recently developed condensed phase cavity ring-down TA technique combines the advantages of high sensitivity, species selectivity, and time resolution. That combination makes CRDS a very suitable technique to overcome the challenges associated with MFE measurements in proteins described above.

2.1.1 Principles of cavity ring-down spectroscopy

Cavity ring-down spectroscopy is a multi-pass TA technique, in which the sample is situated inside an optical cavity comprised of highly reflective mirrors, with enhanced sensitivity compared to conventional single pass TA experiments.[60, 63-64] In this section, the general principles of CRDS spectroscopy and the methods for data collection using CRDS spectroscopy are described in detail.

Simply put, the enhancement in sensitivity in CRDS measurements stems from the fact that the probe light, usually a laser light pulse, passes through the sample multiple times (~500) as the light gets reflected between the mirrors forming the optical cavity. Figure 2-1 shows a schematic of a CRDS measurement process.

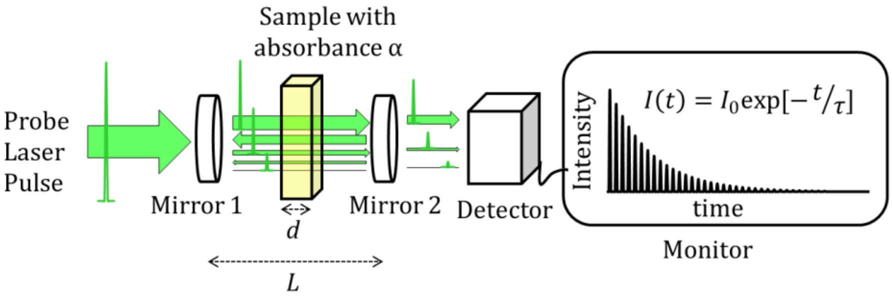

Figure 2-1: Schematic representation of a CRDS experiment, where a probe laser light pulse is injected into an optical cavity of length L comprised of Mirrors 1 and 2. The probe light pulse passes through a sample cell of length d and the fraction of the light (I) leaking through Mirror 2 onto the detector is recorded and analysed. The observable is the decay constant τ, *i.e.* the ring-down time, which describes the exponential decrease of the intensity of I.

The schematic illustrates a typical setup, in which a sample cell is situated in the centre of an optical cavity.[c] The probe light pulse is injected into the cavity through Mirror 1. Due to the high reflectivity the majority of the probe laser light is reflected from the back side of Mirror 1 and does not enter the optical cavity. Inside the cavity the light is reflected back and forth, passing through the sample multiple times. Each time the light is reflected by Mirror 2, a fraction of the light leaks out of the cavity onto a detector where the light intensity is recorded. With each round trip the probe light pulse is attenuated by a fraction and the light intensity (I) leaking out of Mirror 2 can be expressed as an exponential decay:

$$I(t) = I_0 e^{-{}^{t}/_{\tau}} \tag{2.1}$$

---

[c] In some applications the sample cell is omitted by “flooding” the optical cavity with the sample. This is common practice in gas phase measurements and also feasible in the condensed phase. It is, however, not a viable option for the measurements presented in this work, mainly due to the limited amount of sample available and the fact that the mirrors would become contaminated by proteins adsorbing to their surfaces with detrimental effects on their reflectivity.

where I_0 is the light intensity of the first light pulse exiting the cavity through Mirror 2 and τ is the time constant (*i.e.* the ring-down time) that describes the rate at which $I(t)$ decreases with time. The ring-down time τ is the observable in CRDS measurements and used to extract information about species and processes in the probed volume on the basis of the light attenuation caused by the species present in the probed volume. Other significant sources for the decrease in I are scattering and absorption taking place at Mirrors 1 and 2, the walls of the sample cell, and the solvent.

Let us for simplicity first imagine an "empty" cavity – that is a hypothetical cavity without any absorbing species inside and equal effective reflectivity of Mirrors 1 and 2. The rate at which I decreases depends primarily on the effective reflectivity (R) of Mirrors 1 and 2, the length of the cavity (L) and the speed of light (c):

$$\frac{dI}{dt} = -\frac{(1-R)c}{L}I. \tag{2.2}$$

In such a case, the light intensity detected leaking out of Mirror 2 is described by

$$I(t) = I_0 \exp\left[-\frac{(1-R)c}{L}t\right] = I_0 e^{-t/\tau_0}, \tag{2.3}$$

with

$$\frac{1}{\tau_0} = \frac{(1-R)c}{L}. \tag{2.4}$$

For example, the ring-down time achieved with the experimental setup described in this thesis is approximately 4 μs (measured at 530 nm of the cavity without sample cell inside the cavity). Using Equation 2.4 the effective reflectivity is than calculated to be ~0.9995. However, in order to estimate the τ_0 relevant for the experiments described in this thesis, the sample cell has to be considered as part of the optical cavity, and the additional light loss has to be considered in the calculation in the effective reflectivity as well. The ring-down time of the optical cavity including the (empty) sample cell is 1.5 μs, which equates to an effective reflectivity of 0.9987.

In the presence of absorber inside the sample cell, the absorbance (α) has to be considered as an additional source of light loss and the temporal evolution of I is then described by:[65,d]

$$\frac{dI}{dt} = -\left[\ln(10)\,\alpha\frac{c}{L} + \frac{1}{\tau_0}\right] I. \tag{2.5}$$

For constant absorbance (α =constant), integration of Equation 2.5 gives:

$$I(t) = I_0 \exp\left[-\left(\ln(10)\,\alpha\frac{c}{L} + \frac{1}{\tau_0}\right) t\right]. \tag{2.6}$$

Thus, for α =constant, $1/\tau$ takes the form:

$$\frac{1}{\tau} = \left(\ln(10)\,\alpha\frac{c}{L} + \frac{1}{\tau_0}\right), \tag{2.7}$$

where α can be expressed as a function of the path length of the light through the sample (d), the concentration (c_i) and the extinction coefficient (ε_i) of species i in the probed sample volume:

$$\alpha = \sum_i \varepsilon_i c_i d. \tag{2.8}$$

That way the observable in CRDS, τ, is linked to the concentration of the transient species.

In pump-probe transient absorbance measurements τ_0 can be readily determined experimentally by recording the ring-down time without prior excitation and the differential absorbance (ΔA) can be calculated using Equation 2.7 based on τ and τ_0:

$$\Delta A = \frac{\tau_0 - \tau}{\tau_0 \tau}\frac{L}{c}\frac{1}{\ln 10}. \tag{2.9}$$

The ΔA data presented in Chapter 3 is calculated using Equation 2.9, and the CRDS observables τ and τ_0 are calculated by fitting the light intensity $I(t)$ using Equation 2.1.

The approach based on calculating τ using Equation 2.9 has a time resolution inherently limited by the ring-down time, as changes in the differential absorbance during the ring-down time are not captured appropriately. Both τ and α are assumed to be constant in this approach. In order to quantify absorbance changes with a lifetime smaller or similar to the ring-down time, the time dependence of $\alpha(t)$ and hence $\tau(t)$ have to be considered. In

---

[d] The factor ln(10) expresses the absorbance α on the conventional $\log_{10}$ scale as the optical density $O = \ln(10)\alpha$.

Chapter 4, the comparatively long ring-down times (~0.5 µs) achieved with the flavomaquette samples and fast reaction kinetics observed in some of the flavomaquettes requires temporal deconvolution of the ring-down traces ($I(t)$) in order to analyse the reaction kinetics appropriately.

The decrease of the absorbance on the timescale of the ring-down time was approximated by:

$$\varDelta A = \beta e^{-kt} + \gamma \tag{2.10}$$

This leads to the following description of $I(t)$ based on Equation 2.5:

$$I(t) = I_0 \exp\left[-\frac{c}{L}\frac{\ln 10\, \beta}{k}\left(1 - e^{-kt}\right) - \frac{\ln 10\, c}{L}\gamma t - \frac{t}{\tau_0}\right] \tag{2.11}$$

To calculate β and γ, the ratio of $I(t)$ and $I'(t)$ was fit by the following function:

$$F = \frac{I(t)}{I'(t)} = \exp\left[-\frac{c}{L}\frac{\ln 10\, \beta}{k}\left(1 - e^{-kt}\right) - \frac{\ln 10\, c}{L}\gamma t\right]. \tag{2.12}$$

The differential absorbance observed in the flavomaquettes presented in Chapter 4 is calculated as (*c.f.* Equation 2.10 for $t = 0$):

$$\varDelta A = \beta + \gamma. \tag{2.13}$$

Note that ring-down times achieved with natural cryptochrome samples are significantly smaller (~0.2 µs) due to less favourable optical properties of the natural protein solutions which are attributed largely to scattering as a result of partial aggregation of the protein. The resulting sub-microsecond time resolution of the previously described approach based on Equation 2.9, is sufficient for the purpose of the investigation of the photochemistry described in Chapter 3. The $\varDelta A$ in Chapter 3 was calculated based on Equation 2.9 in order to avoid over-parameterisation which would lead to a significant decrease in the precision of the $\varDelta A$ measurements.

2.1.2 Experimental setup and parameters

The CRDS setup used in this thesis is shown schematically in Figure 2-2. A quartz flow cell (Hellma, 165-QS, 0.2 mL sample volume, d = 1 mm path length) is situated in the centre of an optical cavity comprised of two highly reflective mirrors M1 and M2 (Layertec, broadband coated, radius of mirror curvature 0.5 m, reflectivity > 99.7% in the wavelength range 450–690 nm). The length of the cavity is L = 0.6 m. For the photoexcitation at 450 nm a Nd:YAG (Continuum, Surelite I) pumped dye laser (Sirah, Cobra) was used. The measurements on the natural proteins and artificial proteins were performed with 1 mJ at 10/3 Hz and 0.3 mJ at 1 Hz respectively.[e] The probe light is generated by a tuneable optical parametric oscillator (Opotek, Opolette) and introduced into the cavity via the front mirror M1. Light leaving the rear mirror M2 is detected by a photomultiplier tube (Hamamatsu, H6780) and recorded on a digital oscilloscope (LeCroy, WaveSurfer 64MXs-A).

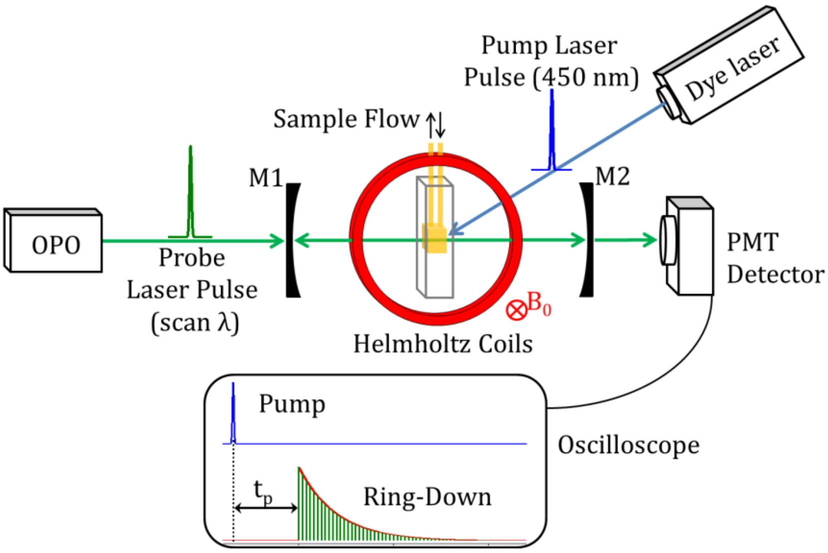

Figure 2-2: Schematic representation of the CRDS setup used in this thesis.

An external magnetic field B = 0–30 mT is applied using a set of custom built Helmholtz coils. The effect of a magnetic field B on the observed ΔA is quantified by subsequent measurements of ΔA at different magnetic field intensities. See Section 2.3 for more details on the quantification of magnetic field effects.

---

[e] In the measurements of natural proteins an additional dark time of 20 s between the variable scans (PPD time, or B) was introduce to allow the sample to recover between scans.

In cryptochrome measurements (Chapter 3), protein samples are kept at 278 K during measurements using a temperature controlled circulating bath (Grant, Optima T100). Flavomaquette measurements (Chapter 4) were performed without external cooling.

Cryptochrome samples (total sample volume ~200 μL) were measured under static conditions while flavomaquette samples (total sample volume ~1 mL) are recirculated at 2.5 mL min^{-1} (Bartels Mikrotechnik, mp6).

The light intensity leaking out of M2 is measured alternatingly with ($I(t)$) and without photoexcitation ($I'(t)$). The ΔA is recorded at specific time intervals after the photoexcitation by varying the pump-probe delay (PPD) time. The PPD time is controlled by digital delay generators (Quantum Composer, 9520; Stanford Research Systems, DG645). The ΔA is calculated based on $I(t)$ and $I'(t)$ using a least-squares curve-fitting routine (*fmincon*, The MathWorks, MATLAB R2014b) and Equations 2.9 and 2.12 for results on cryptochromes (Chapter 3) and flavomaquettes (Chapter 4) respectively.[f] Differential absorbance spectra are recorded by scanning the probe wavelength (λ) in steps of 10 nm from smaller to larger wavelengths.

The cryptochrome measurements presented in Chapter 3 and maquette measurements presented in Chapter 4 were performed under the conditions summarized in Table 2-1. For more information of the sample conditions see Section 2.4.

---

[f] Different fitting routines are used due to differences in the ring-down times and decay rates of the ΔA observed in cryptochrome and flavomaquette samples respectively. For more details see Section 2.1.1.

Table 2-1: Summary of the experimental conditions for both the cryptochrome and maquette measurements presented in Chapter 3 and 4.

	Cryptochromes	**Maquettes**
protein conc.	60-70 µM	20-25 µM
solvent composition (*aq.*)	10 mM TRIS pH7 (adjusted using HCl) 150 mM NaCl 20% (v/v) glycerol	20 mM phosphate buffer pH6.5 (adjusted using HCl) 100 mM KCl --
re-oxidising agent	5 mM ferricyanide	--
sample volume	200 µL	1 mL*
flow conditions	static	2.5 mL min^{-1}
temperature	278 K	291 K
excitation energy	0.3 mJ	1 mJ
frequency	1 Hz[†]	10/3 Hz

* The volume of the sample cell in all measurements is identical (200 µL). In maquette measurements the sample was circulated through a reservoir of 800 µL volume.
[†] The sample was allowed to recover in the dark for 20 s between variable scans of approximately 10 s.

2.2 Global target analysis of differential absorbance data

Analysing multidimensional data with respect to multiple parameters simultaneously, *i.e.* globally, is a common challenge in TA spectroscopy. This section focuses on the analysis of time (t) and wavelength (λ) resolved ΔA data (S_{data}), arguably the most common variant.

The contribution of each species (i) to a ΔA spectrum (S) is proportional to the concentration (c_i) and the extinction coefficient (ε_i) according to the Beer-Lambert Law

$$S(t,\lambda) = \sum_i c_i(t)\varepsilon_i(\lambda). \tag{2.14}$$

This is illustrated in Figure 2-3, where $S(t,\lambda)$ is expressed as the sum of the ΔA_i associated with individual species i. The ΔA of the individual species is calculated as the matrix product of a column vector representing the evolution of their concentrations in time, $c_i(t)$, and a row vector representing the extinction coefficient spectra $\varepsilon_i(\lambda)$. The overall $S(t,\lambda)$ can also be conveniently expressed in matrix form:

$$S(t,\lambda) = C(t)E(\lambda), \tag{2.15}$$

where C represents a matrix with i columns representing the evolution of the concentration of each species in time and E represents a matrix with i rows containing the wavelength spectra of each species. $S_{\text{data}}(t,\lambda)$ can be analysed efficiently by parameterizing c_i and/or ε_i using kinetic and spectral models as described in the following subsections.[66-67]

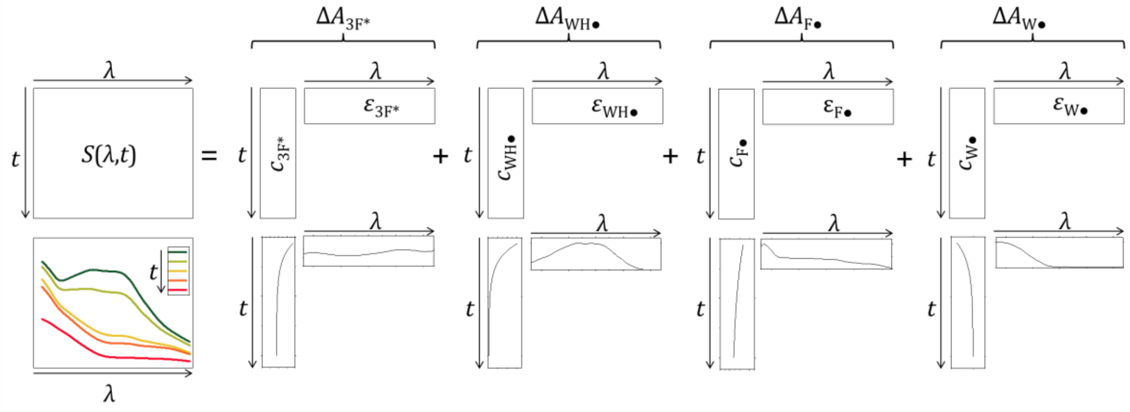

Figure 2-3: Schematic of the calculation of the temporal evolution of the overall ΔA, $S(t,\lambda)$, as the sum of the ΔA_i contributed by the individual transient species (i) according to Equations 2.14 and 2.15. In this example i = $^3F^*$, $WH^{\bullet +}$, $F^{\bullet -}$, and $W^{\bullet}$. The contribution of each species to $S(t,\lambda)$ is the matrix product of a column and a row vector representing the evolution of their concentration in time $c_i(t)$ and extinction coefficient spectra $\varepsilon_i(\lambda)$ respectively. Global target analysis based on a spectral model has been used to analyse ΔA of *Er*Cry4 wild type as an example here (*c.f.* Section 3.1.3.)

2.2.1 Kinetic model

Kinetic models are in general based on parameterizing $c_i(t)$ using reaction rate laws, where the reaction rate is proportional to the concentration c_i and rate constants k_i of the reactants i. Figure 2-4 illustrates the kinetic model used to analyse the data of a flavoprotein described in more detail in Section 4.1. The reaction rate laws (Figure 2-4 right) are based on the assumption of irreversible first-order reactions. The reaction scheme includes two excited species (A and B), and the ground state (C). At $t = 0$ the concentrations of B and C are assumed to be zero.

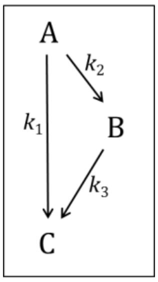

$$\text{I)}\quad \frac{dc_\mathrm{A}}{dt} = -k_1 c_\mathrm{A} - k_2 c_\mathrm{A}$$

$$\text{II)}\quad \frac{dc_\mathrm{B}}{dt} = k_2 c_\mathrm{A} - k_3 c_\mathrm{B}$$

$$\text{III)}\quad \frac{dc_\mathrm{C}}{dt} = k_1 c_\mathrm{A} + k_3 c_\mathrm{B}$$

Figure 2-4: Reaction scheme including two excited states (A and B), the ground state (C), and three rate constants k_1, k_2, and k_3. The rate equations I, II, and III are calculated based on the assumption of irreversible first-order reactions.

The time dependence of c_i was calculated using *SimBiology* (The MathWorks, MATLAB R2014b). A least-squares residuals fitting routine (*fmincon*, The MathWorks, MATLAB R2014b) was employed to optimize ε_i and $c_i(k)$ simultaneously:

$$\chi^2(k) = \sum_{\lambda,t} \big(S_\mathrm{data}(t,\lambda) - S_{\mathrm{fit}(k)}(t,\lambda,k)\big)^2, \tag{2.16}$$

where $S_{\mathrm{fit}(k)}$ is the parameterized fit function based on equation 2.14. That way rate constants k can be estimated directly. Furthermore species associated difference spectra (S_SADS) can be derived mathematically from Equation 2.15:[g]

$$S_{\mathrm{fit}(k)} = S_\mathrm{SADS}\, C(k) \tag{2.17}$$

$$S_{\mathrm{fit}(k)}/C(k) = S_\mathrm{SADS}. \tag{2.18}$$

2.2.2 Spectral model

Spectral models depend on knowledge about the shape and position of the absorption features of the relevant transient species. As a basis for the spectral model, known spectra of identical or comparable species (*e.g.* isoelectronic species) measured under identical or at least comparable conditions can be used. Assuming the ΔA spectra of all relevant

---

[g] The operator "/" in Equation 2.18 represents the operation for numerical matrix division *mrldivide* in MATLAB (The MathWorks, MATLAB R2014b)

individual species are known, the overall observed ΔA spectrum can be expressed as a linear combination of the ΔA of the individual species weighted by their respective concentrations (see Equation 2.14). Consequently, so called reference spectra ($\varepsilon_{R,i}$) can be used to reconstruct the observed ΔA in order to estimate the concentration of the species contributing to the overall ΔA.

In cases where the comparability under which the reference spectra were recorded is limited, physical perturbations of the chromophore through its environment and their effect on the ΔA spectra have to be considered. The interaction of the chromophore with its environment (*e.g.* through ion-dipole and dipole-dipole interactions, and hydrogen bonding), is known to alter the electronic structure and consequently the absorption properties of the chromophore. This effect is known as solvatochromism in the case of chromophore-solvent interactions and as enzymichromism in the case of perturbations induced by chromophore-protein interactions.[68] Trp radicals for example are known to exhibit solvatochromic and enzymichromic shifts of up to ±20 nm.[69-72] In this work a parameter θ is introduced to account for enzymichromic shifts of the observed absorption spectrum with regard to literature spectra ε_L:

$$\varepsilon_R(\lambda) = \varepsilon_L(\lambda + \theta). \qquad 2.19$$

If not stated otherwise, appropriate reference spectra are available and θ is fixed to zero to avoid over-parameterisation.

A least-squares residuals fitting routine (*fmincon*, The MathWorks, MATLAB R2014b) was used to optimise $c_i(t)$:

$$\chi^2(c_i) = \sum_{\lambda,t} \left(S_{data}(t,\lambda) - S_{fit(c)}(t,\lambda)\right)^2, \qquad 2.20$$

where $S_{\mathrm{fit}(c)}$ is the fit function based on equation 2.14 and 2.19:

$$S_{fit(c)}(t,\lambda) = \sum_i c_i(t)\varepsilon_{R,i}(\lambda + \theta_i). \qquad 2.21$$

Since the reference spectra $\varepsilon_{R,i}$ are normalized to give an integrated absorbance of 1, the resulting $c_i(t)$ represents the relative contribution of species i to the overall ΔA spectrum at time *t*, which is proportional to its relative concentration at that time. This makes it possible to estimate the time dependence of the concentration of transient species. The temporal evolution of $c_i(t)$ can in turn be analysed using kinetic models analogously to the method described above (see Figure 2-4) to deduce kinetic parameters and identify reaction pathways.

Note that in contrast to the use of a kinetic model, no assumptions regarding the reactivity of the species are made. Hence results acquired through global analysis based on a spectral model are not biased towards any particular reaction scheme. This is a noteworthy advantage over the use of a kinetic model which requires the assumption of a reaction scheme to start with. On the flip side, the spectral model suffers from relying on the accuracy of the reference spectra and the correct identification of all contributing species. For that reason, each results section that includes global analysis based on a spectral model is preceded by a section which focusses on the identification of the transient species and discusses the accuracy of the reference spectra.

2.3 Quantifying and characterizing magnetic field effects

In this work MFEs are measured as the change in ΔA with application of a magnetic field *B*. The difference in ΔA is measured by subsequent measurements of ΔA with (ΔA_B) and without ($\Delta A_{B=0}$) an external magnetic field applied as an absolute change ($\Delta\Delta A$) and a percentage change ($\%MFE$):

$$\Delta\Delta A(B) = \Delta A_B - \Delta A_{B=0} \qquad 2.22$$

$$\%MFE = \frac{\Delta\Delta A}{\Delta A_{B=0}} \qquad 2.23$$

An increase in ΔA with increasing *B* is interpreted as an increase in the concentration of absorbing species and *vice versa*.

The hyperfine interactions in a SC RP facilitate S-T interconversion, as long as the hyperfine interaction energy is larger than or comparable to the energetic separation between the spin states (see Figure 1-5). With increasing energetic separation of the spin states through the Zeeman interaction energy, S-$T_{+/-}$ interconversion efficiency is reduced.

For strong magnetic fields where the Zeeman interaction energy is much larger than the hyperfine interaction energy, S-T interconversion is restricted to mixing of S and T_0, and no further reduction of S-T interconversion efficiency with increasing magnetic fields through the Zeeman interaction is observed.

This saturation effect, described in more detail in Section 1.4.1.1, is reflected in the shape of MARY spectra. A schematic representation of a typical MARY spectrum is shown in Figure 2-5. It is characterized by the saturation value (MFE_{sat}) and the magnetic field ($B_{1/2}$) where half of the saturation value MFE_{sat} is reached. The MFE_{sat} and $B_{1/2}$ can be evaluated by measuring and analysing the $\Delta\Delta A$ (or $\%MFE$) as a function of B. In this thesis a Lorentzian fit function is used to determine MFE_{sat} and $B_{1/2}$ from MARY spectra using the built in fitting routine of *OriginPro 2017* (*OriginLab Corporation*).

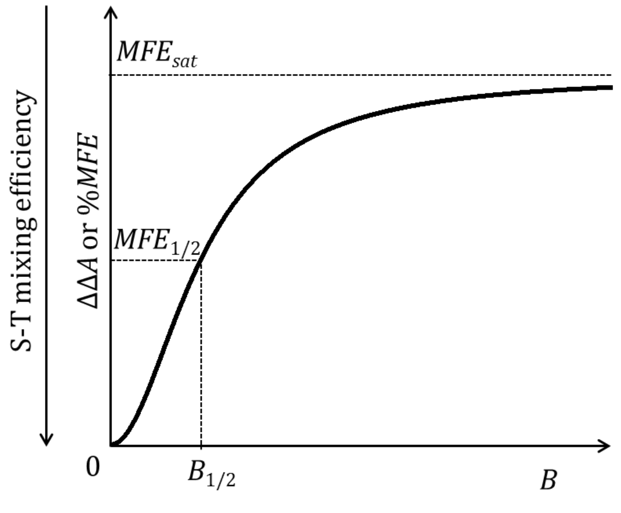

Figure 2-5: Schematic representation of the effect of a magnetic field on the S-T mixing efficiency and the resulting change in the observed $\Delta\Delta A$ or $\%MFE$ reflecting the change in concentration of transient species with B. The magnetic field where half of the saturation value (MFE_{sat}) is reached is marked $B_{1/2}$.

A theoretical value for $B_{1/2}$ can be estimated based on the Weller equation[15, 73-74]

$$B_{1/2} \approx \sqrt{3}\frac{B_1^2 + B_2^2}{B_1 + B_2}, \qquad 2.24$$

where B_1 and B_2 are the effective hyperfine coupling constants for radicals 1 and 2. The effective hyperfine coupling constants depend on the interaction between the nuclear spin with quantum number I_n of nucleus n and the anisotropic hyperfine coupling constants $a_{i,n}$:[73-74]

$$B_i = \left(\sum_n \frac{4}{3} a_{i,n}^2 I_n (I_n + 1)\right)^{1/2} . \qquad 2.25$$

Based on the Weller equation (Equation 2.24) and literature values for $a_{i,n}$, the $B_{1/2}$ for a flavin-Trp radical pair is estimated to be approximately 3 mT.[15, 74-75] However this approach of estimating $B_{1/2}$ is solely taking into account the hyperfine driven S-T interconversion, and neglects spin relaxation processes which are known lead to a broadening of the MARY spectra, *i.e.* an increase in $B_{1/2}$.[76]

In principle, a negative $\Delta\Delta A$ is expected for singlet-born RPs based on the hyperfine mechanism and positive MFEs for triplet-born RPs, as explained in more detail in Section 1.4.1. It is important to note however that LFEs (see Section 1.4.1.4) and MFEs induced by the Δg-mechanism (see Section 1.3.2.2) are opposite in sign to the "normal" MFE discussed in this thesis. The LFE can be the dominant MFE at magnetic fields on the same order of magnitude as the average hyperfine interaction (≈1−2 mT) or weaker, while the Δg-mechanism is only dominant at magnetic fields orders of magnitudes larger than both the average hyperfine interaction for the SC RP discussed and external magnetic fields used in this thesis.

2.4 Top-down and bottom-up approach: Natural, mutated, and artificial proteins

Besides the difficulty of detecting minute changes in the differential absorbance upon application of a magnetic field, another dimension of difficulty is added by the intrinsic chemical complexity of the approximately 63 kDa cryptochromes. Cryptochromes, like any other protein, have evolved to become highly complex molecular machines. For this thesis two promising and complementary approaches were used to cut through the natural complexity of cryptochromes and shed light on their rich photochemistry.

A) In a top-down approach, mutant Crys are used, where specific amino acids, which are anticipated to play a role in the photoinduced redox reaction, are replaced by redox inert phenylalanine. These selective modifications of the natural Crys allow us to investigate the role of individual amino acids and the effects of their absence.

B) In a bottom-up approach we use *de novo* and purposefully designed and "structurally simple" model systems, known as maquettes. That way we can circumvent the inherent complexity of natural Crys to study the interaction and photochemistry of selected amino acids and the flavin chromophore, independent of the obscuring complexity of their natural counterparts.

In the following two subsections the relevant properties of the Cry and maquette samples investigated in this thesis are described.

2.4.1 Cryptochromes

Cryptochrome samples have been recombinantly expressed in plant or bacteria cells as follows:

- *Er*Cry4 protein samples were expressed in *E. coli* bacteria using the full length complementary DNA of the *Er*Cry4-gene by Henrik Mouritsen *et al.* at the University of Oldenburg (Germany).[77]
- *Dm*Cry samples were expressed recombinantly by Stefan Weber and Erik Schleicher *et al.* at the University of Freiburg (Germany) using *E. coli*.[78]
- *At*Cry1 samples were provided by *Planet Biotechnology* after isolation and expression in *Nicotiana benthamiana* tobacco plants.[55]

In addition to the WT cryptochromes *Er*Cry4, *Dm*Cry, and *At*Cry1, mutated cryptochromes of *Er*Cry4 and *Dm*Cry were provided by the abovementioned sources. The WT samples exhibit an intact Trp ET chain as illustrated schematically in Figure 2-6, while in the mutant Crys specific Trps are replaced by redox inert phenylalanine.

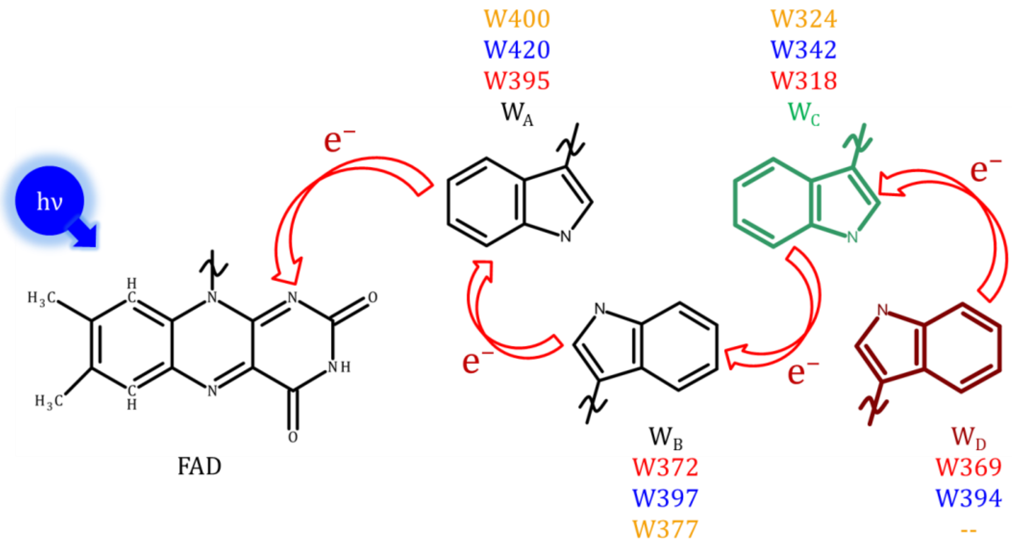

Figure 2-6: Schematic representation of the ET chain comprising W_A, W_B, W_C, and W_D in ***Er*****Cry4** and ***Dm*****Cry**. An ET chain of only 3 Trp has been identified in ***At*****Cry1**. Upon blue light excitation an electron is transferred along the 3 or 4 Trp as indicated by the red arrows. The Trp are labelled according to their position in the protein sequence in red for *Er*Cry4, blue for *Dm*Cry and yellow for *At*Cry1.[20] In the cryptochrome mutants *Er*Cry4 W324F and *Dm*Cry W318F investigated in this thesis, **W_C** (green) has been replaced by a phenylalanine and in *Er*Cry4 W369F and *Dm*Cry W394F **W_D** (brown) has been replaced by phenylalanine.

In the mutated cryptochromes investigated in Chapter 3 of this thesis, either W_C, the third Trp of the ET chain, or W_D, the fourth Trp of the ET chain was replaced by the aromatic but redox inactive amino acid phenylalanine (F).[h] These mutants are referred to as *Er*Cry4 W318F and *Dm*Cry W342F or *Er*Cry4 W369F and *Dm*Cry W394F reflecting the position of the replaced Trp in the amino acid sequence (see Figure 2-6). The aim of these mutations is to interrupt or shorten the Trp ET chain to gain insight into the role of the third and fourth Trp in the ET reaction.

The Cry proteins referred to as "wild type" (WT) in this thesis have been expressed *in vivo* as explained above and are largely identical to the natural Cry. A noteworthy difference is that all three (*Er*Cyr4, *Dm*Cry, and *At*Cry1) recombinantly expressed cryptochromes, WT and mutants, possess a so called histidine-tag fused to the N-terminal tail to facilitate

---

[h] The abbreviation for phenylalanine F is only used in the name of the mutant Cry *e.g.* *Er*Cry4 W318F to indicate that the W at position 318 was replaced by phenylalanine. In all other instances in this thesis F is used as abbreviation for flavin.

efficient purification of the protein sample after expression. Furthermore, the *Er*Cry4 amino acid sequence is different in two amino acids close to the N-terminal tail as compared to the natural *Er*Cry4. These differences are pointed out for completeness but are unlikely to have a tangible effect on the photochemistry investigated due to their position close to the N-terminal tail. For the remainder of the thesis the WT cryptochromes are referred to as the natural cryptochromes to highlight their natural composition of the Trp ET chain in contrast to the mutated cryptochromes.

2.4.2 Maquettes

Maquette samples investigated in this thesis were expressed in *E. coli* and provided to us by Dutton *et al.* (University of Pennsylvania, USA).[42] This chapter outlines the relevant synthesis and design principles, while all credit for the synthesis of the flavomaquettes goes to Dutton *et al.*

The maquettes are based on a monomeric α-helical design first published by Farid *et al.*[41] They are comprised of four α-helices which self-assemble in aqueous solution driven by hydrophobic-hydrophilic interactions. The general structure of the maquettes is represented as a "snake diagram" in Figure 2-7 (left). The α-helices (H1-4) are represented as arrows pointing from the N-terminal tail (N-TT) to the C-terminal tail (C-TT) and are connected by flexible amino acid loops. The amino acid sequence for the control and the Trp containing maquettes is shown in the appendix A1 and A2 respectively.

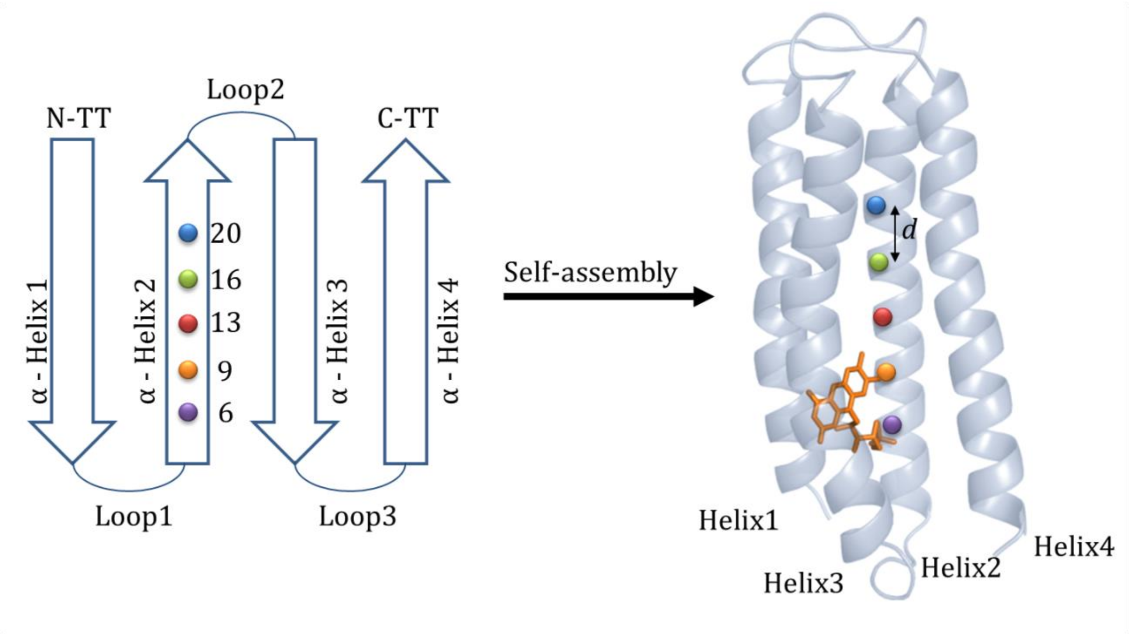

Figure 2-7: Snake diagram of the maquette design (left) and schematic representation of the folded maquette (right). The orange dot marks amino acid 9 (cysteine) on α-helix 2 which is the attachment site of the riboflavin chromophore. The amino acid positions 6 (violet), 13 (red), 16 (green), and 20 (blue) mark the positions of the amino acids which have been replaced with histidine (His, H) or Trp in the maquettes H6, W13, W16, and W20 respectively.

The amino acid at position 9 on helix 2 is highlighted by an orange dot and marks the position of the cysteine to which the RF (riboflavin) chromophore is covalently attached. Covalent attachment of the RF to cysteine was achieved by nucleophilic substitution of the bromine of 8-Br-RF as illustrated in Figure 2-8. The synthesis was performed by Bialas *et al.* and is described elsewhere in more detail.[42]

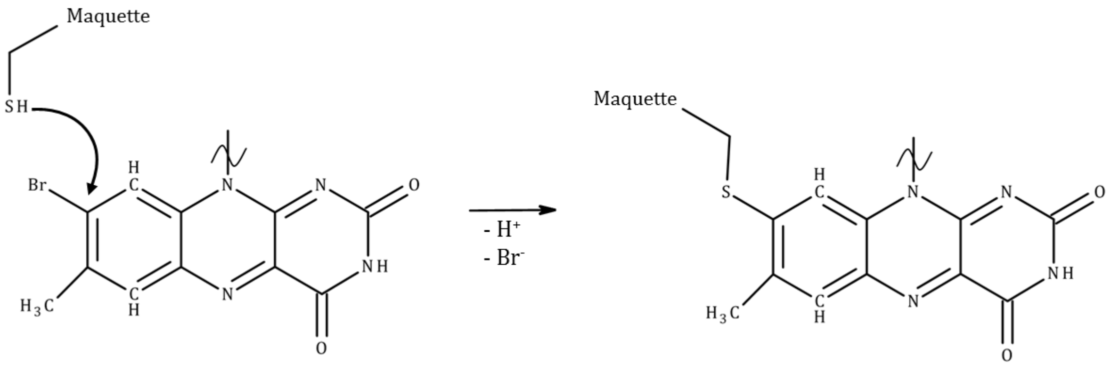

Figure 2-8: Nucleophilic aromatic substitution of Br with cysteine to achieve a covalent link between the RF chromophore and the maquette.

Amino acid position 6, 9, 13, 16, and 20 are marked by coloured dots and represent the positions in the amino acid sequence of Helix 2 which are one helical turn apart from the neighbouring marked position and pointing towards the hydrophobic centre in the folded maquette. A schematic of the folded maquette is shown on the right hand side in Figure 2-7. The distance (*d*) between the β-carbon atoms of the amino acids at position 6, 9, 13, 16, and 20 are one helical turn (~5.6 Å) apart, respectively. To study the light induced redox activity of the maquettes, Trp and histidine (His), which are known to reduce excited flavins, are introduced into the maquette structure by replacing the respective amino acid at the marked positions 6, 13, 16, and 20.

A set of 5 different flavomaquettes are investigated in this thesis, where either no or a single Trp/His is introduced into the maquette structure:

- A **control** with no amino acid capable of reducing the excited flavin
- One maquette, **H6**, with the amino acid of Helix 2 at position 6 replaced by His
- A series of three maquettes, where one amino acid of Helix 2 at increasing distances from the flavin, at position 13, 16, or 20 is replaced by Trp. These maquettes are referred to in the following as **W13**, **W16**, and **W20** respectively.

2.5 Sample preparation

Prior to the experiments, cryptochrome samples were filtered using micro pore centrifuge filters (Merck Millipore Ltd, Ultracel 30K). This is to remove unwanted small molecules, in particular unbound FAD. All samples (Cry and maquettes) were centrifuged for 90 min at 10,000 rpm to remove aggregated proteins. Aggregated proteins have the potential to interfere heavily with CRDS measurements as they scatter light in the observed wavelength region, which decreases the ring-down time and therefore the sensitivity of the experiment significantly.

The purity of the samples was then checked using UV/VIS spectroscopy (Agilent Technologies, Cary 60). Figure 2-9 shows exemplary UV/VIS spectra of A) *Er*Cry4 WT, *Dm*Cry WT, *At*Cry1 WT and B) the flavomaquette W13, and a (RF (20 µM), Trp (1 mM)) *aq.* solution. All flavoprotein samples exhibit the typical ground state absorbance of the oxidised flavin (^{1}F) at 450 nm. The cryptochrome spectra and the RF (*aq.*) spectra show the expected two peaks at 375 nm and 450 nm (see Section 1.1.2). The structure of the peak at 450 nm in the cryptochrome spectrum is attributed to enzymichromic effect of the protein environment on the FAD. The significant difference in the structure of the flavomaquette spectrum reflects the different electronic structure due to the sulphur-bond at the 8-position of the isoalloxazine ring.

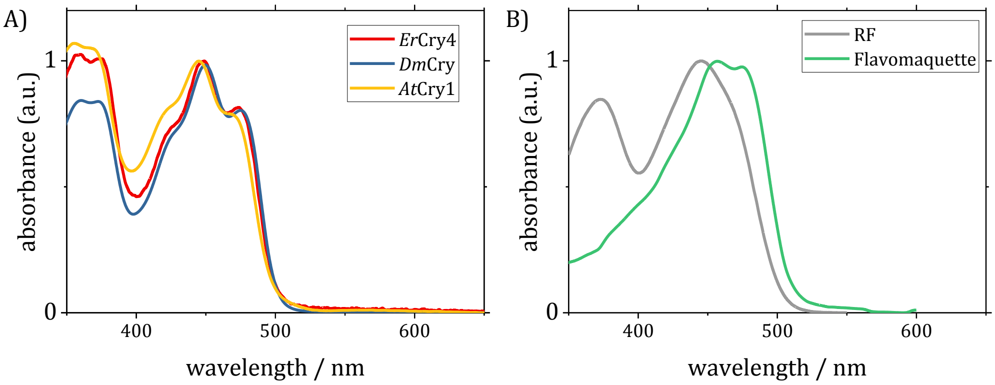

Figure 2-9: Normalized UV/VIS spectra of A) *Er*Cry4 WT (red), *Dm*Cry WT (blue), and *At*Cry1 WT (yellow) and B) RF (grey) and flavomaquette W13 (green). The spectra are normalized to their maximum around 450 nm for comparability.

Note that in none of the samples a significant absorbance at wavelengths larger than 520 nm is observed. This is an important precondition for the CRDS experiments performed in this work, where the wavelength region 520 nm to 690 nm is probed predominantly. Any light loss associated with the dark state of the sample (*i.e.* the sample without prior photoexcitation), shows up in the UV/VIS as a positive absorbance signal and would manifest itself as a reduced reference ring-down time τ_0 (see Section 2.1.1). This in turn would have a detrimental effect on the sensitivity of the CRDS measurements. Common sources for such unwanted light loss are aggregated proteins which cause light scattering, and the presence of the semi-reduced neutral FAD which absorbs light in the probed wavelength region. Protein aggregates are efficiently removed by centrifuging the sample prior to measurements. Stable semi-reduced neutral FAD is only observed in Cry samples, and 5 mM potassium ferricyanide ($K_3[Fe(CN)_6]$) is added to those in order to oxidize $FADH^{\bullet}$.

Chapter 3.

Effects of magnetic fields on the photochemistry of cryptochromes

Cryptochromes (Cry) are photoreceptor proteins found in a wide range of organisms including vertebrates, plants, and insects, and are postulated to be involved in the process of magnetoreception in animals, such as the European robin or fruit flies. [7, 20, 59] A light induced radical pair (RP) mechanism involving a highly conserved Tryptophan (Trp, W) electron-transfer (ET) chain and a flavin adenine dinucleotide (FAD) cofactor is believed to lie at the heart of the magnetic sensitivity of the photochemistry observed in Crys *in vitro* (see Figure 3-1).[7, 59]

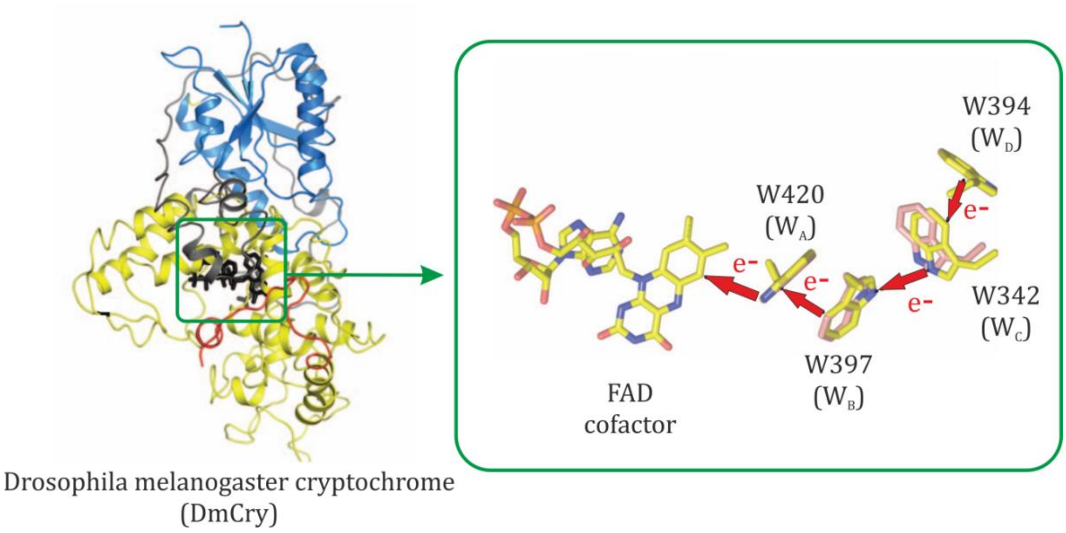

Figure 3-1: Crystal structure of *Dm*Cry with a detailed illustration of the relative arrangement of the non-covalently bound FAD and the ET chain comprised of four Trps (W). Adapted with permission from Zoltowski *et al.* and Levy *et al.*[79-80]

Figure 3-2 shows the proposed photoreaction cycle appropriate for *Dm*Cry.[59] Absorption in the first absorption band, in the blue region of the visible spectrum around 450 nm leads to the excited singlet state of the flavin ($^1F^*$). The nearest Tryptophan (Trp, W) of a highly conserved ET chain, comprised of three or four Trp (W_A, W_B, W_C, and potentially W_D), readily reduces the $^1F^*$ within 0.1-1 ps creating a radical pair, RP1, comprised of the anionic F radical ($F^{\bullet-}$) and the cationic Trp radical $WH^{\bullet+}$ (see Figure 3-1).[78, 81] This is followed by ET along the chain to form a RP between the flavin and the distal Trp. RP1 is formed in a singlet state, conserving the spin state of its precursor. The coherent interconversion between the S and T states driven by hyperfine interactions is sensitive to magnetic fields. As explained in more detail in Section 1.4, application of a magnetic field leads to the energetic separation of the $T_{+/-}$ states from the S and T_0 state through Zeeman interaction, which decreases the S-T interconversion efficiency. Both $F^{\bullet-}$ (pK_a=8.3) and $WH^{\bullet+}$ (pK_a=4.3) in RP1 can change their protonation state within proteins to form a second longer-lived radical pair, RP2.[15, 53, 57, 81-82] Since back electron-transfer (BET) is spin selective, *i.e.* only spin-allowed from the singlet state, the lifetime of RP1 and the reaction yield of RP2 are sensitive to magnetic fields. Note that, depending on the rate of the ET with respect to the rate of intersystem crossing (ISC), the formation of the excited flavin triplet state ($^3F^*$) competes with the ET to form RP1. Since in the functional state, ET largely outcompetes ISC, for clarity the reaction pathway via $^3F^*$ is not illustrated in the reaction scheme.

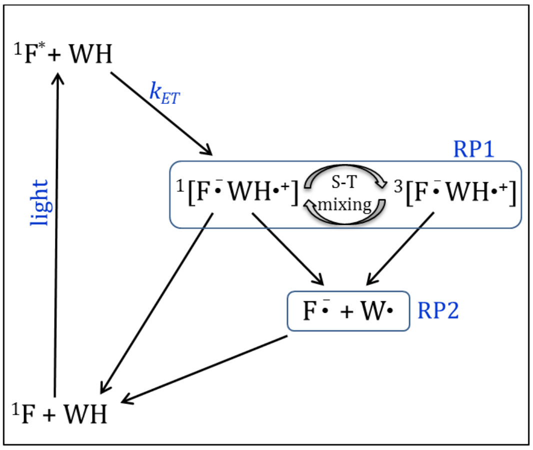

Figure 3-2: Photochemical reaction scheme appropriate for *Dm*Cry WT. Upon light excitation of the flavin ground state (^1F), $^1F^*$ is formed and subsequently reduced by a nearby WH to form RP1: $^1[F^{\bullet -}\ WH^{\bullet +}]$. RP1 undergoes magnetically sensitive coherent singlet-triplet mixing. Since charge recombination occurs only from the singlet state, an external magnetic field has an effect on both the lifetime of RP1 and the quantum yield of RP2.[83]

In this chapter, the photochemistry and magnetic field effects of *Er*Cry4, *Dm*Cry, and *At*Cry1 are investigated using a pulsed cavity enhanced TA technique (CRDS). This application of CRDS to measuring MFEs in proteins is unique to this research group. In the case of *Dm*Cry and *At*Cry1 the results are contrasted with literature results from conventional TA studies conducted previously.[15, 58-59] *Er*Crys have until recently believed to be vestigial flavoproteins and not to bind FAD.[84] Only very recently has expression of *Er*Cry4 with bound FAD been successful, and these are the first MFE studies on this system.[84]

The main aspects of this chapter are the identification of the photochemical reaction cycle, the effects of magnetic fields on the reactivity of avian cryptochrome (*Er*Cry4), and comparison with the photochemistry of insect (*Dm*Cry) and plant cryptochrome (*At*Cry1). In addition to the wild-type (WT) proteins, mutated *Er*Cry4 and *Dm*Cry are investigated, in which a single Trp within the Trp-tetrad was replaced by phenylalanine in order to shed light on the role of the distal and second to distal Trp (*i.e.* W_D and W_C).

In the first section of this chapter (3.1), global target analysis of time and wavelength resolved differential absorbance (ΔA) data is used to identify transient species and to quantify the kinetic processes for both *Dm*Cry and *Er*Cry4 in detail. In the second section (3.2) the effects of magnetic fields on the photochemistry of *Dm*Cry and *Er*Cry4 are investigated. In Section 3.3 the differences in the photochemistry and the MFEs of *At*Cry1, *Er*Cry4, and *Dm*Cry are highlighted and the results are summarized in Chapter 3.4.

Work presented in this chapter has been conducted in collaboration with undergraduate students Thomas Spearman and Jessica Walton.

3.1 Photochemistry of *Dm*Cry and *Er*Cry4

To gain insight into the photochemical properties of *Dm*Cry and *Er*Cry4, time and wavelength resolved ΔA data was analysed globally, as described in Section 2.2, using a spectral model.

In Section 3.1.2 and 3.1.3 time and wavelength resolved ΔA data of *Dm*Cry and *Er*Cry4 respectively are analysed, using a spectral model described in Section 3.1.1, to identify the transient species involved in the photochemical reaction cycle and to estimate the kinetics of relevant reaction processes. In Chapter 3.1.2 a comparison with literature results on *Dm*Cry is of particular interest. The primary focus of the *Er*Cry4 study presented in Section 3.1.3 is the identification of the transient species, since this is the first TA study on *Er*Cry4 and the first investigation of the *Er*Cry4 photoreaction cycle.

In both Sections 3.1.2 and 3.1.3 the results found for the WT Crys are compared to the results of the mutated Crys. The W_D deficient mutants (*Dm*Cry W394F and *Er*Cry4 W369F) exhibit ΔA similar to the WT Crys and are compared directly. In W_C deficient mutants (*Dm*Cry W342F and *Er*Cry4 W318F), in which the ET chain is interrupted, markedly different ΔA is observed, hence these are discussed separately. See Section 2.4.1 for more details on the cryptochrome WT and mutants.

3.1.1 Reference spectra employed in the spectral analysis

Figure 3-3 shows normalized absorbance spectra of the transient species used as reference spectra (ε_{i}.) taken from the literature (see figure caption for details).[57-58, 69, 82, 85-86]

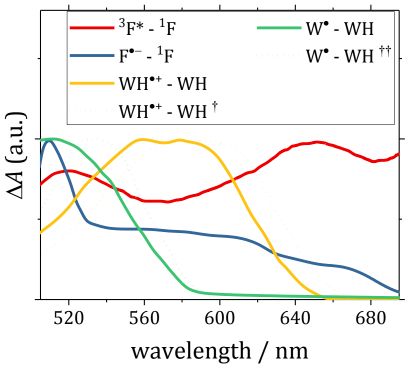

Figure 3-3: Literature reference spectra normalized to the respective highest absorbance intensity of the illustrated wavelength region (510 nm - 690 nm). The spectra of the excited triplet state difference spectrum of FMN bound inside the light-oxygen-voltage domain 1 (LOV1) of a *Chlamydomonas reinhadtii* (Cr) phototropin is shown in red; The difference spectrum of $F^{\bullet-}$ bound inside *Dm*Cry WT is shown as blue solid lines, the difference spectra of $WH^{\bullet+}$ and $W^{\bullet}$ *aq.* as yellow and green solid lines respectively.[69, 85-86] The reference spectra of $WH^{\bullet+}$ and $W^{\bullet}$ measured by Solar *et al.* have previously been used to analyse Trp radicals in *Dm*Cry WT.[58] The dotted green line represents the differential absorbance spectrum of $W^{\bullet}$ observed in CrLOV1.[57] The dotted yellow line represents the difference spectrum of $WH^{\bullet+}$ measured by Solar *et al.* in aqueous solution shifted towards longer wavelengths by 15 nm to account for the enzymichromic shift observed in *Er*Cry4 WT.

The measured $\Delta A(t)$ spectra of *Dm*Cry WT, *Dm*Cry W342F, and *Er*Cry4 W318F presented in this chapter can be fitted satisfactorily using the reference spectra shown as solid lines in Figure 3-3 as a basis for the spectral model described in Section 2.2.

The ΔA spectra of *Dm*Cry W394F (*c.f.* Figure 3-4B) and *Er*Cry4 W369F (*c.f.* Figure 3-5B) exhibit a small absorbance feature peaking around 540 nm. This shoulder cannot be explained based solely on the reference spectra for flavin and Trp species observed in either *Dm*Cry or *Er*Cry4 WT. Instead the additional absorbance maximum matches that of an absorbance feature previously observed in CrLOV1, and has been assigned to the neutral Trp radical ($W^{\bullet}$).[57, 78, 85] This absorbance feature peaking around 540 nm observed in *Dm*Cry W394F and *Er*Cry4 W369F is therefore tentatively assigned to $W^{\bullet}$, and the literature spectrum of $W^{\bullet}$ measured by Langenbacher *et al.* is used as reference spectrum (see green dotted line in Figure 3-3).[57] Differences in the absorbance spectra of $W^{\bullet}$ between the mutants W394F and *Er*Cry4 W369F and the respective WT are not surprising, given that Trp radicals are known to exhibit strong enzymichromic shifts and the $W^{\bullet}$ observed in the WT is predominantly located on W_D, which is replaced by phenylalanine in the W394F.[70-72, 87] Consequently the $W^{\bullet}$ observed in W394F, likely $W_C^{\bullet}$, is at a different position and subject to a different environment than the $W_D^{\bullet}$ radical in *Dm*Cry WT.

In cryptochromes, a dominant ΔA feature with a broad peak centred around 570 nm is often observed, decaying on a µs-time scale, and is typically attributed to $WH^{\bullet +}$.[15, 58-59, 78] In *Er*Cry4 WT (see Figure 3-5A) a similar feature shifted by ~15 nm with respect to the $WH^{\bullet +}$ reference spectrum by Solar *et al.* is observed.[69] Using the reference spectrum for $WH^{\bullet +}$ (solid yellow line in Figure 3-3), which worked well for *Dm*Cry WT, did not lead to a satisfactory fit for the *Er*Cry4 WT data (dotted line in Figure 3-5A). The clear discrepancy between the fit and the data is attributed to an enzymichromic shift of the $WH^{\bullet +}$ spectrum observed in *Er*Cry4 WT with respect to that measured by Solar *et al.* Enzymichromic shifts of up to ±20 nm are commonly observed in Trp radicals.[70-72, 87] The yellow dotted line in Figure 3-3 shows the $WH^{\bullet +}$ reference spectrum shifted by +15 nm. This spectrum is used for $WH^{\bullet +}$ in the spectral model for *Er*Cry4 WT.

In some cryptochromes (*e.g.* in *At*Cry1) protonation of the radical $F^{\bullet -}$ can lead to the formation of a relatively stable radical pair involving the neutral F radical ($FH^{\bullet}$), whose absorbance spectrum is similar to $WH^{\bullet +}$ around 570 nm.[53, 57] In Cry, $FH^{\bullet}$ is not typically formed as part of RP1 via hydrogen atom-transfer, but rather by protonation of $F^{\bullet -}$ creating a more stable RP2.[15, 53, 57] This mechanism, however, is not consistent with the evolution of this spectral feature with time, as observed here. The feature is dominant at early times, but exhibits a relatively short lifetime compared to other spectral features, and does not contribute significantly to the long-lived spectral component associated with RP2 (see Figure 3-5A). Consequently the absorbance feature around 570nm is assigned to $WH^{\bullet +}$ instead.

3.1.2 Spectral analysis of *Dm*Cry

The Δ*A* spectra recorded at various PPD times are shown in Figure 3-4 for A) *Dm*Cry WT, B) *Dm*Cry W394F, and C) *Dm*Cry W342F.[i] The solid lines represent the fit spectra ($S_{\mathrm{fit}(c)}$), and the temporal evolution of the relative contribution of each species to the overall Δ*A* is shown in Figure 3-4D) *Dm*Cry WT, E) *Dm*Cry W394F, and F) *Dm*Cry W342F, as estimated through global target analysis. They are presented as the absorbance contributed by each species integrated over the wavelength range of the measurement and are therefore directly proportional to the concentration of each species (see Section 2.2 and 3.1.1 for more detail).

3.1.2.1 Spectral analysis of DmCry WT & DmCry W394F

The results of the global target analysis for *Dm*Cry WT, shown in Figure 3-4D, are in good agreement with the results of previous TA studies on *Dm*Cry WT.[58-59] The results for both *Dm*Cry WT and the W_D deficient mutant, *Dm*Cry W394F, are consistent with the proposed photo-reaction cycle (see Figure 3-2).

In both the WT and the W394F mutant, $F^{\bullet-}$ and $WH^{\bullet+}$ are the predominant absorbers at 0.5 μs PPD time, consistent with rapid ($k_{\mathrm{ET}} \gg 1\ \mu s^{-1}$) RP1 formation. Note that the contribution of $F^{\bullet-}$ in the WT at 0.5 μs is almost three times larger than in the mutant W394F. This indicates a lower quantum yield of RP1 in the *Dm*Cry W394F, or that charge recombination in the RP1 of the mutant W394F is taking place at a higher rate, or both. In *Dm*Cry WT the $WH^{\bullet+}$ concentration decreases with a lifetime of approximately 8.6 ±1.4 μs while the concentration of $W^{\bullet}$ increases on the same timescale, consistent with the proposed RP2 formation through deprotonation of the $WH^{\bullet+}$.[j] The same process is observed in *Dm*Cry W394, but significantly faster (see Figure 3-4E). Given that only the first data point (at 0.5 μs) shows any contribution of $WH^{\bullet+}$ suggests a $WH^{\bullet+}$ lifetime <1 μs and that the majority of $WH^{\bullet+}$ has already decayed on a sub-microsecond timescale.

---

[i] The Δ*A* spectra in Figure 3-4 show the average of A) 7, B) 6, and C) 12 consecutively recorded Δ*A* spectra, respectively. The error bars represent one standard error of the mean.

[j] The lifetime of $WH^{\bullet+}$ in DmCry WT is estimated by fitting the respective $WH^{\bullet+}$ concentration time profile to a single exponential decay function assuming that the RP1 formation is complete before 0.5 μs and considering the two decay channels for $WH^{\bullet+}$ (deprotonation and charge recombination) as illustrated in Figure 3-2 (see yellow solid line in Figure 3-4D).

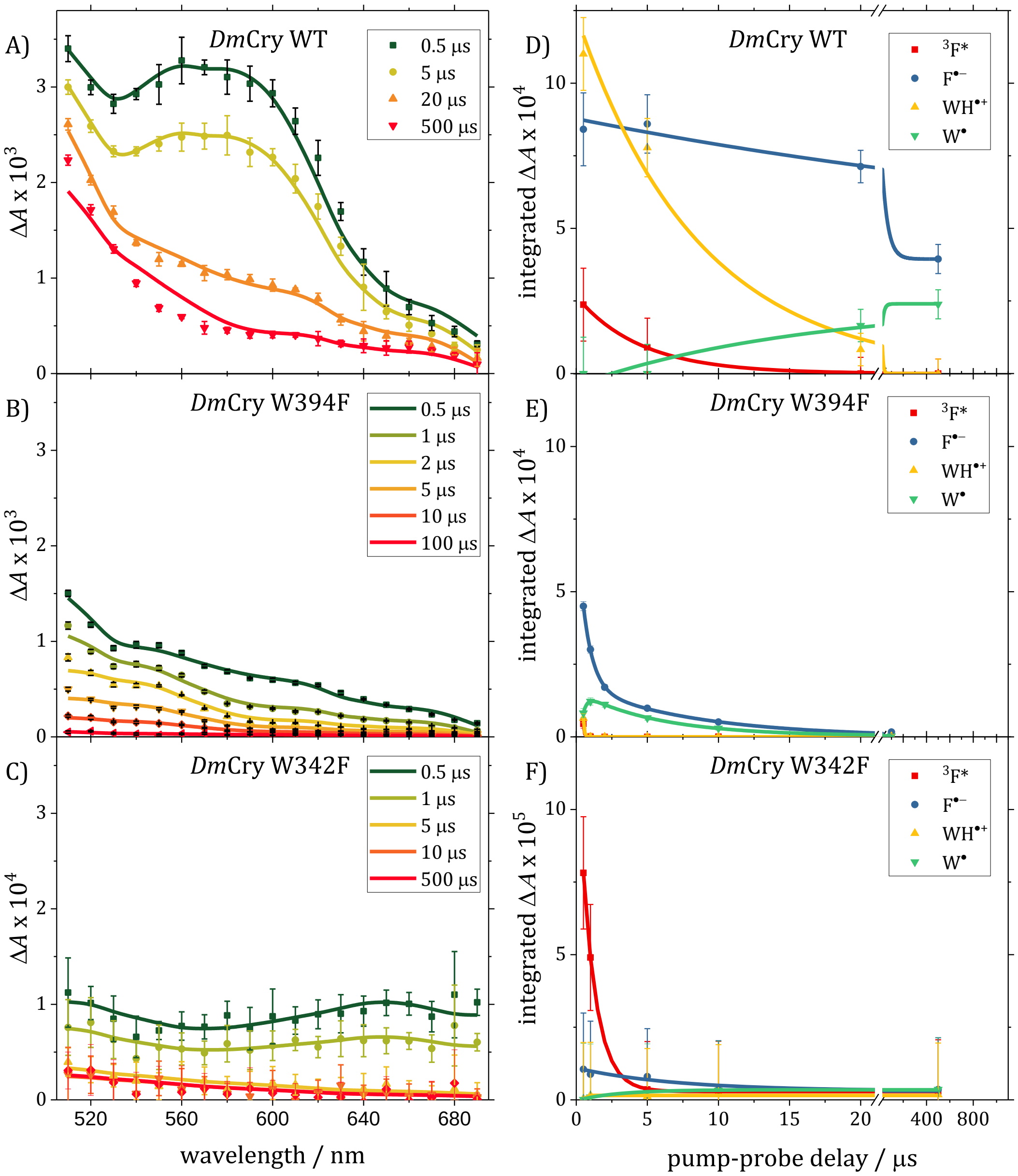

Figure 3-4: ΔA spectra of A) *Dm*Cry WT, B) *Dm*Cry W394F, and C) *Dm*Cry W342F recorded under standard conditions (see Table 2-1) as a function of PPD time. Error bars represent one standard error of the mean (SEM). The solid lines illustrate the fit spectra calculated using the global target analysis method described in the text (see Section 2.2 and 3.1.1). The contribution coefficients (c_i) resulting from the global analysis are shown as symbols in D), E), and F). Error bars represent the estimated standard deviation. Solid lines are exponential fits to estimate the lifetimes of the individual species - see text for more details. To aid comparison the y-axis scales for A) and B) as well as for D) and E) are kept identical, while the scale is increased by an order of magnitude for C) and F) with respect to A) and D).

In *Dm*Cry WT the lifetime of RP2, comprised of $F^{\bullet-}$ and $W^{\bullet}$, exceeds the time frame of the experiment, and a large contribution of both species is observed after 1 ms (see Figure 3-4D). In *Dm*Cry W394F, $F^{\bullet-}$ and $W^{\bullet}$ are the dominant absorbing species, supporting the proposed identity of RP2 (see Figure 3-4E). The lifetime of the RP2 in *Dm*Cry W394F is approximated by fitting the contribution of $F^{\bullet-}$ to a biphasic exponential. This simplistic model of a biphasic decay of $F^{\bullet-}$ accounts for the comparatively short lifetime of RP1 with the first decay component and the longer lifetime of RP2 with the second. While this approach does not account for the fact that the changing concentration of the respective Trp radical pair partner influences the observed decay rate of $F^{\bullet-}$, it still allows for a rough estimate of the observed lifetime of $F^{\bullet-}$: 8.1 ±3.3 µs. This demonstrates a much shorter lifetime of RP2 in *Dm*Cry W394F compared to *Dm*Cry WT, where a significant fraction of $F^{\bullet-}$ (50%) is still present after 500 µs. This is consistent with the hypothesis that replacing W_D with phenylalanine in *Dm*Cry leads to a decrease in the lifetime of the flavin-Trp radical pair due to a decrease in distance between the FAD and the distal W of the ET chain.

These findings on *Dm*Cry WT and *Dm*Cry W394F are in qualitative agreement with the literature, although comparability is limited due to differences in experimental conditions and applied methods.[58-59, 78]

3.1.2.2 Spectral analysis of DmCry W342F

The ΔA observed in the W_C deficient mutant, *Dm*Cry W342F, is approximately an order of magnitude smaller than in *Dm*Cry WT (compare Figure 3-4A and C). Global target analysis results show that a large fraction (~90%) of the ΔA in the observed wavelength region can be assigned to $^3F^*$ (see Figure 3-4F). Although the low signal to noise ratio prohibits a detailed analysis, there is a clear change in the shape of the ΔA spectrum from a broad featureless spectrum at 0.5 µs, similar to ΔA spectra typical for $^3F^*$, to a spectral shape resembling that of flavin and Trp radicals between 5-500 µs. This and the fact that the ΔA signal exhibits a lifetime exceeding the time frame of the measurement (1 ms) provides some evidence for the formation of a long-lived RP2 comprising $F^{\bullet-}$ and $W^{\bullet}$, albeit at a yield more than an order of magnitude smaller than in the *Dm*Cry WT.

3.1.3 Spectral analysis of *Er*Cry4

The Δ*A* recorded at a series of PPD times are shown in Figure 3-5 for A) *Er*Cry4 WT, B) *Er*Cry4 W369F, and C) *Er*Cry4 W318F.[k] The solid lines represent the fit spectra ($S_{\mathrm{fit}(c)}$). The temporal evolution of the relative contribution (c_i) of each species *i* to the overall Δ*A* is shown in Figure 3-5D) *Er*Cry4 WT, E) *Er*Cry4 W369F, and F) *Er*Cry4 W318F, as estimated through global target analysis using the following spectral model described in Section 2.2 and 3.1.1. The c_i represent the Δ*A* contributed by each species integrated over the wavelength range of the measurement and therefore reflect the change in concentration of the individual species with time.

3.1.3.1 Spectral analysis of ErCry4 WT & ErCry4 W369F

The Δ*A* spectra of *Er*Cry4 WT and the W_D deficient mutant, *Er*Cry4 W369F, shown in Figure 3-5A and B respectively, are remarkably similar to their *Dm*Cry analogues (*c.f.* Figure 3-4A and B). Likewise, results of the global analysis of *Er*Cry4 WT and *Er*Cry4 W369F are consistent with the reaction scheme proposed for *Dm*Cry WT (see Figure 3-2), albeit with different lifetimes associated with the individual transient species.

---

[k] The Δ*A* spectra in Figure 3-5 show the average of A) 4, B) 6, and C) 12 consecutively recorded Δ*A* spectra, respectively. The error bars represent one standard error of the mean.

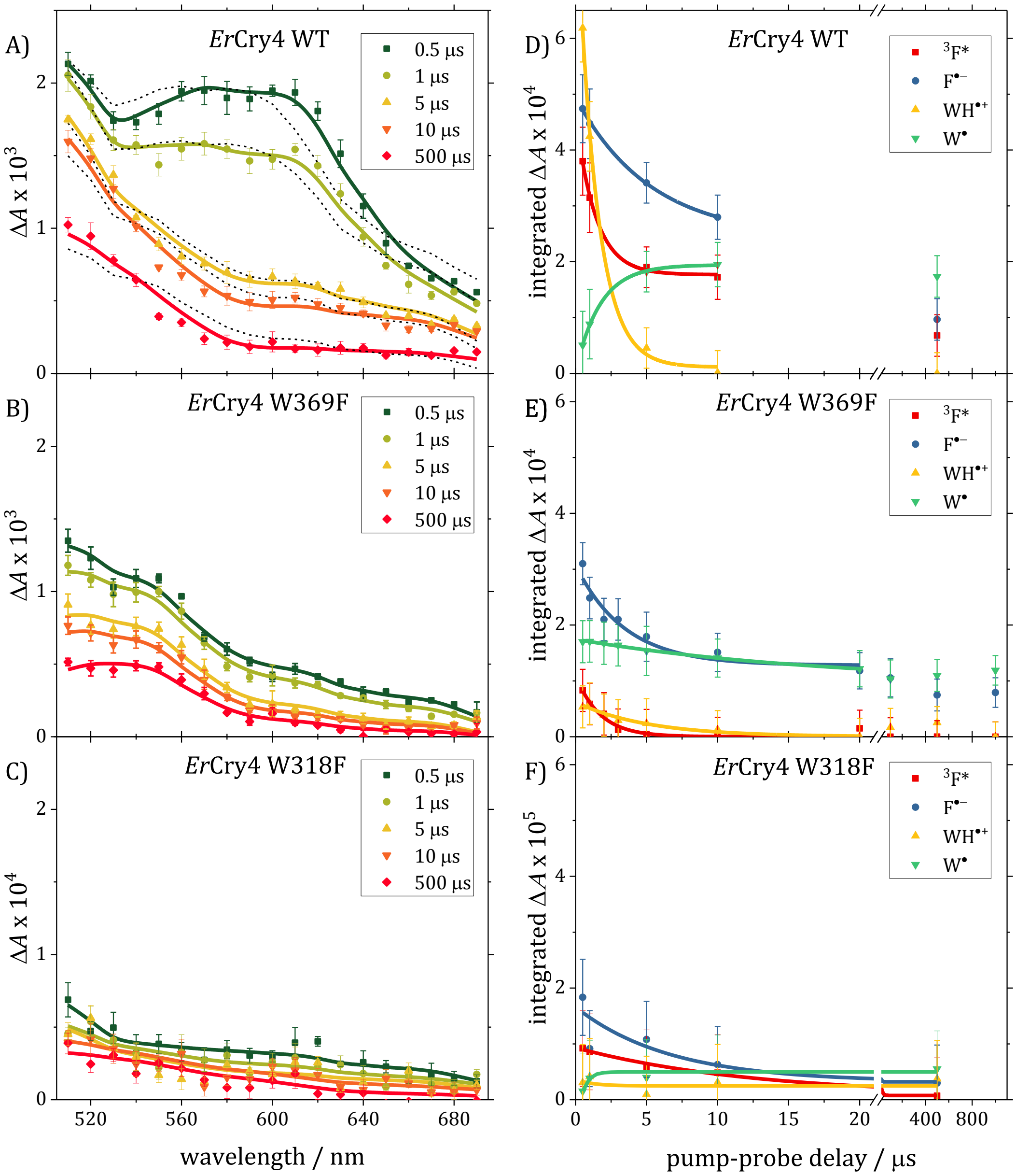

Figure 3-5: ΔA spectra of A) *Er*Cry4 WT, B) *Er*Cry4 W369F, and C) *Er*Cry4 W318F recorded under standard conditions (see Table 2-1). Error bars represent one SEM. Solid lines illustrate the fit spectra calculated using global target analysis (see Section 2.2). The dashed lines in A) represent the fit spectra using the reference spectra shown as solid yellow line in Figure 3-3 for $WH^{\bullet +}$ (see text). The contribution coefficients (c_i) resulting from the global analysis are shown as symbols in D), E), and F). Error bars represent the estimated standard deviation. Solid lines are exponential fits to estimate the lifetimes of the individual species (see text). To aid comparison, the *y*-axis for A) and B) as well as for D) and E) are kept identical, while the scale is increased by an order of magnitude for C) and F) with respect to A) and D).

In general, the temporal evolution of the concentration of all species is consistent with the proposed model, including a relatively short-lived RP1 and a longer lived RP2 state.

In *Er*Cry4 WT, the earliest spectrum, recorded at 0.5 μs PPD time, shows $F^{\bullet-}$ and $WH^{\bullet+}$ contributing the most strongly to the overall absorbance, reflecting the RP1 [$F^{\bullet-}$ $WH^{\bullet+}$] formation on a timescale much faster than this experiment ($k_{ET} \gg 1$ μs). The $WH^{\bullet+}$ in *Er*Cry4 WT decays with a rate constant of 0.73 ±0.10 μs^{-1} (lifetime of 1.4 ±0.2 μs), accompanied by an increase in $W^{\bullet}$ concentration with a rate constant of 0.57 ±0.05 μs^{-1}.[1] This is consistent with the proposed formation of $W^{\bullet}$ through deprotonation (see Figure 3-2) and lends support to the assignment of the respective Trp radical spectra. The similarity of the rates suggests that the deprotonation of $WH^{\bullet+}$ to form $W^{\bullet}$ (*i.e.* RP2) is much faster than the charge recombination of RP1. This, in turn, is consistent with the previous observation that the lifetime of $WH^{\bullet+}$ is much shorter than that of $F^{\bullet-}$. In Figure 3-6, the temporal evolution of the contribution of $WH^{\bullet+}$ is illustrated for both *Er*Cry4 WT and *Dm*Cry WT for direct comparison. It is immediately clear that the lifetime of $WH^{\bullet+}$ in *Er*Cry4 WT is significantly shorter than the lifetime in *Dm*Cry WT. The lifetime of $WH^{\bullet+}$, *i.e.* RP1, reflects the combined rate of BET in RP1 and deprotonation of $WH^{\bullet+}$. The absolute and relative rates of BET in RP1 and deprotonation are likely to have a decisive effect on the MFE in cryptochromes, as will become clearer in the following Section 3.2.

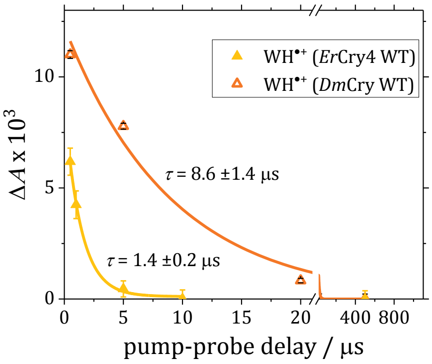

Figure 3-6: Direct comparison of the contribution coefficients (c_i) of *Er*Cry4 WT (solid yellow triangles) and *Dm*Cry WT (open orange triangles) presented previously as part of Figure 3-4D and Figure 3-5D respectively. Error bars represent the estimated standard deviation. The solid and dashed lines are exponential fits to estimate the lifetimes of the individual species with the respective lifetimes shown in the figure.

---

[1] Both rate constants were estimated by fitting the temporal evolution of the $WH^{\bullet+}$ and $W^{\bullet}$ contribution with single exponential functions; see solid yellow and green lines in Figure 3-5D.

In the mutant *Er*Cry4 W369F, the earliest Δ*A* spectrum, recorded at 0.5 μs PPD time, is dominated by the contributions of $F^{\bullet-}$ and $W^{\bullet}$ (see Figure 3-5B and E). This suggests both a rapid RP1 formation as well as a fast deprotonation of the majority of $WH^{\bullet+}$ on a sub-microsecond timescale.

Note that the results of the spectral analysis presented in Figure 3-5E suggest that a fraction of the initially formed $WH^{\bullet+}$ decays on a microsecond timescale with a lifetime of 5.1 ±1 μs. At first glance this seems in conflict with the previous observation of fast deprotonation of $WH^{\bullet+}$ to form $W^{\bullet}$ within 1 μs, but can be rationalized considering the fact that the RP is formed between the flavin and a Trp of a Trp-triad (F - W_A - W_B - W_C). Following the reduction of $^1F^*$ by W_A, an electron is transferred back and forth between the Trp amino acids W_A, W_B, and W_C. The likelihood of the electron hole being localized on any one Trp of the Trp-triad depends on the relative forward and back ET rate constants between W_A, W_B, and W_C. Furthermore, the acidity of amino acids and their deprotonation rate constants depend strongly on the local protein environment. The deprotonation of a flavin-Trp RP, which is more precisely a distribution of radical pairs, including $[F^{\bullet-}\ WH_A^{\bullet+}]$, $[F^{\bullet-}\ WH_B^{\bullet+}]$, and $[F^{\bullet-}\ WH_C^{\bullet+}]$, would therefore not necessarily lead to the observation of a single exponential decay following the first order rate law.

The contribution of $F^{\bullet-}$ at 0.5 μs PPD time is only 1.5 times larger in *Er*Cry4 WT than in *Er*Cry4 W369F, suggesting comparable quantum yields of RP1 in *Er*Cry4 W369F and the WT (see Figure 3-5D and E). Global analysis of *Er*Cry4 W369F shows that the concentration of $F^{\bullet-}$ and $W^{\bullet}$ does not decrease significantly between 0.1 and 1 ms. In contrast to the DmCry mutant analogue DmCry W394F, ErCry4 W369F forms a relatively stable RP2, comprised of $F^{\bullet-}$ and $W^{\bullet}$. The lifetime of this RP2 exceeds the observed time frame of the experiment (0.5 μs - 1 ms).

A large fraction (~25% at PPD time 0.5 μs) of the Δ*A* spectra of *Er*Cry4 WT can be assigned to $^3F^*$ (see Figure 3-5D). This is surprising since in cryptochromes and other flavoproteins the dominant quenching pathway of the excited singlet state $^1F^*$ is by ET from a nearby amino acid on a femtosecond to picosecond timescale, efficiently outcompeting intersystem crossing.[25, 81, 83, 88-90] Consequently, singlet-born radical pairs are usually observed in cryptochromes and other flavoproteins.[15, 53, 59-60, 62] In unpublished picosecond transient absorbance experiments performed in this group, the formation of $^3F^*$ has been linked to the decay of $^1F^*$, supporting the proposed formation of $^3F^*$ from $^1F^*$ through ISC.

The observation of ^{3}F* suggests that a significant fraction of *Er*Cry4 WT is in an inactive state in which fast ET is inhibited. Note that only ~10% of the of the Δ*A* spectra of *Dm*Cry WT is assigned to ^{3}F* (see Figure 3-4D).

3.1.3.2 Spectral analysis of ErCry4 W318F

At 0.5 µs PPD time, the Δ*A* signal and the estimated $F^{\bullet-}$ concentration (see Figure 3-5C and F) are more than an order of magnitude smaller in the W_C deficient mutant, *Er*Cry4 W318F, than in *Er*Cry4 WT. The behaviour of the *Er*Cry4 W318F mutant exhibits striking similarities with its *Dm*Cry analogue *Dm*Cry W342F (see Figure 3-4F). The global analysis reveals a long–lived spectral component, assigned to the sum of both $F^{\bullet-}$ and $W^{\bullet}$, which does not decay significantly between 10 and 500 µs. Although the low signal to noise ratio prohibits an unambiguous assignment, the results suggest that, in *Er*Cry4 W318F, a radical pair, likely comprised of $F^{\bullet-}$ and $W^{\bullet}$, is formed at a yield more than an order of magnitude lower than in *Er*Cry4 WT.

3.2 Effects of magnetic fields on the photochemistry of *Dm*Cry and *Er*Cry4

In order to investigate the effects of weak magnetic fields (1-30 mT) on the photochemistry of *Dm*Cry and *Er*Cry4, the Δ*A* of *Dm*Cry and *Er*Cry4 were investigated a) by comparing the temporal evolution of the Δ*A* at 0 and 30 mT and b) by measuring the magnetically altered reaction yield (MARY) as a function of magnetic field. See Section 2.3 for more details on the employed methods for the quantification of MFEs. Quantifying differences in the temporal evolution of Δ*A* recorded at *B* = 0 or 30 mT provides insight into the changes in reaction kinetics upon application of an external magnetic field, while MARY spectra recorded as a function of magnetic field *B* can give direct insight into the spin dynamic processes and interactions such as spin relaxation and the hyperfine interactions of the radical pairs.

3.2.1 Time dependence of the Δ*A* and MFEs in *Dm*Cry and *Er*Cry4

The temporal evolution of Δ*A* at *B* = 0 mT and 30 mT applied external magnetic field was studied at two different wavelengths: 600 nm (Δ*A*(600 nm)), where $WH^{\bullet+}$ exhibits the strongest absorbance, and 530 nm (ΔA(530nm)) where all species of interest ($WH^{\bullet +}$, $W^{\bullet}$, $F^{\bullet -}$ and $^3F^*$) absorb similarly (see Figure 3-3).

As in Section 3.1, the results for *Dm*Cry are presented first (Section 3.2.1.1) followed by that of the *Er*Cry4 (Section 3.2.1.2). Analogously to the structure of Section 3.1 the WT Cry and the W_D deficient mutants are compared directly, while the W_C deficient mutants are treated separately.

The approach and analysis method is explained here as introduction to the discussion of the results presented in the following two sections.

Consistent with the suggested photocycle (see Figure 3-2) and the results of the Section 3.1, the evolution of the ΔA observed at both 530 nm and 600 nm show a clear (at least) biphasic decay in the WT and W_C deficient mutants of *Dm*Cry and *Er*Cry4 (see Figure 3-7 and Figure 3-9 respectively). The temporal evolution of both ΔA(600 nm) and ΔA(530 nm) can be described well by distinguishing only two decay components with distinct decay times differing by several orders of magnitude. The lifetime of the first decay component (τ_1) is calculated by fitting the ΔA data between the time interval 0.25 µs to 20 µs to a single exponential fit function with constant offset *c*:

$$f_1 = A_1 e^{-t/\tau_1} + c. \tag{3.1}$$

The second decay component of ΔA reflects the lifetime of RP2. To estimate τ_2, the ΔA data was fitted between 0.1 and 1 ms to a single exponential function:

$$f_2 = A_2 e^{-t/\tau_2}. \tag{3.2}$$

The difference in the evolution of the ΔA between 530 nm and 600 nm in time is attributed to the formation of $W^{\bullet}$ from $WH^{\bullet +}$, with absorption maxima around 510 nm and 580 nm respectively. The fast decay component, decaying on a microsecond timescale, reflects the chemical transformation of RP1, *i.e.* the decrease in $WH^{\bullet +}$ concentration, through both deprotonation and BET.[m] Consequently, the lifetime of the early decay component (τ_1) of ΔA(600 nm) reflects the lifetime of RP1.

---

[m] Other processes affecting the temporal evolution of the ΔA at 600 nm, albeit to a much smaller extent, are the decrease in $^3F^*$ and $F^{\bullet -}$ concentration.

Analogously, the lifetime of RP2 can be estimated from τ_2. Since RP2 absorbs more strongly at 530 nm than at 600 nm the τ_2 calculated from ΔA(530 nm) is used to estimate the lifetime of RP2.

The results are summarized in Table 3-1 and Table 3-2 for *Dm*Cry and *Er*Cry4, respectively. Since τ_1 and τ_2 differ by several orders of magnitude, the fraction of the of ΔA decaying with a lifetime τ_2 can be assumed to be constant when calculating τ_1, while the fraction decaying with a lifetime of τ_1 can be assumed to be negligible on the timescale of 0.1 to 1 ms, where τ_2 is calculated.

3.2.1.1 The temporal evolution of the ΔA and MFEs in DmCry

The temporal evolution of ΔA in *Dm*Cry WT & *Dm*Cry W394F

The ΔA observed in *Dm*Cry WT and *Dm*Cry W394F are shown in Figure 3-7A and B as a function of PPD time, respectively.

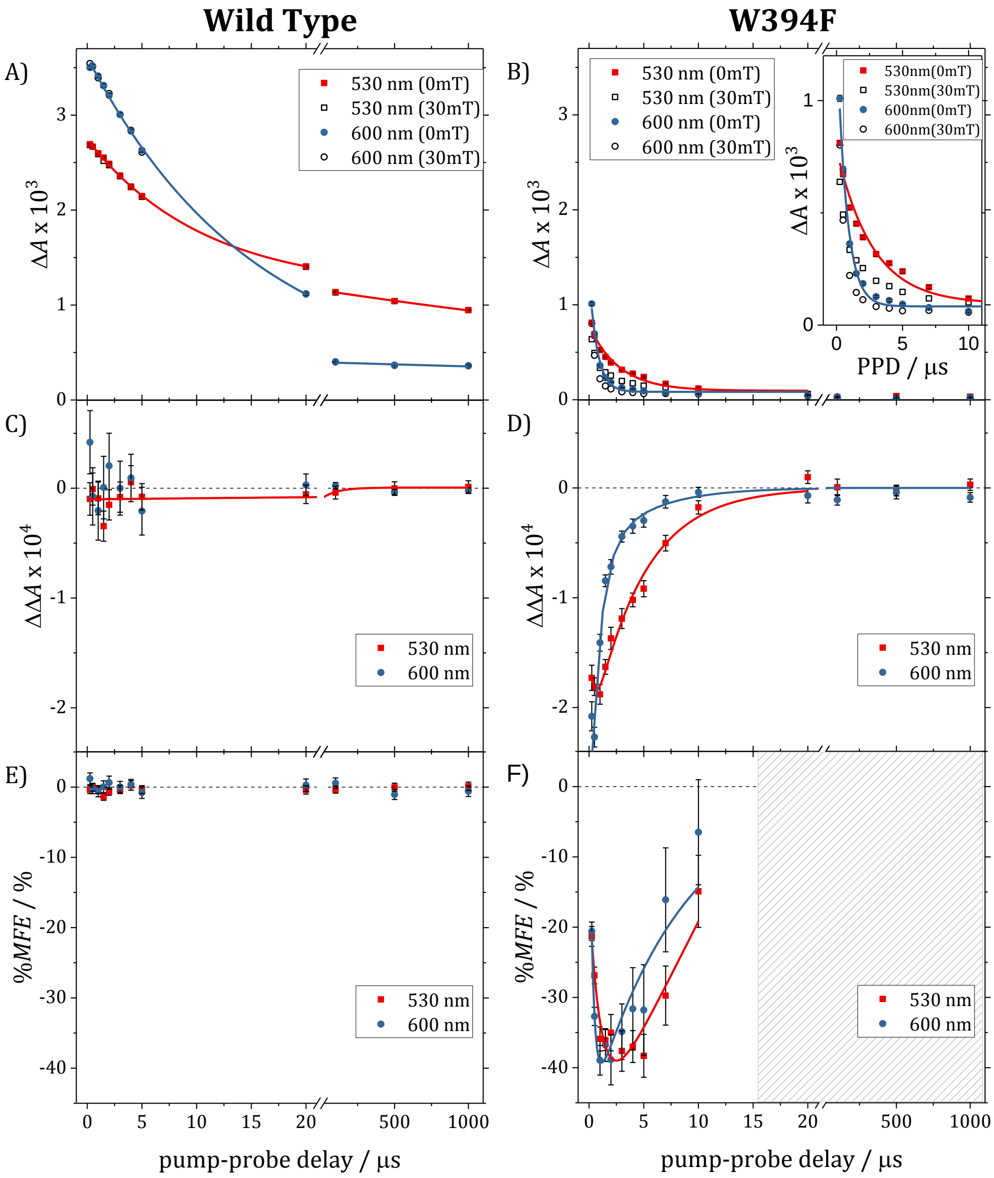

Figure 3-7: A) and B) show the ΔA of *Dm*Cry WT and *Dm*Cry W394F respectively, measured under standard conditions (see Table 2-1). The ΔA at 530 nm (red) and 600 nm (blue) were measured with magnetic field applied (B = 30 mT, solid symbols) and without (B = 0 mT, open symbols).[n] For comparability, the scale of the y-axis of A), and B) are kept identical. The inset in B) shows the data within the first 10 μs on an increased y-scale. Solid lines represent exponential fits, see text for details. C) and D) show the difference ($\Delta\Delta A$) of the ΔA measured at 0 mT and 30 mT at 530 nm (red) and 600 nm (blue). E) and F) show the %*MFE*. The solid lines shown in C), D), and F) are shown to guide the eye. Error bars represent one SEM. For comparability, the scales of the y-axis are kept identical for *Dm*Cry WT and *Dm*Cry4 W394F.

---

[n] Open symbols are often hidden behind solid symbols due to the similarity of their ΔA values.

The first decay component of ΔA(600 nm) exhibits a lifetime of τ_1 = 15.3 ±1.1 μs in *Dm*Cry WT and τ_1 = 0.73 ±0.06 μs in *Dm*Cry W394F (see Table 3-1). The significantly shorter lifetime reflects the shorter lifetime of RP1 in *Dm*Cry W394F as compared to *Dm*Cry WT, consistent with the results from Section 3.1.2.[o]

In *Dm*Cry WT, a large (>40%) fraction of the ΔA(530 nm) decays on a timescale τ_2 = 4.9 ±0.2 ms. In contrast, in the mutant *Dm*Cry W394F only 4% of the initial ΔA(530 nm) remains after 100 μs. While the RP1 in *Dm*Cry WT exhibits a lifetime of only a few microseconds, RP2 lives for several milliseconds. In *Dm*Cry W394F the lifetime of RP1 and RP2 are both significantly reduced compared to *Dm*Cry WT and no significant signal is observed after 1 ms PPD time. These observations are consistent with the proposed photoreaction cycle and the expected effect of replacing the W_D with phenylalanine.

---

[o] While the reported trend is consistent between the two approaches (single wavelength analysis *vs.* global target analysis in Chapter 3.1.2) there is a small discrepancy between the absolute values calculated independently. The lifetime of RP1 estimated in the Chapter 3.1.2 for *Dm*Cry WT is calculated directly from the ΔA associated with $WH^{\bullet+}$, which was extracted from time and wavelength resolved data. At 8.6 ±1.4 μs the lifetime estimated that way is significantly shorter than the lifetime of 15.3 ±1.1 μs estimated through the analysis of the ΔA observed at 600 nm in this section. This discrepancy can be rationalized by considering that the decay of ΔA(600 nm) does not only reflect the decay of $WH^{\bullet+}$ but also the decrease in $^3F^*$ and $F^{\bullet-}$ concentrations. Note that the single wavelength analysis reproduces the expected trend but does not quantify the lifetime of $WH^{\bullet+}$ accurately since it is not the only species with significant absorbance at 600 nm. This demonstrates the advantage of a global spectral deconvolution compared to a single wavelength analysis approach.

Table 3-1: Results of the kinetic analysis of the Δ*A* time traces of *Dm*Cry WT, *Dm*Cry W394F, and *Dm*Cry W342F shown in Figure 3-7 and Figure 3-8 using the Equations 3.1 and 3.2 as fit functions with $k_i = 1/\tau_i$. The uncertainties shown represent one standard deviation.

	***Dm*Cry WT**		***Dm*Cry W394F**		***Dm*Cry W342F**
	530 nm	600 nm	530 nm	600 nm	530 nm
A_1 **×10^5**	158 ±2	340 ±10	69 ±5	120 ±10	5.2 ±2.1
k_1 **/µs^{-1}**	0.094 ±0.004	0.065 ±0.005	0.37 ±0.06	1.4 ±0.1	2.2 ±1.2
τ_1 **/µs**	10.1 ±0.4	15.3 ±1.1	2.7 ±0.4	0.73 ±0.06	0.46 ±0.26
A_2 **×10^5**	116 ±1	40 ±1*	3.1 ±0.7*	2.3 ±2*	1.4 ±0.5*
k_2 **/s^{-1}**	204 ±8	--	--	--	--
τ_2 **/ ms**	4.9 ±0.2	--	--	--	--

*Where an insufficient signal to noise ratios prohibit the quantification of the decay rate k_2 the Δ*A* data between 0.1-1 ms was averaged to obtain values for the magnitude of A_2 instead.

The temporal evolution of MFEs in *Dm*Cry WT & *Dm*Cry W394F

In *Dm*Cry WT, averaging the ΔΔ*A*(530 nm) recorded between 0.25 µs and 20 µs, gives a small ΔΔ*A* field effect of $-(9.6 \pm 3.7) \times 10^{-6}$ or a %*MFE* of −(0.40 ±0.14)% (see Figure 3-7B and C). The negative sign indicates that RP1 is initially formed in a S-state, but the low signal to noise ratio of the ΔΔ*A* prohibits any detailed analysis of its temporal evolution.

By contrast, in *Dm*Cry W394F the ΔΔ*A* is orders of magnitudes larger (see Figure 3-7D). Generally the ΔΔ*A* curves exhibit a complex time dependence, reflecting both the rate constants associated with the chemical transformations of the RP1 species (*e.g.* ET, BET, and deprotonation) as well as parameters governing the ratio of singlet and triplet population of the RP (*e.g.* hyperfine coupling constants and rate of spin relaxation). The ΔΔ*A* exhibits a steep increase in the magnitude to reach a maximum of $-(1.9 \pm 0.1) \times 10^{-4}$ after 1 µs PPD time at 530 nm and a maximum of $-(2.3 \pm 0.1) \times 10^{-4}$ after 0.5 µs at 600 nm followed by a decay back to zero within 20 µs. The sharp initial increase of ΔΔ*A* at both 530 nm and 600 nm can be attributed to the altered S-T population difference of RP1 induced by the application of a magnetic field, leading to a magnetically altered time dependence of the concentration of the SC RP and a magnetically altered yield of downstream photoproducts. The subsequent decrease in the $\Delta\Delta A$(530 nm) signal is attributed to the fact that spin correlation is likely to be lost within less than ~1 µs and that the overall concentration of RP1 deceases rapidly through deprotonation and BET.

The slightly later maximum of the $\Delta\Delta A$(530 nm) signal can be rationalized by the deprotonation of RP1 forming RP2, leading to a further increase of the magnitude of the $\Delta\Delta A$(530 nm) as the MARY of RP1 (absorbing predominantly at 600 nm) is passed on to RP2 (absorbing predominantly at 530 nm). Consequently the $\Delta\Delta A$ at 530 nm reaches its maximum magnitude, which is at 1 µs PPD time, significantly later than at 600 nm. After 1 µs, the formation of RP2 through deprotonation of RP1 is (over-) compensated by the loss of RP2 which leads to the overall decrease of the magnitude of $\Delta\Delta A$(530 nm) after 1 µs PPD time. This is consistent with the proposed photoreaction scheme, the results presented in 3.1.2 and the interpretation of the ΔA time traces shown in Figure 3-4B, where the deprotonation of RP1 to form RP2 is reflected in the faster decay of the ΔA at 530 nm than the ΔA at 600 nm.

The %*MFE*s in both spectral regions are shown in Figure 3.7F. The %*MFE* rises from −20% after 250 ns to a broad maximum of ca. −38% at 2-5 µs. It is noteworthy that in *Dm*Cry W394F the %*MFE* observed in the first 10 µs is an order of magnitude larger than that observed in *Dm*Cry WT.

The magnitude of the %*MFE* is dependent both on the $\Delta\Delta A$ of magnetically sensitive species as well as the overall ΔA caused by all transient species. Therefore the increase in the magnitude of the %*MFE* reflects both MFEs on the SC RP concentration arising from the hyperfine mechanism, and the decrease in the absorbance associated with non-magnetically sensitive transient species such as ^{3}F*. The results from the global analysis in Section 3.1.2 suggest that ^{3}F* is present at high concentrations at early PPD times (<1 µs) and its decrease in concentration within the first microseconds leads to an apparent increase in the overall %*MFE*.

After 10 µs PPD time the magnitude of the %*MFE* decreases to approximately −10%. Assuming spin correlation is largely lost within 1 µs, this decrease is likely to be the result of a relative decrease in the concentration of species with magnetically sensitive concentration with respect to non-magnetically sensitive species. An additional mechanism that can lead to a decrease in the %*MFE* on this timescale, following the loss of spin coherence, is based on the effects of magnetic fields on spin relaxation processes.[76] Evidence for this mechanism and a more detailed description is provided in Section 3.2.3. No %*MFE*s are shown at PPD times larger than 10 μs, as the magnitude of the ΔA is close to zero, division by which lead to unphysical results.

<u>The temporal evolution of ΔA and MFEs in *Dm*Cry W342F</u>

The ΔA and $\Delta\Delta A$ of *Dm*Cry W342F are shown in Figure 3-8A and B, respectively. A biphasic decay of the weak ΔA is observed, with one component decaying with a lifetime of 0.46 ±0.26 μs and a second long-lived component. In contrast to *Dm*Cry WT and *Dm*Cry W394F, $^3F^*$ constitutes the dominant absorber at early PPD times (see Figure 3-4F) and consequently τ_1 does not provide a good estimate for the RP1 lifetime. According to the spectral deconvolution described in Section 3.1.2, the ΔA observed after 10 μs PPD time is likely to be associated with the species $F^{\bullet-}$ and $W^{\bullet}$. The fact that the ΔA between 0.1 to 1 ms is approximately constant is consistent with the hypothesis of the formation of a long-lived RP2.

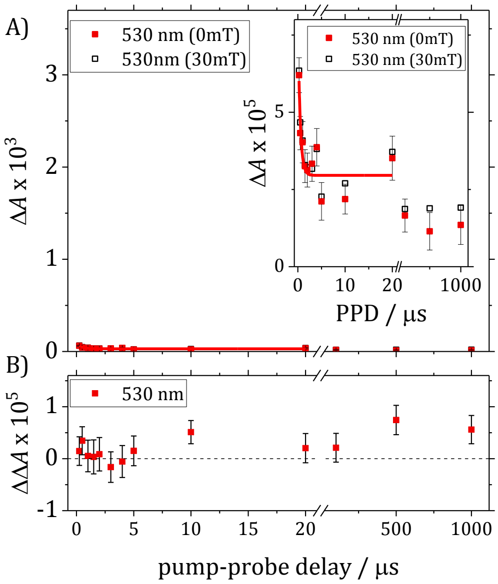

Figure 3-8: A) The Δ*A* of *Dm*Cry W342F measured under standard conditions (see Table 2-1) as a function of PPD time at 530 nm. The Δ*A* was measured with an external magnetic field of *B* = 30 mT applied (open squares) and without *B* = 0 mT (solid red squares). To highlight the difference in the magnitude of the Δ*A* compared to the *Dm*Cry WT, the scale of the *y*-axis is kept identical to the *y*-axis of Figure 3-7A. The inset shows the Δ*A* data on an increased *y*-axis scale. The solid lines represent an exponential fit to the Δ*A* (for details see text). B) The difference (ΔΔ*A*) of the Δ*A* measured at 0 mT and 30 mT presented in Figure 3-8A which reveals no significant MFE in *Dm*Cry W342F.

No significant MFE was detected in *Dm*Cry W342F. The average of the ΔΔ*A* between 0.5-5 µs is $6.5 \pm 5.3 \times 10^{-7}$. But note that due to the low Δ*A* signal, only 3.4×10^{-5} in the PPD time region of 0.5-5 µs, a %*MFE* on the order of several percent cannot be excluded due to the limited signal to noise ratio.

3.2.1.2 The temporal evolution of the ΔA and MFEs in ErCry4

The temporal evolution of Δ*A* in *Er*Cry4 WT & *Er*Cry4 W369F

The Δ*A* in *Er*Cry4, shown in Figure 3-9A and B, for *Er*Cry4 WT and *Er*Cry4 W369F, and Figure 3-10A for *Er*Cry4 W318F, exhibit a similar biphasic temporal evolution as its *Dm*Cry analogues (see Figure 3-7A, B, and Figure 3-8A, respectively). In *Er*Cry4 WT and *Er*Cry4 W369F the change in Δ*A* on a microsecond timescale can be attributed largely to the dynamic processes of RP1, whereas the decay observed on a milliseconds timescale is associated with the decrease of RP2 concentration. Equation 3.1 and 3.2 are used to calculate the lifetime τ_1 and τ_2 of the ΔA observed on distinct timescales: 0.25-20 μs and 0.1-1 ms respectively. The results of the fit are summarized in Table 3-2 and the lifetime τ_1 and τ_2 can be used to approximate the lifetime of RP1 and RP2, respectively. More details on the calculation and assignment of τ_1 and τ_2 can be found at the beginning of Section 3.2.1.

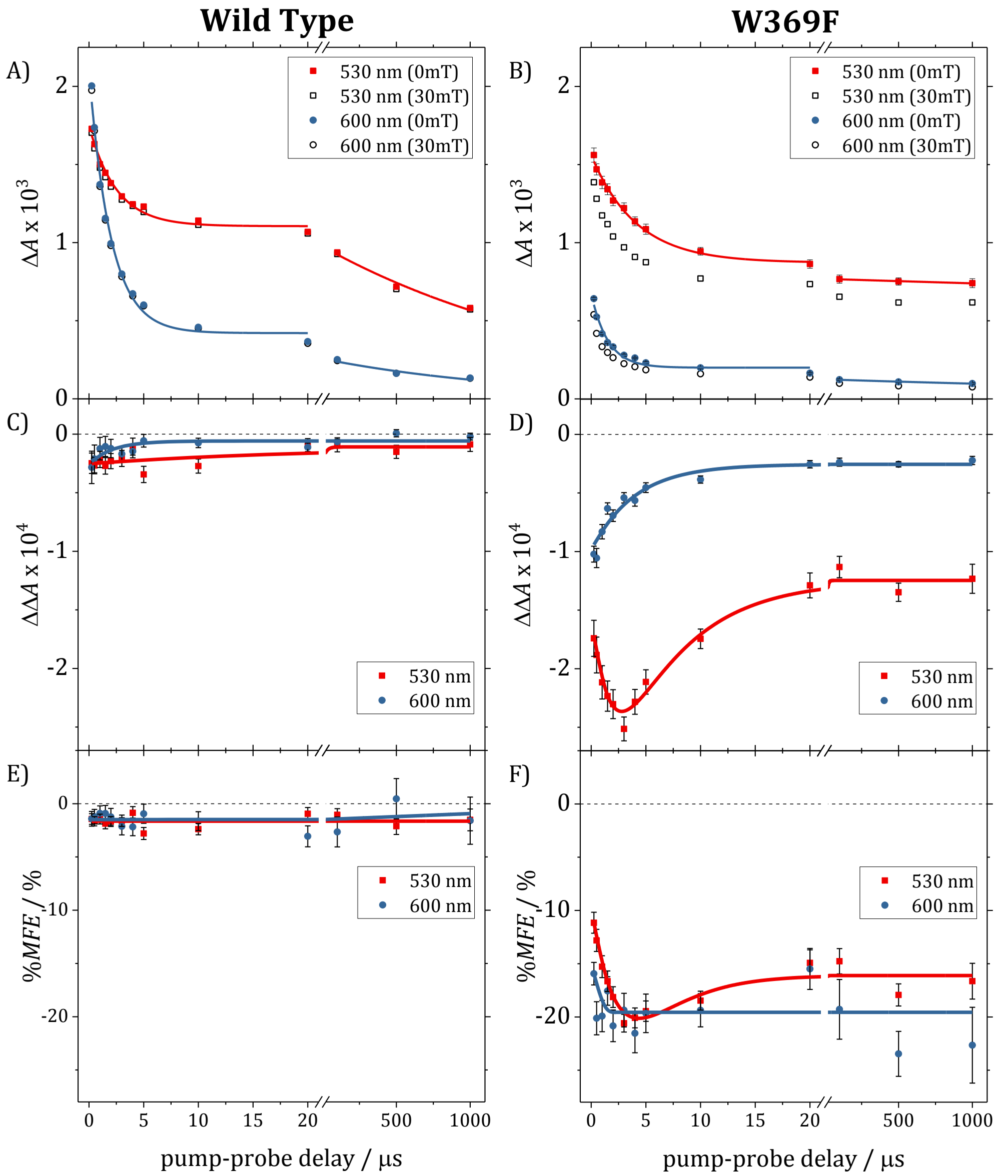

Figure 3-9: A) and B) show the ΔA of *Er*Cry4 WT and *Er*Cry4 W369F respectively, measured under standard conditions (see Table 2-1). The ΔA at 530 nm (red) and 600 nm (blue) was measured with a magnetic field applied (B = 30 mT, solid symbols) and without (B = 0 mT, open symbols)[p]. Solid lines represent exponential fits to the ΔA (for details see the beginning of this section). C) and D) show the subtraction ($\Delta\Delta A$) of the ΔA measured at 0 mT and 30 mT at 530 nm (red) and 600 nm (blue). E) and F) show the ratio (%*MFE*) of the $\Delta\Delta A$ and ΔA at 530 nm and 600 nm. The solid lines in C), D), E), and F) are shown to guide the eye. Error bars represent one SEM. For comparability, the scales of the y-axis are kept identical for *Er*Cry4 WT and *Er*Cry4 W369F.

---

[p] Open symbols are often hidden behind solid symbols and hardly visible

Table 3-2: Results of the kinetic analysis of the Δ*A* time traces of *Er*Cry4 WT, *Er*Cry4 W369F, and *Er*Cry4 W318F shown in Figure 3-9 and Figure 3-10 using the Equations 3.1 and 3.2 as fit functions with $k_i = 1/\tau_i$. The uncertainties shown represent one standard deviation.

	***Er*Cry4 WT**		***Er*Cry4 W369F**		***Er*Cry4 W318F**
	530 nm	600 nm	530 nm	600 nm	530 nm
$\boldsymbol{A_1 \times 10^5}$	64 ±3	168 ±8	69 ±3	47 ±4	6.3 ±0.4
$\boldsymbol{k_1}$ **/μs⁻¹**	0.40 ±0.04	0.50 ±0.04	0.24 ±0.02	0.66 ±0.11	0.8 ±0.4
$\boldsymbol{\tau_1}$ **/μs**	2.5 ±0.3	2.0 ±0.2	4.1 ±0.4	1.5 ±0.3	1.2 ±0.6
$\boldsymbol{A_2 \times 10^5}$	98 ±4	26 ±3	76.8 ±0.3	12.5 ±0.02*	6.3 ±0.4*
$\boldsymbol{k_2}$ **/s⁻¹**	543 ±73	740 ±23	38 ±6	--	--
$\boldsymbol{\tau_2}$ **/ ms**	1.8 ±0.2	1.4 ±0.4	26 ±4	--	--

* The Δ*A* data between 0.1-1 ms was averaged to obtain values for the magnitude of A_2 where insufficient signal to noise ratios prohibit the quantification of the decay rate k_2.

In *Er*Cry4 WT, the early decay component of Δ*A*(600 nm) exhibits a lifetime of τ_1 = 2.0 ±0.2 μs - almost an order of magnitude shorter than the τ_1 observed in *Dm*Cry WT (15.3 ±1.1 μs) reflecting a much shorter RP1 lifetime in *Er*Cry4 WT compared to *Dm*Cry WT. This is in good agreement with the trend calculated independently using the spectral deconvolution method presented in Section 3.1.3.[q]

In *Er*Cry4 WT a significant decrease in the Δ*A*(530 nm) is observed between 0.1 ms and 1 ms with a lifetime of 1.8 ±0.2 ms. Although the results from the spectral deconvolution suggest that some non-negligible amount of the ^{3}F* is present even at late (*e.g.* 0.5 ms) PPD times, the majority of the Δ*A*(530 nm) after 0.1 μs PPD can be attributed to the RP2 instead, considering the respective absorbance spectra. The comparatively fast decay of Δ*A*(530 nm) between 0.1 ms and 1 ms suggests a relatively short RP2 lifetime in *Er*Cry4 WT compared with *Dm*Cry WT.

---

[q] The lifetime of the RP1 is slightly overestimated by analysing the decay of Δ*A* at a single wavelength (τ_1 = 2.0 ±0.2 μs) compared to the results of the global analysis (1.4 ±0.2 μs). This discrepancy reflects the limitation of single wavelength analysis since other species besides the RP1, such as ^{3}F*, contribute to the overall Δ*A*, which may alter the decay rate of the Δ*A*. A significant amount of ^{3}F* is present at early PPD times (Section 3.1.3).

The Δ*A* signal in *Er*Cry4 W369F exhibits an approximately biphasic exponential decay, similar to the results of *Er*Cry4 WT and *Dm*Cry WT. The rate constant of the exponential decay of Δ*A*(600 nm), at early PPD times (k_1), is significantly larger than that of Δ*A*(530 nm), being 0.66 ±0.11 μs^{-1} and 0.24 ±0.02 μs^{-1}, respectively. This reflects a change in the relative absorbance intensities at 530 nm and 600 nm, and suggests a significant change in the relative concentrations of transient species absorbing differently at 530 nm and 600 nm on a microsecond timescale. The absorbance spectra of the transient species likely to be present within the observed time frame are shown in Figure 3-3. $^3F^*$ and $F^{\bullet-}$ exhibit similar absorbance at both 530 nm and 600 nm. In contrast, $WH^{\bullet+}$ exhibits a broad absorbance maximum between 560 nm and 600 nm while the absorbance of $W^{\bullet}$ is negligible at 600 nm. Radicals $WH^{\bullet+}$ and $W^{\bullet}$, absorb strongly at 530 nm. Consequently, the difference in rate constants observed at 530 nm and 600 nm supports the proposed deprotonation of $WH^{\bullet+}$ to form $W^{\bullet}$ (RP1 → RP2) on a microsecond timescale. Additional evidence for this slow deprotonation step is presented in Section 3.1.3, analogous to that in DmCry WT and DmCry W369F (Sections 3.1.2 and 3.2.1) and in the literature.[78]

In *Er*Cry4 W369F, *ca*. 50% of the Δ*A*(530 nm) signal remains constant between 0.1 ms and 1 ms. In contrast, a significant decay was observed on this timescale in *Er*Cry4 WT, and in the *Dm*Cry mutant analogue (*Dm*Cry W394F) only a Δ*A* signal of (3.1 ±0.7) $\times 10^{-5}$, *i.e.* more than an order of magnitude less than in *Er*Cry4 W369F, is observed on that timescale. This suggests both a comparatively high yield of RP2 in *Er*Cry4 W369F and an increased lifetime of the RP2, exceeding the observed timeframe of the experiment (0.25 μs to 1 ms). This is surprising, as replacing W_D by phenylalanine shortens the potential ET chain. Assuming that the electron hole is mostly localized on W_D in *Er*Cry4 WT, a shortening of the ET chain by replacing the W_D by phenylalanine is intuitively expected to lead to a decreased lifetime of the intramolecular RP in the mutant. Note that this trend is observed in *Dm*Cry as a decrease in the lifetime of the transient absorbance signal of *Dm*Cry W394F compared to *Dm*Cry WT, and has been attributed to this effect (see Section 3.1.2).

Replacing W_D by phenylalanine has a dramatic effect on the observed Δ*A* both as a function of time and wavelength. This provides evidence that in *Er*Cry4 WT W_D is involved in the ET cascade following the reduction of $^1F^*$, and is likely the RP partner of the flavin radical in RP1 and RP2. The increased lifetime of RP2 of *Er*Cry4 W369F compared to *Er*Cry4 WT suggests an unexpected stabilization of the flavin-W_C radical pair RP2.

The phenomenon of the long-lived transient species in *Er*Cry4 W369F could alternatively be rationalized by W_C not being the (only) RP partner observed in this experiment. An alternative competing ET pathway might exist, perhaps involving different amino acids when the ET from W_D to W_C is blocked. There is, however, some evidence against this hypothesis. Both the *Er*Cry4 W369F mutant and the *Dm*Cry W394F mutant, where W_D is replaced by redox inert phenylalanine, exhibit very similar ΔA spectra, suggesting the transient species, including the ET chain, are the same (compare Figure 3-4B and Figure 3-5B). Recent EPR and TA measurements of *Dm*Cry W394F support the assignment of W_C as the terminal electron donor.[78] Additionally, the ΔA spectra and their temporal evolution can be rationalized satisfactorily by considering exclusively flavin and Trp species. Hence, although we cannot rule out the unexpected involvement of other amino acids in the ET chain, it seems unlikely.

The temporal evolution of MFEs in *Er*Cry4 WT & *Er*Cry4 W369F

The MFE observed in *Er*Cry4 WT (see Figure 3-9C) is significantly larger than in *Dm*Cry WT (*c.f.* Figure 3-7C). The $\Delta\Delta A$(530 nm) averaged over the time window of 0.25 μs to 3 μs is $-(2.4 \pm 0.3) \times 10^{-5}$ and the $\%MFE = -(1.6 \pm 0.2)\%$.

Section 1.4 highlighted the importance of efficient competition between the spin selective BET, formation of RP2 from RP1, and spin relaxation processes. The reason for the observation of larger MFE in *Er*Cry4 WT compared to *Dm*Cry WT is most probably that faster spin selective BET from RP1 and faster deprotonation of RP1 compete more efficiently with spin decoherence. This hypothesis is supported by the evidence of a shorter lifetime of the RP1 and faster formation of RP2 in *Er*Cry4 WT compared to *Dm*Cry WT presented in Section 3.1 and earlier in this section. The negative sign of the MFE is again consistent with the assumption of a singlet-born RP1.

There is a clear difference in the temporal evolution of the ΔA and $\Delta\Delta A$ observed at 530 nm compared to that at 600 nm. This difference is also observed in *Dm*Cry (see Section 3.2.1.1) and can be analogously rationalized by considering the proposed photoreaction cycle (see Figure 3-2) in which deprotonation of RP1 ($[F^{\bullet-}\ WH^{\bullet+}]$) leads to RP2 ($[F^{\bullet-}\ W^{\bullet}]$). $W^{\bullet}$ does not absorb strongly at 600 nm while $WH^{\bullet+}$ exhibits an absorbance maximum at around 600 nm. Hence, a decrease in RP1 concentration leads to decrease in ΔA at 600 nm. At 530 nm, this decrease is partly compensated by the formation of $W^{\bullet}$ which absorbs strongly there. This effect is observed in ΔA as a steeper and "deeper" drop of ΔA(600 nm) compared to ΔA(530 nm) but also in $\Delta\Delta A$ as the magnetic sensitivity is passed from RP1 to RP2. The %MFE is approximately constant over the observed timeframe with an average value of –(1.6 ±0.2)%.

By contrast with the WT, the *Er*Cry4 W369F mutant exhibits an extraordinarily large and negative $\Delta\Delta A$ (see Figure 3-9D). The negative MFE is consistent with the suggested formation of a singlet-born SC RP. The maximum $\Delta\Delta A$ observed in *Er*Cry4 W369F is an order of magnitude larger than observed in the *Er*Cry4 WT. This remarkably large MFE and the significant difference in the magnitude of the mutant and WT cryptochrome, which is also observed between *Dm*Cry WT and *Dm*Cry W394F, will be analysed and discussed in more detail in Section 3.2.3. The remainder of this section focuses on the analysis of the temporal evolution of the $\Delta\Delta A$ observed in *Er*Cry4 W369F.

The $\Delta\Delta A$ measured at 530 nm reaches a maximum magnitude of $-(2.5 \pm 0.1) \times 10^{-4}$ after 3 μs PPD time, followed by a decay within 20 μs and a plateau at approximately -1.2×10^{-4} between 0.1 ms and 1 ms. The magnitude and temporal evolution of the $\Delta\Delta A$ at 600 nm is markedly different. It reaches maximum magnitude, $-(1.1 \pm 0.1) \times 10^{-4}$, much earlier, at 0.5 μs PPD time, and plateaus between 0.1 ms and 1 ms PPD time at a much lower level, approximately -2.4×10^{-5}.

The temporal evolution of the $\Delta\Delta A$ signal in *Er*Cry4 W369F exhibits similarities to the $\Delta\Delta A$ observed in *Dm*Cry W394F reflecting similarities in their photocycle presented in Section 3.1. In *Er*Cry4 W369F, as in *Dm*Cry W394F, the difference in the temporal evolution of the $\Delta\Delta A$(530 nm) compared to the $\Delta\Delta A$(600 nm) is attributed to the formation of $W^{\bullet}$ from $WH^{\bullet+}$ through deprotonation: Both radicals absorb at 530 nm, but only $WH^{\bullet+}$ absorbs strongly at 600 nm. This is consistent with the difference in the respective decay rate constants of ΔA(530 nm) and ΔA(600 nm) calculated in the previous section and supports the proposed deprotonation of a fraction of $WH^{\bullet+}$ on a microsecond timescale.

The %MFE at both 530 nm and 600 nm increases between 0.25 μs and 5 μs after photoexcitation, before plateauing at approximately 20% between 20 μs and 1 ms PPD time. The large %MFE reflects that in *Er*Cry4 W369F the spin–selective charge recombination competes very efficiently with spin decoherence processes. Furthermore, the long lifetime of the $\Delta\Delta A$ and the %MFE is firm evidence for the formation of a long–

lived RP2, which inherits the magnetic sensitivity of RP1 consistent with the proposed photo-cycle.

The temporal evolution of Δ*A* and MFEs in *Er*Cry4 W318F

The Δ*A* signal observed at 530 nm in *Er*Cry4 W318F, shown in Figure 3-10A, is more than an order of magnitude smaller than in *Er*Cry4 WT (*c.f.* Figure 3-9A). At 530 nm, a weak long–lived component is still observed after 1 ms, consistent with the results of Section 3.1.3, which suggest the formation of a long–lived RP in *Er*Cry4 W318F, despite the replacement of W_C with phenylalanine, albeit at low yield compared to *Er*Cry4 WT and *Er*Cry4 W369F.

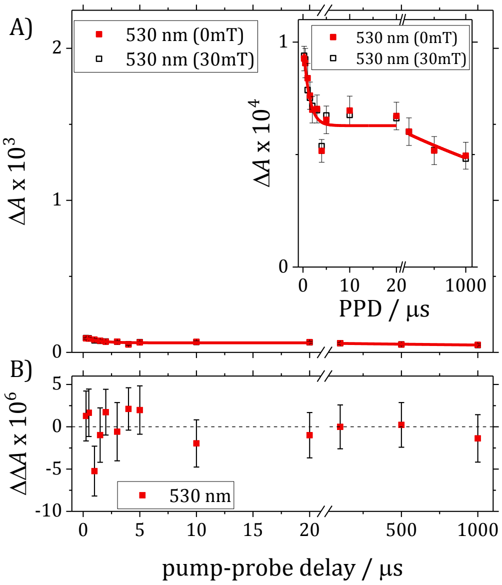

Figure 3-10: A) shows the Δ*A* of *Er*Cry4 W318F measured under standard conditions (see Table 2-1) as a function of PPD time at 530 nm. The Δ*A* was measured with an external magnetic field of *B* = 30 mT applied (open squares) and without *B* = 0 mT (solid red squares). To highlight the difference in the magnitude of the Δ*A* compared to the *Er*Cry4 WT, the scale of the y-axis is kept identical to the *y*-axis of Figure 3-9A. The inset shows the Δ*A* data on an adjusted *y*-axis scale. The solid lines represent an exponential fit to the Δ*A* (for details see text). B) shows the difference (ΔΔ*A*) of the Δ*A* measured at 0 mT and 30 mT presented in A).

No significant MFE was detected in *Er*Cry4 W318F. The average of the ΔΔ*A* between 0.5-5 μs is 0.1 ±10 $\times 10^{-7}$. But note that due to the low Δ*A* signal, only ~7.3 $\times 10^{-5}$ in the PPD time region of 0.5-5 µs, a $\%MFE$ on the order of several percent cannot be excluded due to the limited signal to noise.

3.2.2 Spectral analysis of MFEs in *Er*Cry4 W369F

The large MFEs observed in *Er*Cry4 W369F allow for a more detailed analysis of the effects of a 30 mT magnetic field on the observed ΔA. In addition to the analysis of the temporal evolution of the $\Delta\Delta A$ at two selected wavelengths, described in the previous section, it facilitates the analysis of the spectral properties of transient species whose concentration is sensitive to magnetic fields. This additional spectral information sheds more light on the identity of those species.

The ΔA signal was recorded as a function of wavelength and PPD time at both B = 0 mT and 30 mT. The ΔA(0 mT) and $\Delta\Delta A$ action spectra are shown in Figure 3-11A and B respectively. The ΔA(0 mT) spectra recorded at 0.5 µs, 5 µs, and 100 µs with B = 0 mT are shown in Figure 3-11A for comparison. For increased signal to noise, the $\Delta\Delta A$ spectra shown in Figure 3-11B represent the average of 4, 3, and 3 separately measured $\Delta\Delta A$ spectra recorded between 0.5-3 µs, 5-20 µs, and 0.1-1 ms PPD time, respectively. The solid lines in Figure 3-11A and B are the results of global target analysis using a spectral model as described in the Section 2.2 for *Er*Cry4 W369F. Note that the data presented in Figure 3-11A is an excerpt from the data set shown in Figure 3-5B.

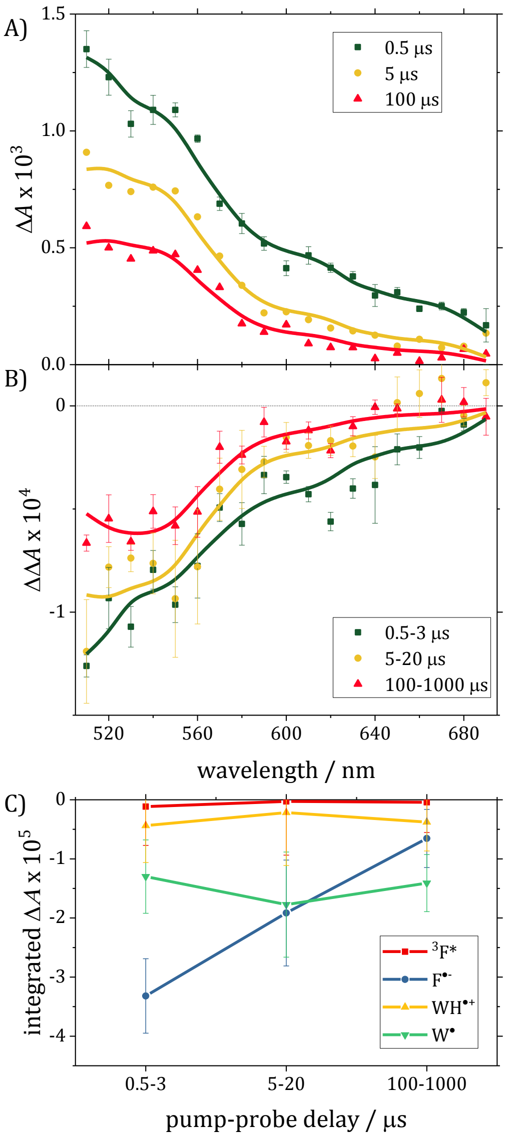

Figure 3-11: A) The ΔA spectra and B) the $\Delta\Delta A$ action spectra of *Er*Cry4 W369F recorded under standard conditions (see Table 2-1) as a function of PPD delay time. The error bars represent one standard error of the mean. The solid lines are the fitted spectra using the global analysis method as described in Section 2.2 and 3.1.1. C) The contribution coefficients (c_i) resulting from the global target analysis of the $\Delta\Delta A$ spectra shown in B). They are represented as the absorbance contributed by each species (indicated by different colours) integrated over the wavelength range of the measurement. Error bars represent the estimated standard deviation.

The striking similarity between the ΔA spectra in Figure 3-11A and the $\Delta\Delta A$ spectra in Figure 3-11B suggests that the concentrations of most transient species absorbing in the observed wavelength region are magnetically dependent. This is consistent with the global analysis of the ΔA (see Section 3.1.3), where the vast majority of the ΔA signal is assigned to $F^{\bullet -}$, $WH^{\bullet +}$, and $W^{\bullet}$.

The $\Delta\Delta A$ spectra can be explained entirely using flavin and Trp radical reference spectra. The results of the spectral target analysis are shown in Figure 3-11C. As expected, there are some differences between the results of the target analysis of the ΔA and the $\Delta\Delta A$ of *Er*Cry4 W369F, notably with respect to the $^3F^*$ contribution. A significant component of the ΔA at early PPD times (0.25 µs to 3 µs) is assigned to $^3F^*$ (see Figure 3-5E); in contrast only a negligible amount of the $\Delta\Delta A$ is attributed to $^3F^*$ at all PPD times (see Figure 3-11C). This difference is, of course, also reflected in the $\Delta\Delta A$ data recorded at 0.5 µs to 3 µs in the wavelength range 670 nm to 690 nm, where $^3F^*$ is the dominant absorber. No significant $\Delta\Delta A$ signal (see Figure 3-11B dark green symbols) is observed in this region, while the ΔA data points recorded within the same time and wavelength range show a comparatively large positive ΔA signal (see Figure 3-11A dark green symbols). This suggests that, although there is a significant concentration of $^3F^*$ present at early PPD times, the $^3F^*$ concentration is not significantly affected by the application of an external B field. The dominant species contributing to the overall $\Delta\Delta A$ signal are $F^{\bullet -}$ and $W^{\bullet}$, consistent with the suggested RP mechanism as the origin of the observed MFE and the results from previous sections regarding the identity and the lifetime of the RP2.

3.2.3 Magnetically altered reaction yield spectra

In this section, the magnetically altered reaction yield (MARY) as a function of the intensity of an external magnetic field B is investigated at selected PPD times. For this purpose the change in the differential absorbance ΔA, upon application of a magnetic field ranging from 0 mT to 30 mT is measured as both an absolute change ($\Delta\Delta A = \Delta A(B) - \Delta A(B=0)$) and percentage change ($\%MFE = \Delta\Delta A/\Delta A(B=0)$) in ΔA.

3.2.3.1 Comparison between ErCry4 and DmCry MARY spectra

Figure 3-12A shows the $\%MFE$ of *Er*Cry4 WT and *Dm*Cry WT recorded at 530 nm and 2 µs PPD as a function of B between 0 mT and 30 mT. Fewer B-field measurements were made for the MARY spectrum of *Dm*Cry, in order to increase the signal to noise ratio.

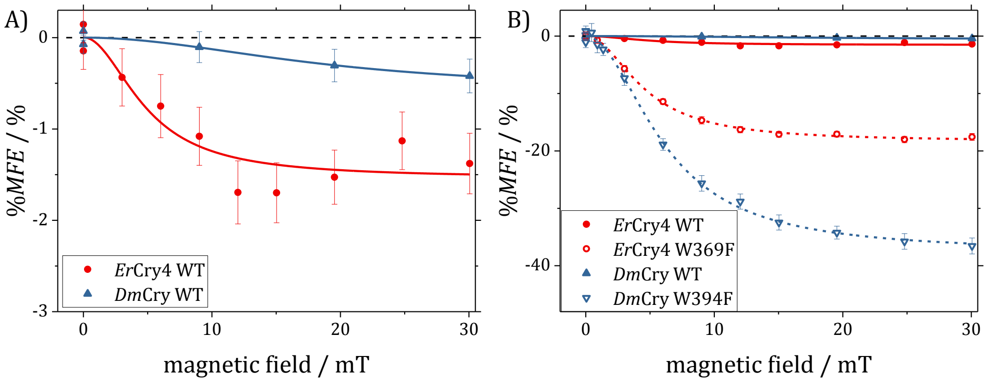

Figure 3-12: MARY spectra for A) *Er*Cry4 WT (red) and *Dm*Cry WT (blue) and B) *Er*Cry4 WT (red solid circles), *Er*Cry4 W369F (red open circles), *Dm*Cry WT (blue solid triangles), and *Dm*Cry W394F (blue open triangles) measured under standard conditions (see Table 2-1) at 530 nm and 2 µs PPD time. The error bars represent one SEM and the lines Lorentzian fits to the %*MFE* data. Results of the fitting are summarized in Table 3-3.

The negative sign of the MFE observed in both *Er*Cry4 WT and *Dm*Cry WT is consistent with previous sections and the assumption of the formation of a singlet-born SC RP. Both MARY spectra can be fit satisfactorily by a Lorentzian function, represented as solid lines, from which $\%MFE_{sat}$ and $B_{1/2}$ values were extracted (see Table 3-3).

Table 3-3: Summary of the $B_{1/2}$ values extracted from Lorentzian fits to the MARY spectra shown in Figure 3-12. Uncertainties represent one standard deviation.

		$\%MFE_{sat}$ / %	**$B_{1/2}$ / mT**
***Er*Cry4**	WT	−1.5 ±0.2	4.9 ±1.6
	W369F	−18.4 ±0.2	4.6 ±0.1
***Dm*Cry**	WT	−0.59 ±0.44	(19 ±18)
	W394F	−37.6 ±0.6	6.1 ±0.2

The MARY spectra for *Er*Cry4 WT and *Dm*Cry WT are significantly different both in the magnitude of the $\%MFE_{sat}$ and width. In *Er*Cry4 WT the %*MFE* has essentially reached its saturation value of $\%MFE_{sat} = -(1.5 \pm 0.2)\%$ at 30 mT ($\%MFE(30\text{mT}) = -(1.4 \pm 0.3)\%$). The %*MFE* at 30 mT and the $\%MFE_{sat}$ in *Dm*Cry WT are significantly smaller than in *Er*Cry4 WT ($\%MFE(30\text{mT}) = -(0.42 \pm 0.19)\%$ and $\%MFE_{sat} = -(0.59 \pm 0.44)\%$). This finding is in good agreement with the results presented in the Section 3.2.1.

The $B_{1/2}$ of *Er*Cry4 WT is estimated to be 4.9 ±1.6 mT, close to the Weller estimate of the $B_{1/2}$ of flavin-Trp RPs of 3 mT. The Weller formula (Equation 2.24) allows the calculation of expected $B_{1/2}$ values, considering the hyperfine coupling and the energy splitting of the triplet spin states by the Zeeman effect. The $B_{1/2}$ values of flavin-Trp RPs have often been found experimentally to exceed the Weller value significantly.[15, 76] The discrepancy between the experimental observation and the Weller estimate of $B_{1/2}$ is likely to be due to the effects of spin relaxation, which are not considered in the Weller formula.

Figure 3-12B shows the MARY spectra of the two WT proteins (bold lines) and the W_D deficient mutants (dashed lines). The difference in the magnitudes of the $\%MFE$ between the WT and mutant Cry is clear and consistent with the results presented in Section 3.2.1. This is further evidence that the fourth Trp (W_D) plays a decisive role in the photochemistry of *Dm*Cry WT and *Er*Cry4 WT and is the most likely flavin-Trp RP partner in RP1 and RP2.

There are two likely and related effects, which can rationalize the difference in behaviour between the Crys with intact Trp-tetrad and the mutants with the shortened Trp ET chain. In Section 1.4 it was established that, in addition to magnetically sensitive spin mixing and spin selective BET, an effective competition between the spin selective BET and the spin decoherence processes are prerequisites for the manifestation of an MFE via the RP mechanism. Additionally, the formation of RP2 needs to compete efficiently with the BET and spin-decoherence processes in order to inherit the MFE from RP1 and form a relatively stable species whose concentration is dependent on magnetic fields.

According to the results presented in Section 3.1 and 3.2 the rate of RP2 formation is significantly increased, and RP1 lifetime decreased, in the W_D mutants compared to the respective WT. This observation offers a plausible explanation for the significantly increased MFE observed in the W_D mutants compared to the WT: The shorter lifetime of RP1 and the faster formation of RP2 likely leads to more effective competition between spin selective BET, RP2 formation, and spin relaxation processes, which in turn leads to larger MFEs.

A shortening of the Trp ET chain may also lead to an increase in the spin coherence time facilitating more effective competition between spin–selective BET, spin-decoherence, and RP2 formation. The modulation of the exchange interaction between the unpaired electrons of the SC RP by fast electron hopping between W_D and W_C has been proposed as a likely mechanism for the spin-decoherence observed in *At*Cry1 and *E. coli* PL.[15] The involvement of the W_D in both *Er*Cry4 WT and *Dm*Cry WT has been demonstrated convincingly in previous sections. The replacement of the W_D with phenylalanine prevents electron hopping between W_D and W_C, not only altering the kinetics of the chemical transformation as outlined in the previous sections, but also having a decisive effect on the spin relaxation time.

3.2.3.2 Time dependence of MARY spectra observed in cryptochromes

The exceptionally large MFEs observed in both *Er*Cry4 W369F and *Dm*Cry W394F allow for a detailed analysis of the temporal evolution of the MARY of transient species and any temporal evolution of $B_{1/2}$. The MARY spectra for *Er*Cry4 W369F and *Dm*Cry W394F, recorded at various PPD times as indicated by the different colours, are shown in Figure 3-13. In Figure 3-13A and B the MFE is presented as $\Delta\Delta A$ spectra while C and D show the results of the same MFE measurements as $\%MFE$.

The temporal evolution of the magnitude of $\Delta\Delta A$ or $\%MFE$ measured at 30 mT shows the expected trends: In *Er*Cry4 W369F $\Delta\Delta A$ increases from 0.5 µs to 2 µs and then decreases between 2 µs and 100 µs. In *Dm*Cry W394F, the $\Delta\Delta A$ decreases from 0.5 µs onwards. In *Er*Cry4 W369F, the $\%MFE$ increases between 0.5 µs to 2 µs then approximately plateaus. The $\%MFE$ in *Dm*Cry W394F increases from 0.5 µs to 2 µs followed by a constant decrease. These trends are consistent with the results of Section 3.2.1. Note that some features, such as the increase in $\Delta\Delta A$ between 0.5 µs to 2 µs in *Dm*Cry W394F are visible in the data presented in Section 3.2.1, but are not reflected in this data set due to the limited time resolution. For a detailed analysis of the temporal evolution of the $\Delta\Delta A$ and the $\%MFE$ see Section 3.2.1.

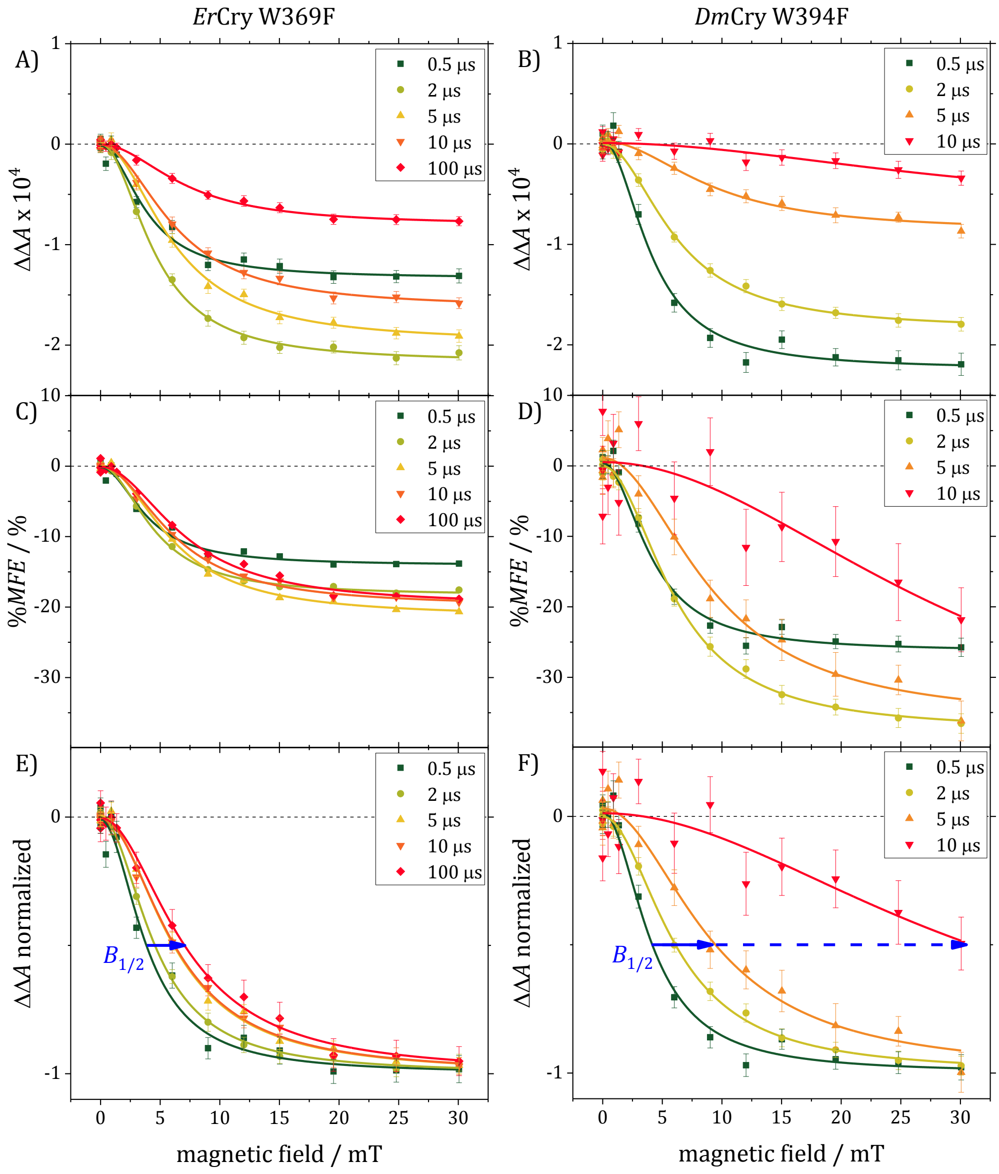

Figure 3-13: MARY spectra for *Er*Cry4 W369F and *Dm*Cry W394F measured under standard conditions (see Table 2-1) at 530 nm and a series of PPD times as indicated by different colours. The error bars represent one SEM and the lines Lorentzian fits of the MFE data. Results of the fitting are summarized in Table 3-4 and illustrated in Figure 3-14. The MARY spectra are represented as $\Delta\Delta A$ spectra in A) and B), as %MFE spectra in C) and D), and as $\Delta\Delta A$ spectra normalized to the saturation value of $\Delta\Delta A$ in E) and F). Note that the MARY spectra shown in A), C), and E) for *Er*Cry4 and B), D, and F) for *Dm*Cry represent the results of the same measurement. The blue arrow in E) and F) highlights the increase in $B_{1/2}$ with PPD time.

The temporal evolution of the width of the MARY spectra is quantified by fitting each of the MARY spectra with a Lorentzian function to estimate $B_{1/2}$. The width of the MARY spectrum and the $B_{1/2}$ value are independent of the magnitude of the MFE (*i.e.* the $B_{1/2}$ value is the same for $\Delta\Delta A$, $\%MFE$, and the normalized $\Delta\Delta A$) and the temporal evolution of the width, *i.e.* the temporal evolution of $B_{1/2}$, is best illustrated in the $\Delta\Delta A$ spectra normalized to their respective saturation values, as shown in Figure 3-13E and F. It is clear from Figure 3-13E and F that the width of the MARY spectra, reflected in the $B_{1/2}$ values, increases with increasing PPD time. The $B_{1/2}$ for *Er*Cry4 W369F and *Dm*Cry W394F are shown as a function of PPD time in Figure 3-14 and summarized in Table 3-4.

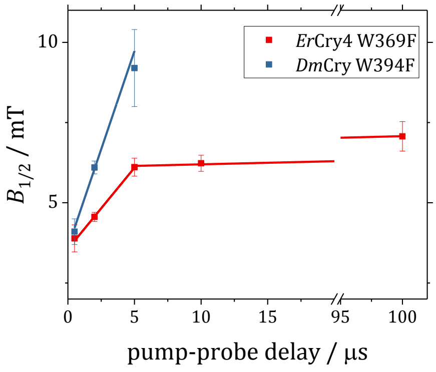

Figure 3-14: Illustration of the $B_{1/2}$ values extracted from Lorentzian fits to the MARY spectra shown in Figure 3-13 as a function of PPD time for *Er*Cry4 W369F (red) and *Dm*Cry W394F (blue).The error bars represent one standard deviation. The solid lines are shown to guide the eye.

Table 3-4: Summary of the $B_{1/2}$ values extracted from Lorentzian fits to the MARY spectra shown in Figure 3-13. Uncertainties represent one standard deviation.

PPD time / µs	**$B_{1/2}$ / mT**	
	***Er*Cry4 W369F**	***Dm*Cry W394F**
0.5	3.89 ±0.42	4.1 ±0.4
2	4.56 ±0.14	6.1 ±0.2
5	6.11 ±0.28	9.2 ±1.2
10	6.23 ±0.25	(31 ±26)
100	7.07 ±0.46	-

For *Er*Cry4 W369F, large $\Delta\Delta A$ and ΔA values can be obtained between 0.5 µs and 100 µs PPD time (see Figure 3-9B). Thus the $\Delta\Delta A$, %MFE, and $B_{1/2}$ values can be determined with satisfactorily high precision in that time interval. In contrast, reflecting the diminishing ΔA signal, the uncertainties of the %MFE data of *Dm*Cry W394F measured at 10 µs PPD time are unsatisfactorily large (see Figure 3-7B) and is not considered in the following analysis. For *Dm*Cry W394F, no MARY spectrum was recorded for 100 µs PPD time since even lower $\Delta\Delta A$ and ΔA values and larger uncertainties on the %MFE values are to be expected (see Figure 3-7B and D).

In both *Er*Cry4 W369F and *Dm*Cry W394F, a significant increase in the $B_{1/2}$ values with increasing PPD time is observed (see Figure 3-13E, F and Figure 3-14). An increase in $B_{1/2}$ with PPD on this timescale is unexpected since previous studies attribute the increased width of MARY spectra of flavin-Trp SC RP in proteins to the effects of spin relaxation destroying spin coherence.[15, 76] In order to explain the increase in $B_{1/2}$ beyond 2 µs in this way, the spin coherence time of the magnetically sensitive SC RP would have to be extraordinarily long, exceeding 2 µs. The increase in $B_{1/2}$ between 2 µs and 5 µs consequently suggests that either the spin coherence lifetime is indeed exceptionally long in the *Er*Cry4 and *Dm*Cry mutants or, that the width of the MARY spectra is affected by another mechanism instead.

The replacement of the W_D with phenylalanine has the potential to increase the spin coherence time by inhibiting decoherence processes driven by the modulation of the exchange interaction through electron hopping between the Trp of the ET chain, which could in fact rationalize the long spin-coherence lifetime.

The phenomenon can also be rationalized by MFEs on the S-T population difference of SC RP, where the spin correlation is induced through spin–selective charge recombination from the S-state. Since BET is forbidden from the T-state but allowed from the S-state, the relative T-state population increases from thermal equilibrium values in cases where spin selective BET is significantly faster than S-T interconversion. In this way, S-T interconversion can become the rate determining step for the charge recombination. The efficiency of S-T interconversion depends on the magnitude of the energy gap induced by magnetic fields through the Zeeman interaction. Consequently, the lifetime of the SC RP and the concentration of downstream photoproducts depend on the intensity of the applied magnetic field. This mechanism, acting in addition to the processes described previously may be the origin of the change in the MARY spectra with PPD times exceeding the spin-coherence lifetime. Since BET has to be faster than the S-T interconversion, this mechanism is expected to be effective only on RP1. This is consistent with the temporal evolution of $B_{1/2}$ and the lifetime of RP1.

3.3 Contrasting the photochemistry of avian, insect and plant cryptochrome

In this section the photochemistry of *Arabidopsis thaliana* (*At*) cryptochrome *At*Cry1 WT is investigated and compared with the findings on *Dm*Cry WT and *Er*Cry4 WT. A detailed analysis of the photochemistry and the effects of a magnetic field on the concentration of the transient species of *Dm*Cry WT and *Er*Cry4 WT can be found in Sections 3.1 and 3.2. *At*Cry1 WT is, like *Dm*Cry WT, a well-studied flavoprotein. It is proposed to exhibit a photo-induced reaction cycle different from *Dm*Cry WT and *Er*Cry4 WT (see Figure 3-15).[15, 58-59, 91-92]

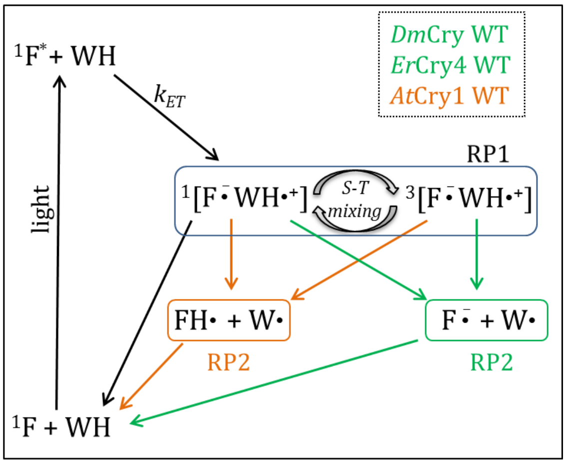

Figure 3-15: Photochemical reaction scheme appropriate for *Dm*Cry WT (green), *Er*Cry4 WT (green), and *At*Cry1 WT (orange). The singlet excited state ($^1F^*$) is formed upon light excitation of the FAD ground state (^1F). The $^1F^*$ is subsequently reduced by a nearby Trp to form a radical pair (RP1) conserving the spin state of its precursor $^1[F^{\bullet-} WH^{\bullet+}]$. The RP1 undergoes coherent singlet-triplet mixing driven by hyperfine interactions as indicated by the curly arrows. The data presented in this work suggest that the RP1 changes its protonation state to form RP2 comprised of $F^{\bullet-}$ and $W^\bullet$ in DmCry WT and ErCry4 WT, as indicated by the green reaction pathway and $FH^\bullet$ and $W^\bullet$ in *At*Cry1 WT as indicated by the orange reaction pathway.

Upon blue-light excitation of the flavin cofactor, an electron is transferred from a nearby Trp (W_A) to reduce the excited flavin ($^1F^*$) to form a SC RP (RP1) comprised of $F^{\bullet-}$ and $WH^{\bullet+}$, which interconverts coherently between the S and T-state. This RP1 can react via competing pathways: charge recombination or change in protonation state to form RP2.

The protonation state of RP2 observed on a microsecond timescale in *At*Cry1 WT differs from the RP2 observed in *Dm*Cry WT and *Er*Cry4 WT. In *At*Cry1 WT the formation of the neutral $FH^{\bullet}$ is observed.[15, 58] In contrast no evidence for the protonation of $F^{\bullet-}$ is observed in *Dm*Cry WT and *Er*Cry4 WT on a microsecond timescale, and the detected RP2 in *Dm*Cry WT and *Er*Cry4 WT is comprised of $F^{\bullet-}$ and $W^{\bullet}$ instead. The sensitivity of the coherent S-T interconversion, indicated as curly arrows in Figure 3-15, can lead to magnetically altered lifetimes of the SC RP and reaction yields of downstream photoproducts.[15, 59] See Section 1.3 and 1.4 for more details on the manifestation of MFE in SC RP.

3.3.1 Time dependence of Δ*A* and MFEs

Figure 3-16 shows the Δ*A* spectra of *At*Cry1 WT recorded at a series of PPD times. The Δ*A* signal decays rapidly between 0.5 μs and 5 μs, however between 8 μs and 13 μs the spectral shape and the magnitude of the Δ*A* does not change significantly. The Δ*A* spectra recorded at late PPD times (after 5 μs) are distinctly different from the spectra observed in *Er*Cry4 WT and *Dm*Cry WT, for which $F^{\bullet-}$ and $W^{\bullet}$ were the predominant absorbing species (see Figure 3-4 and Figure 3-5). The overall shape of the Δ*A* spectra observed in *At*Cry1 WT (see Figure 3-16) is consistent with the proposed formation of a RP comprised of $FH^{\bullet}$ and $W^{\bullet}$, and is similar to the results of previous TA studies on *At*Cry1 WT and other plant cryptochromes.[15, 57, 93] This is consistent with the evidence that in *At*Cry1 WT the anionic flavin radical ($F^{\bullet-}$) is protonated on a microsecond timescale to form a longer lived RP2 analogous to *Er*Cry4 WT and *Dm*Cry WT.[15] Note however, that in *Er*Cry4 WT and *Dm*Cry WT protonation of $F^{\bullet-}$ on a microsecond timescale is not observed, and RP2 is comprised of $F^{\bullet-}$ and $W^{\bullet}$ instead.

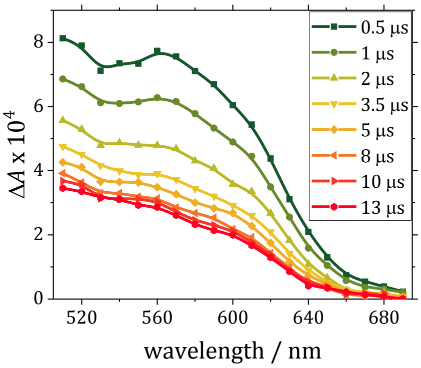

Figure 3-16: Differential absorbance (ΔA) spectra of *At*Cry1 WT recorded under standard conditions (Table 2-1) and a series of PPD delay times as indicated by the different colours of the symbols. The solid lines are spline fits to guide the eye.

Figure 3-17 shows the time dependence of the ΔA measured at 530 nm in *Er*Cry4 WT (red), *Dm*Cry WT (blue), and *At*Cry1 WT (yellow). The characteristic biphasic decay of ΔA is observed in all three cryptochromes. The faster decay component (microsecond lifetime) can be largely attributed to processes associated with the changes in RP1 concentration, including the BET and the change in protonation state to form RP2. The second decay component, which is orders of magnitude slower (millisecond lifetime), is associated with the lifetime of RP2. More details on the assignment of the two phases of the ΔA decay traces can be found in Section 3.2.1.

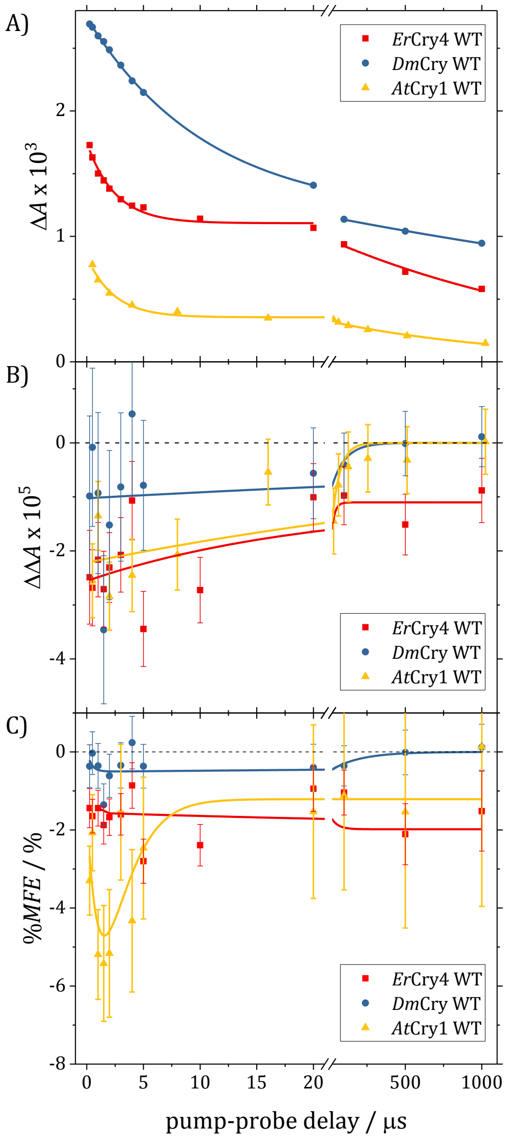

Figure 3-17: A) The ΔA, B) the $\Delta\Delta A$, and C) the $\%MFE$ of *Er*Cry4 WT (red), *Dm*Cry WT (blue), and *At*Cry1 WT (yellow) measured under standard conditions (Table 2-1) at 530 nm as a function of PPD time. Error bars represent one standard error of the mean. Solid lines in A) are biphasic exponential fits, see text for details. Fit parameters are summarized in Table 3-5. Solid lines in B) and C) are shown to guide the eye.

The temporal evolution of the ΔA measured at 530 nm, shown in Figure 3-17 for *Er*Cry4 WT, *Dm*Cry WT, and *At*Cry1 WT, was analysed by separately fitting the ΔA data recorded between 0.25 μs and 20 μs and between 30 μs and 1 ms, using single exponential decay functions of the form

$$f_1 = A_1 e^{-t/\tau_1} + c \tag{3.3}$$

and

$$f_2 = A_2 e^{-t/\tau_2} \tag{3.4}$$

for the two phases of the decay traces, respectively. This method is similar to the data analysis described in more detail in Section 3.2.1. The results are summarized in Table 3-5.

Table 3-5: Results of the kinetic analysis of the ΔA(530 nm) time traces of *Er*Cry4 WT, *Dm*Cry WT, and *At*Cry1 WT, shown in Figure 3-17 using Equations 3.1 and 3.2 as fit functions with k_i.= $1/\tau_i$. The uncertainties represent one standard deviation.

	***Er*Cry4 WT**	***Dm*Cry WT**	***At*Cry1 WT**
A_1 **×10⁵**	64 ±3	158 ±2	48 ±4
k_1 **/μs⁻¹**	0.40 ±0.04	0.094 ±0.004	0.42 ±0.07
τ_1 **/μs**	2.5 ±0.3	10.1 ±0.4	2.3 ±0.4
A_2 **×10⁵**	98 ±4	116 ±1	32.4 ±0.7
k_2 **/s¹**	543 ±73	204 ±8	807 ±50
τ_2 **/ ms**	1.8 ±0.2	4.9 ±0.2	1.23 ±0.08

The ΔA signal of *Dm*Cry WT recorded at 0.5 μs PPD time is ~2 times larger than that of *Er*Cry4 WT and ~3 times larger than that of *At*Cry1 WT. The larger ΔA signal can be rationalized by the significantly slower decay of the ΔA(530 nm) in *Dm*Cry WT (τ_1(*Dm*Cry)= 10.1 ±0.4 μs), *i.e.* a longer lifetime of RP1, than in *Er*Cry4 WT and *At*Cry1 WT and likely also an overall higher quantum yield of RP1 in *Dm*Cry WT. The similarity of τ_1 observed in *At*Cry1 WT (τ_1(*At*Cry1)= 2.3 ±0.4 μs) and *Er*Cry4 WT (τ_1(*Er*Cry4)= 2.5 ±0.3 μs) suggests that the difference in ΔA(0.5 μs) between *Er*Cry4 WT and *At*Cry1 WT is likely due to a difference in the quantum yield of RP1 rather than a difference in the RP1 lifetime.

After 100 µs PPD time the Δ*A* signal in *Dm*Cry WT and *Er*Cry4 WT are of similar magnitude but significantly larger than in *At*Cry1 WT. This is reflected in the fit parameter A_2 (see Table 3-5) and suggests a comparable quantum yield of RP2 in *Dm*Cry WT and *Er*Cry4 WT but a much lower quantum yield of RP2 in *At*Cry1 WT. In both *Er*Cry4 WT and *At*Cry1 WT the lifetime of the second decay component (τ_2(*Er*Cry4)= 1.8 ±0.2 ms and τ_2(*At*Cry1)= 1.23 ±0.08 ms) is significantly smaller than in *Dm*Cry WT (τ_2(*Dm*Cry)= 4.9 ±0.2ms), suggesting a longer lifetime of the RP2 in *Dm*Cry WT than in *Er*Cry4 WT and *At*Cry1 WT.

The ΔΔ*A* and %*MFE* are shown in Figure 3-17B and C respectively for *Er*Cry4 WT (red), *Dm*Cry WT (blue), and *At*Cry1 WT (yellow). The ΔΔ*A* in *At*Cry1 WT and *Er*Cry4 WT is of comparable magnitude ($\sim 2.5 \times 10^{-5}$) and about half the size in *Dm*Cry WT ($\sim 1 \times 10^{-5}$) at early PPD times (see Figure 3-17B). In Section 3.2.1 the relatively small MFE observed in *Dm*Cry WT was rationalized by the hypothesis that the slow spin selective BET and deprotonation of RP1 (reflected in a long RP1 lifetime) led to the small MFEs, since BET and deprotonation of RP1 do not compete efficiently with processes leading to spin relaxation. The ΔΔ*A* observed in *At*Cry1 WT is similar in magnitude compared to the ΔΔ*A* observed in *Er*Cry4 WT while also showing a decay time τ_1 similar to that found in *Er*Cry4 WT. In contrast τ_1 found in *Dm*Cry WT is significantly larger than τ_1 in *At*Cry1 WT and *Er*Cry4 WT. This supports the aforementioned hypothesis that in *Dm*Cry WT the spin selective BET and change in protonation state might not be sufficiently fast for the manifestation of large MFEs on the concentration of the SC RP and downstream photoproducts.

The evidence presented in this chapter strongly suggests that in all three cryptochromes a relatively stable flavin-Trp radical (RP2) is formed, with a lifetime of more than 1 ms and exceeding the timeframe observed in this work. Furthermore, the sensitivity of the concentration of RP2 towards magnetic fields could be demonstrated. The formation of long-lived transient species with magnetic-field-dependent concentrations can be thought of as an ideal precondition for a biological magneto compass based on the RP mechanism. The MFEs presented in this work reflect the differences in concentration of transient species formed through photoexcitation of Crys *in vitro* using nanosecond laser pulses as the excitation source. The transient species undergo chemical transformations (see Figure 3-15) following excitation, and the sensitivity of S-T interconversion towards magnetic fields leads to MFEs on the concentrations of transient species. In this work the changes in concentration are detected at certain time intervals after the excitation (*i.e.* PPD times). In contrast, the excitation of the FAD cofactor of Crys *in vivo* is likely to take place under continuous illumination conditions by a natural light source such as the sun. The relative concentrations of individual transient species will then depend strongly on their respective life times: very short-lived species react quickly and do not accumulate, while more stable and long-lived species of the reaction cycle can reach comparatively high concentrations. A sufficiently long lifetime of a transient species might therefore be crucial in order to reach the threshold concentration necessary to act as the signalling state or the precursor to the signalling state.

3.3.2 Magnetically altered reaction yield spectra

The MARY as a function of magnetic field is shown for *Er*Cry4 WT, *Dm*Cry WT, and *At*Cry1 WT in Figure 3-18. The purpose of this section is the direct comparison between the MARY of the two animal cryptochromes *Er*Cry4 and *Dm*Cry, discussed in detail in Section 3.2.3, and the MARY spectrum of the plant cryptochrome *At*Cry1 WT, which has been investigated previously in detail in this group.[15]

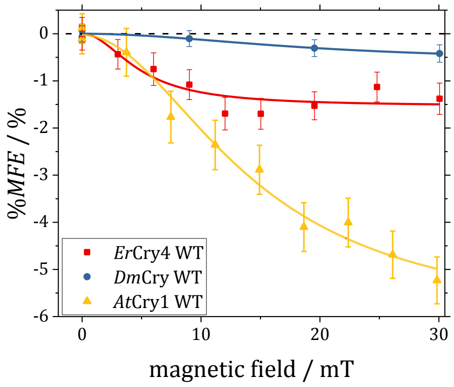

Figure 3-18: MARY spectra or *Er*Cry4 WT (red), *Dm*Cry WT (blue), and *At*Cry1 WT (yellow) measured under standard conditions (see Table 2-1) at 530 nm and 2 µs PPD time. The error bars represent one SEM and the lines Lorentzian fits. Results of the fitting are summarized in Table 3-6.

$B_{1/2}$ values were determined by fitting the %*MFE* with a Lorentzian function and the results are summarized in Table 3-6. The $B_{1/2}$ value for *Dm*Cry WT is included in the table for completeness but not considered in the further analysis due to its large uncertainty.

Table 3-6: Summary of the $B_{1/2}$ values extracted from Lorentzian fits to the MARY spectra shown in Figure 3-18. Uncertainties represent one standard deviation.

	%MFE_{sat} / %	**$B_{1/2}$ / mT**
***Er*Cry4 WT**	−1.5 ±0.2	4.9 ±1.6
***Dm*Cry WT**	−0.59 ±0.44	(19 ±18)
***At*Cry1 WT**	−6.1 ±0.4	14.3 ±1.7

The $B_{1/2}$ of *At*Cry1 WT (14.3 ±1.7 mT) is consistent with the literature value of *At*Cry1 WT (10-12 mT) measured under similar conditions (270 K, 60% glycerol (v/v)) using conventional single pass TA and significantly larger than the estimated $B_{1/2}$ of a flavin-Trp RP using the Weller equation (see Section 2.3).[15] The broadening of the MARY spectrum is attributed to the effects of fast spin relaxation induced by the electron hopping along the Trp ET chain. The significantly smaller $B_{1/2}$ value measured for *Er*Cry4 WT indicates that spin relaxation is less efficient in *Er*Cry4 WT than in *At*Cry1 WT. This is consistent with the hypothesis that electron hopping along the Trp ET chain is the cause of the increased $B_{1/2}$ value in *At*Cry1 WT, since the Trp ET chain in *Er*Cry4 WT differs substantially from that in *At*Cry1 WT. An obvious difference is that the Trp ET chain in *At*Cry1 WT is comprised of 3 Trp, while it is a Trp tetrad in *Er*Cry4 WT (see Figure 2-6).

3.4 Conclusions

MFEs on the lifetimes and concentrations of transient species form the basis of the RP mechanism, which is thought to lie at the heart of the magnetic sense of migratory birds, such as the European robin (*Erithacus rubecula*, *Er*), or of fruit flies (*Drosophila melanogaster*, *Dm*). In this chapter pronounced effects of magnetic fields on the photochemistry of *Er*Cry4, *Dm*Cry, and, for comparison, a plant cryptochrome *At*Cry1 are demonstrated. While MFEs in plant and insect cryptochromes have previously been published, the MFEs presented here on *Er*Cry4 constitute the first evidence for MFEs on the reactivity of a vertebrate cryptochrome. This finding lends further support to the hypothesis that cryptochromes and the RP mechanism play a role in the magnetically sensitive biochemical process of magnetoreception in animals, especially migratory birds.

The results presented in this thesis on *Dm*Cry WT are in good agreement with the photocycle proposed for *Dm*Cry WT in the literature.[58-59] After rapid ($k_{\mathrm{ET}} \gg 1\ \mu\mathrm{s}^{-1}$) formation of RP1 ($[\mathrm{F}^{\bullet-}\ \mathrm{WH}^{\bullet+}]$), the RP2 comprised of $\mathrm{F}^{\bullet-}$ and $\mathrm{W}^{\bullet}$ is formed on a microsecond timescale. The lifetime of RP1 is orders of magnitudes shorter than that of RP2 (τ(RP1) ≈ 10 μs and τ(RP2) ≈ 5 ms). In *Dm*Cry W369F, the $\mathrm{W_D}$-deficient mutant, RP1 and RP2 are also comprised of $[\mathrm{F}^{\bullet-}\ \mathrm{WH}^{\bullet+}]$ and $[\mathrm{F}^{\bullet-}\ \mathrm{W}^{\bullet}]$, respectively, as in *Dm*Cry WT, but both RP1 and RP2 exhibit much shorter lifetimes in *Dm*Cry W369F (*i.e.* ~1 μs and ~10 μs, respectively). This is consistent with the expected effect of shortening the Trp ET chain by replacing the distal Trp of the ET chain $\mathrm{W_D}$ (W394) with phenylalanine.

The shape of the ΔA spectra observed in *Er*Cry4 WT and *Er*Cry4 W369F are similar to that of *Dm*Cry WT and *Dm*Cry W394F, respectively and consistent with the proposed photocycle for *Dm*Cry WT. The lifetimes of RP1 ($[\mathrm{F}^{\bullet-}\ \mathrm{WH}^{\bullet+}]$) and RP2 ($[\mathrm{F}^{\bullet-}\ \mathrm{W}^{\bullet}]$) in *Er*Cry4 WT ($\tau$(RP1) ≈ 2 μs, τ(RP2) ≈ 2 ms) are shorter, but the same order of magnitude as the lifetimes of RP1 and RP2 in *Dm*Cry WT, respectively. As in *Dm*Cry, the formation of RP2 in *Er*Cry4 is much faster in the $\mathrm{W_D}$-deficient mutant than in the WT Crys. In contrast to *Dm*Cry W369F (the $\mathrm{W_D}$ deficient *Dm*Cry mutant) *Er*Cry4 W369F forms a long-lived RP2 ($\tau \gg 1$ ms) whose concentration is sensitive to magnetic fields.

These observations demonstrate the decisive role of W_D in the photochemistry of both *Dm*Cry WT and *Er*Cry4 WT and lend support to the hypothesis that the radical in *Dm*Cry WT and *Er*Cry4 WT is mostly localized on W_D.

In the Cry mutants, where the ET chain is interrupted by replacing the third Trp (W_C) by phenylalanine (*i.e. Dm*Cry W342F and *Er*Cry4 W318F), the observed ΔA is more than an order of magnitude smaller than in the WT Crys. A long-lived spectral component present in the ΔA spectra is attributed to the formation of a relatively stable RP2 comprised of $F^{\bullet -}$ and $W^{\bullet}$. This suggests that the formation of a stable RP is still feasible when the Trp ET chain is interrupted, albeit at yield reduced by 2 orders of magnitude.

A negative MFE on the concentration of the transient species is observed in both *Dm*Cry WT and *Er*Cry4 WT, consistent with the proposed formation of the SC RP in the S-state and TA experiments previously performed in this group on *Dm*Cry WT.[59] The %*MFE* observed in this work is significantly larger in *Er*Cry4 WT than in *Dm*Cry WT. More efficient competition between the spin selective BET, deprotonation of RP1 to form RP2, and spin relaxation are likely the origin of the larger absolute and fractional MFEs observed in *Er*Cry4 WT.

Both *Er*Cry4 W369F and *Dm*Cry W394F exhibit negative MFEs more than an order of magnitude larger than their respective WT counterparts. The large MFEs in those mutants can be rationalized by a more effective competition between spin selective BET, deprotonation of RP1 to form RP2, and spin relaxation. This hypothesis is supported by the observation of faster RP2 formation in both mutants compared to the WT Crys. A decrease in the rate of spin relaxation as a result of shortening the ET chain might also play an important role, as it inhibits fast spin relaxation induced by the electron hopping between W_D and W_C, which has been suggested to drive spin relaxation in *At*Cry1 WT.[15]

Spectral analysis of the MFE observed in *Er*Cry4 W369F provides further evidence that the flavin-Trp RP is the magnetically sensitive species observed in the MFE measurements, while $^3F^*$, despite absorbing strongly in the observed wavelength region, does not show any measurable sensitivity toward magnetic fields.

The photocycle of *At*Cry1 WT is similar to the photocycle proposed for *Dm*Cry WT and *Er*Cry4 WT. In *At*Cry1 WT, however, the initially formed RP [$F^{\bullet -}$ $WH^{\bullet +}$] is protonated on a microsecond timescale and hence the observed RP2 is comprised of $FH^{\bullet}$ and $W^{\bullet}$. The lifetime of RP1 is similar in *At*Cry1 WT and *Er*Cry4 WT but significantly longer in *Dm*Cry WT. At the same time, the $\Delta\Delta A$ is similar in magnitude in *At*Cry1 WT and *Er*Cry4 WT, but much smaller in *Dm*Cry WT. This supports the hypothesis, that in *Dm*Cry WT spin selective BET and RP2 formation is not competing efficiently with spin relaxation processes.

MARY as a function of magnetic field was investigated in order to shed light on the underlying spin dynamics that give rise to MFEs. The $B_{1/2}$ value for *At*Cry1 WT (14 ±2 mT) is consistent with its previously determined $B_{1/2}$ value and is much larger than expected, solely based on the hyperfine interactions involved in a flavin-Trp RP, which is ~3 mT.[15] The much larger $B_{1/2}$ value is attributed to fast spin relaxation induced by modulation of the exchange interaction through fast electron hopping within the Trp ET chain.

In *Er*Cry4 W369F and *Dm*Cry W394F an increase in the $B_{1/2}$ values between 0.5 µs and 5 µs is observed. This observation suggests that either the spin-coherence lifetime is longer than expected (>1 µs), or a magnetic field dependent process besides the hyperfine mechanism has an effect on the concentration of transient species. An alternative mechanism to rationalize this phenomenon is based on a SC RP, where spin correlation is realized through spin selective charge recombination from the S-state. In this SC RP, the rate of BET would also be sensitive to magnetic fields, if the spin-flip transition between T_0 and $T_{+/-}$ is the rate determining step.

Chapter 4.

The photochemistry of a *novel* artificial protein magnetosensor

In this chapter the first study of magnetic field effects in an artificial protein is presented. These so-called maquettes have been designed and synthesised by Dutton *et al.* to enable us to investigate the properties of protein-embedded cofactors, independent of the inherent complexities introduced by the natural protein surrounding. The maquettes are specifically designed to model the photochemistry of Crys, exhibiting both a flavin chromophore, riboflavin (RF), and selected redox active amino acids (Trp or His), while bearing minimal structural similarity (see Figure 4-1).[r]

The results presented in this chapter have been published[42, 94] and, analogous to Cry, RP formation upon light excitation is observed in the maquettes.

---

[r] More details on the structure of the maquettes and an introduction to the bottom-up approach using de novo designed maquette model systems can be found in Section 2.4.

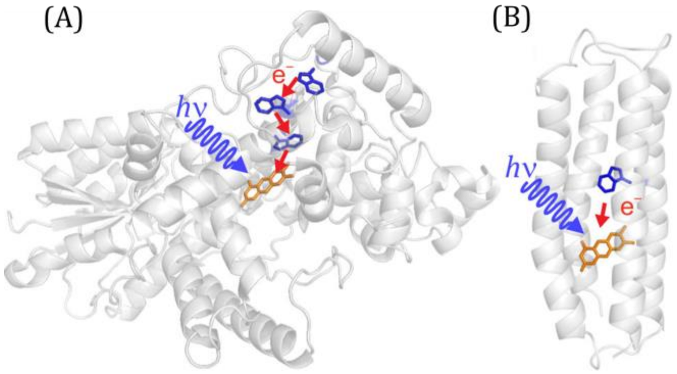

Figure 4-1: Schematic representation of A) a natural Cry and B) a maquette flavoprotein, highlighting the photoinduced ET indicated by red arrows between the flavin (orange) and Trp (blue) in both proteins. Reprinted with permission from Bialas *et al.* Copyright 2018 American Chemical Society.[42]

The rate of ET plays a key role in the photochemistry and manifestation of MFEs in cryptochromes. ET rates in natural and artificial proteins have been shown to exhibit an approximately exponential dependency on the donor-acceptor distance (see Equation 1.1)[31] and pronounced effects on the RP yield and lifetime in *Dm*Cry and *Er*Cry4 were found in the previous chapter, by altering the composition of the ET chain. Although these observations can be attributed to the effects of shortening or interrupting the ET chain, the complex nature of cryptochromes prohibits a straight forward and definitive interpretation, as the surrounding amino acids may interact in complex and unexpected ways. By designing artificial proteins from scratch, the complexity of natural cryptochromes is avoided and fundamental principles, such as the dependency of the ET rates and MFEs on the donor-acceptor distances, can be studied in well-defined, controlled, but still biologically relevant systems.

Since the maquettes are novel molecules, one of the primary aims of this chapter is the identification of the transient species formed upon photoexcitation. In the first section the photochemistry of the maquette which contains no redox active amino acid (the control) is analysed. In the control maquette no photoinduced reduction of the flavin is expected.

In the second section, a maquette with a His located one α-helical turn (~6 Å) away from the flavin is investigated. His is known to reduce flavins via hydrogen atom-transfer (HT) to form neutral radical pairs [FH$^\bullet$ His$^\bullet$].[95-96] The advantage of using a maquette design with His rather than Trp as the redox active amino acid is that His$^\bullet$ radicals, in contrast to Trp radicals, do not absorb significantly in the spectral region observed in this work. This simplifies the observed Δ*A* spectra and facilitates the identification of the $FH^{\bullet}$ spectrum.

Finally, in Sections 4.3 and 4.4, the photochemistry of a series of three maquettes containing Trp at increasing distances from the flavin (W13, W16, W20) are analysed and compared with their natural analogues, cryptochromes. Key interests of this section are the effects of increasing flavin-Trp distance on the photochemistry and MFEs of the maquettes.

4.1 Photochemistry of the control maquette

In the absence of any amino acid in the control maquette sequence to reduce the excited singlet state of the flavin, $^{1}F^{*}$, no RP formation is expected to be observed. Instead only fluorescence, ISC and relaxation of the excited triplet state, $^{3}F^{*}$, is expected, as illustrated in Figure 4-2.[s] The flavin fluorescence quantum yield was determined to be 0.11 in the control maquette by Bialas *et al.*[42] In the same study the lifetime of $^{1}F^{*}$ was measured to be ~1 ns, using time correlated single photon counting. Consequently we do not expect to observe $^{1}F^{*}$ species in this work directly, since the first Δ*A* data is recorded only after 250 ns PPD time.

---

[s] The dashed arrow indicates a photo-degradation process that was observed, leading to a flavin radical $(FH^{\bullet})^{\dagger}$, which will be explained in more detail later in this section.

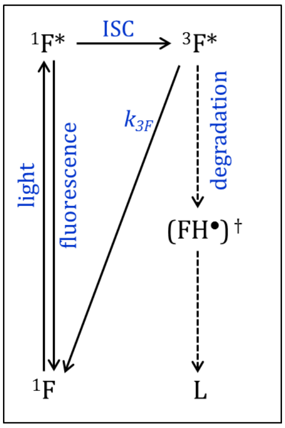

Figure 4-2: Photochemical reaction scheme appropriate for the control maquette. Upon light excitation of the flavin ground state (^{1}F) the ^{1}F* undergoes ISC to form ^{3}F*. ^{3}F* reacts along competing pathways either back to the ground state or to form a photo-degradation product lumichrome (L).

The Δ*A* spectrum observed after photoexcitation of the control maquette is shown in Figure 4-3A. Similar broad and largely featureless Δ*A* spectra are observed between 520 nm and 690 nm at PPD times between 0.25 μs to 10 μs. This is consistent with the proposed reaction cycle shown in Figure 4-2. ISC in flavins takes place on a (sub-) nanosecond timescale[97-98] and is largely complete within the 250 ns before the first Δ*A* spectrum is recorded. Hence, the majority of the Δ*A* signal is attributed to ^{3}F*. The similarity between the observed Δ*A* spectra and literature spectra of similar ^{3}F* supports the assignment (*c.f.* Figure 3-3).

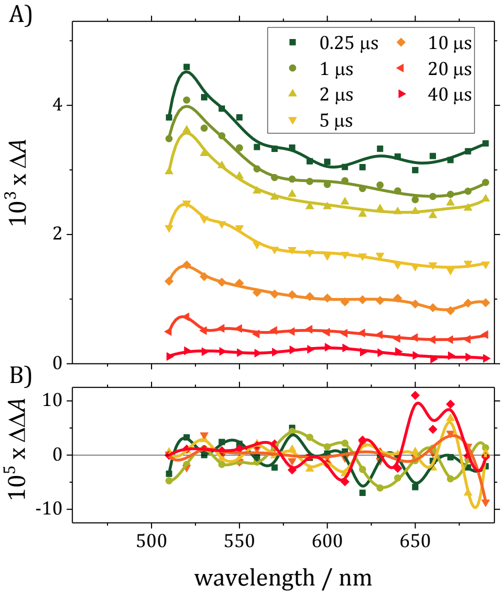

Figure 4-3: A) Δ*A* spectra and B) the ΔΔ*A* action spectra of the control maquette recorded under standard conditions (see Table 2-1) as a function of PPD delay time. Solid lines are spline fits to guide the eye.

No ΔΔ*A* is observed in the control maquette (see Figure 4-3B). Note the almost two orders of magnitude larger *y*-axis scale of Figure 4-3B compared to A. This demonstrates that in the control maquette, the reactivity of ^{3}F* is not affected by a magnetic field of 30 mT.

4.1.1 Signs of photo-degradation of the control maquette

The spectral shape of the Δ*A* spectra of the control (see Figure 4-3A) does not change significantly between 0.25 µs and 10 µs. This is consistent with the proposed decay of just one species *i.e.* ^{3}F*. The Δ*A* spectrum at 40 µs PPD time is, however, distinctly different and exhibits a maximum around 600 nm, similar to literature spectra of neutral flavin radicals. RF is known to produce flavin radicals $(FH^{\bullet})^{\dagger}$ via proton-coupled ET from the ribityl group to the isoalloxazine ring.[26-27] The reaction intermediate $(FH^{\bullet})^{\dagger}$ is structurally similar to the semi reduced neutral flavin radical $(FH^{\bullet})$ formed through the reduction by an electron donor after photoexcitation *e.g.* in Crys (see Section 3.3 and Figure 3-15). The photoreaction indicated by the dashed arrow in Figure 4-2 leads to the bond breaking between the isoalloxazine ring and the ribityl chain, and hence to permanent photodegradation of flavins and the formation of a stable photoproduct lumichrome. The relative magnitudes of the Δ*A* signal of the early PPD times (*e.g.* 0.25 µs), associated with

$^3F^*$, and that at 40 μs, attributed to $(FH^\bullet)^\dagger$, suggests a low quantum yield for the formation of $(FH^\bullet)^\dagger$.

Lumichrome was detected in the maquette control samples after photolysis using UV/VIS spectroscopy (see Figure 4-4), supporting the assumption that the observed ΔA at late PPD times is associated with the neutral flavin radical formed as a photodegradation intermediate.[42] Significantly less lumichrome accumulates during photolysis of Trp- or His- containing maquettes. This can be rationalized by the nearby Trp or His readily quenching the $^3F^*$. This effectively decreases the quantum yield of lumichrome in Trp- and His- containing maquettes compared to the control maquette.

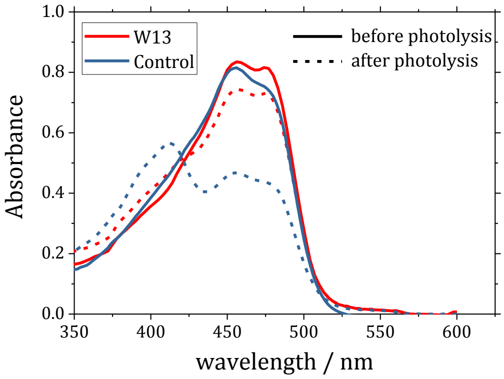

Figure 4-4: UV/VIS spectra of the control (blue) and flavomaquette W13 (red) before (solid lines) and after (dashed lines) CRDS experiments in which the samples were exposed to a total of ~25000 pulses of 1 mJ at 10/3 Hz and 450 nm. Photodegradation is more marked in the control.

4.1.2 Global target analysis

The time and wavelength resolved ΔA data presented in Figure 4-3 was analysed using global target analysis and the kinetic model described in Section 2.2. The kinetic model is based on the reaction scheme shown in Figure 4-2, and accounts for the two primary deactivation pathways of $^3F^*$:

$$^3F^* \rightarrow {}^1F \qquad 4.1$$

$$^3F^* \rightarrow (FH^\bullet)^\dagger \rightarrow L \qquad 4.2$$

Note that ^{1}F* is not considered on the grounds that A) the timescale of ISC is expected to be much faster than 250 ns and B) there is no indication of ^{1}F* in the ΔA spectra.[97-98] The calculated species associated decay spectra (S_{SADS}, see Equation 2.18) are shown in Figure 4-5.

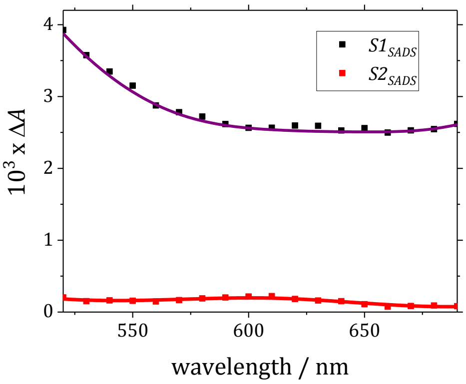

Figure 4-5: Species associated decay spectra $S1_{\mathrm{SADS}}$ (black) and $S2_{\mathrm{SADS}}$ (red) as calculated through global target analysis of the maquette control $\Delta A(t,\lambda)$. The purple and red solid lines are spline interpolations of $S1_{\mathrm{SADS}}$ and $S2_{\mathrm{SADS}}$. $S1_{\mathrm{SADS}}$ is attributed to ^{3}F* and used in the spectral model for the analysis of the Trp containing maquettes presented in Section 4.3. $S2_{\mathrm{SADS}}$ is assigned to the photodegradation intermediate $(\mathrm{FH}^\bullet)^\dagger$.

The spectral shape of $S1_{\mathrm{SADS}}$ and $S2_{\mathrm{SADS}}$ agree with literature spectra of ^{3}F* and $\mathrm{FH}^\bullet$ and $S1_{\mathrm{SADS}}$ and $S2_{\mathrm{SADS}}$ are assigned to ^{3}F* and $(\mathrm{FH}^\bullet)^\dagger$ accordingly.[85, 99-100]

4.2 Photochemistry of H6 maquette: radical pair formation and MFEs

In H6, the His located one α-helical turn away from the flavin chromophore is expected to reduce the flavin after photoexcitation to form a RP. The photochemistry of H6 is thus anticipated to be similar to the control, but with one added complexity: RP formation.

At the beginning of this section, the ΔA spectra of H6 will be analysed and contrasted with the results of the control in order to understand the effects of introducing a redox-active amino acid close to the flavin chromophore. In the second part of the section the MFE observed in the H6 will be discussed.

Figure 4-6 shows Δ*A* spectra of the maquette H6 measured as a function of PPD time. The Δ*A* spectrum of H6 is broadly similar to the Δ*A* spectrum of the control (*c.f.* Figure 4-3) with a broad, almost featureless Δ*A* band between 520 nm and 690 nm which has been attributed to ^{3}F*. The bleaching of the flavin ground state is observed as a negative contribution to the Δ*A* signal below 520 nm.

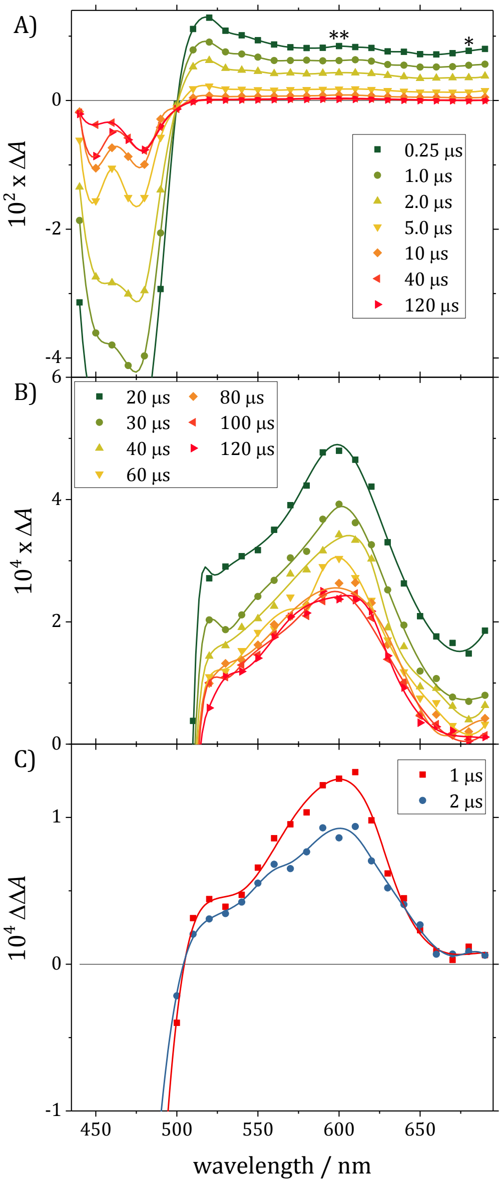

Figure 4-6: A), B) Δ*A* spectra and C) the ΔΔ*A* action spectra of maquette H6, recorded under standard conditions (see Table 2-1) as a function of PPD delay time. The Δ*A* spectra shown in A) and B) are from the same measurement with a focus on early and late PPD times, respectively. The ΔΔ*A* is determined as ΔΔ*A* = Δ*A*(30 mT) – Δ*A*(0 mT). The Δ*A* at 680 nm, dominated by the Δ*A* associated with ^{3}F*, is marked with * and the Δ*A* at 600 nm, where FH$^\bullet$ exhibits an absorption maximum, is marked with ** (see text for more details). Solid lines are spline fits to guide the eye.

In contrast to the control, a local maximum in the Δ*A* signal is observed at around 600 nm at early PPD times (*e.g.* 0.25 μs). Since His is known to readily reduce flavins to form neutral radical pairs of the form [FH$^\bullet$ His$^\bullet$]95-96 and His radicals do not absorb significantly in the visible, this additional ΔA is attributed to the formation of $FH^{\bullet}$. The position of the local ΔA absorbance maximum (~600 nm) is in good agreement with the ΔA of $FH^{\bullet}$ observed in other flavoproteins.[100] This supports the assignment of the ΔA peak to $FH^{\bullet}$ and the following reaction scheme for H6 is proposed, which is similar to that of the control but includes the RP formation through hydrogen-transfer (HT) from His to the flavin to form a RP comprised of $FH^{\bullet}$ and the neutral His radical $His^{\bullet}$ (see Figure 4-7).

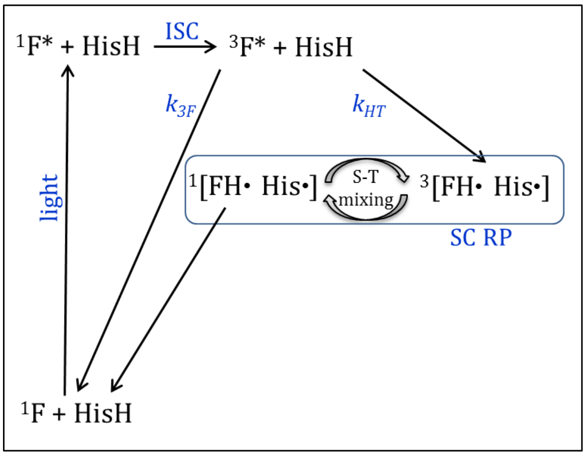

Figure 4-7: Photochemical reaction scheme appropriate for H6. Upon light excitation of the flavin ground state (^1F) the $^1F^*$ undergoes ISC to form $^3F^*$. $^3F^*$ reacts along competing pathways to either relax back to the ground state or to form a SC RP comprised of $FH^{\bullet}$ and $His^{\bullet}$.

The relative magnitude of the ΔA at 680 nm, where only $^3F^*$ is expected to absorb significantly, and the ΔA at 600 nm, where both $^3F^*$ and $FH^{\bullet}$ absorb strongly, suggests a relatively low quantum yield of the $[FH^{\bullet}\ His^{\bullet}]$ RP.

Between 0.25 µs and 5 µs the ΔA signal decreases over the entire wavelength range with little change in the spectral shape. The ΔA signal at 680 nm, shown in Figure 4-8 as a function of PPD time decays approximately exponentially with a rate constant of $k_{H6} = 0.31 \pm 0.03\ \mu s^{-1}$. For comparison, in the control, the ΔA signal measured at 680 nm decays at $k_C = 0.13 \pm 0.01\ \mu s^{-1}$ (shown as open black symbols in Figure 4-8).

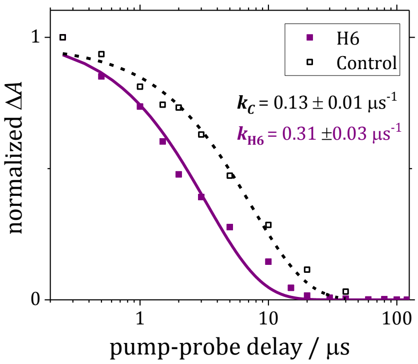

Figure 4-8: Δ*A* measured at 680 nm as a function of PPD time for the H6 and control maquettes. This is a representation of data shown previously in Figure 4-3 and Figure 4-6 of the control (black) and H6 (purple) to compare the time dependence of the Δ*A*. Lines represent single exponential fits (see text for details).

As in the control, the decrease in Δ*A* at 680 nm in H6 reflects the decrease in the concentration of ^{3}F*. The decay observed in H6 is significantly faster than in the control. This is consistent with the proposed reaction cycles, where in the H6, the ^{3}F* is reduced by the nearby His in addition to the quenching processes occurring in the control (see Equation 4.1):

$$^3\mathrm{F}^* + \mathrm{HisH} \xrightarrow{k_{\mathrm{HT}}} \mathrm{FH}^\bullet + \mathrm{His}^\bullet. \qquad 4.3$$

k_{HT} describes the rate for an intramolecular HT between the amino acid His and the ^{3}F*. The decrease of the ^{3}F* concentration can be described using Equation 4.1 and 4.3 assuming irreversible first order reaction kinetics:

$$[\,^3\mathrm{F}^*] = [\,^3\mathrm{F}^*]_0 e^{-(k_{3\mathrm{F}}+k_{\mathrm{HT}})t}. \qquad 4.4$$

We can estimate $k_{\mathrm{HT}} \approx 0.18\ \mu\mathrm{s}^{-1}$ using $k_{\mathrm{HT}} = k_{\mathrm{H6}} - k_{3\mathrm{F}}$, under the assumption that the rate constants $k_{3\mathrm{F}}$ are similar in H6 and the control (*i.e.* $k_{\mathrm{C}} \approx k_{3\mathrm{F}}$).

The single exponential fit of the Δ*A* measured at 680 nm for H6 (see Figure 4-8) is not highly satisfactory and in particular doesn't capture the temporal evolution between 5 µs and 15 µs well. This discrepancy is attributed to conformational inhomogeneity of the maquettes and the resulting range in the donor-acceptor distance. Even small differences in the donor-acceptor distance may have pronounced effects on the observed rate of HT.

Therefore, a strictly single exponential decay of $^3F^*$ is not expected, but rather a stretched exponential which reflects the conformations with shorter/longer donor-acceptor distances and hence larger/smaller rate constants associated with the quenching of the $^3F^*$.

Between 0.25 μs and 40 μs the ΔA signal drops by almost two orders of magnitude and the spectral shape changes significantly from a broad almost featureless spectrum to one which resembles that of $FH^\bullet$ (see Figure 4-6A and B).[100] Between 80 μs and 120 μs the spectral shape is approximately constant and no further decay is observed. This is consistent with the proposed formation of a [$FH^\bullet$ $His^\bullet$] RP which exhibits a long lifetime and is produced at a relatively low quantum yield. The ΔA spectra measured at PPD times ≥80 μs are therefore assigned to $FH^\bullet$.

In contrast to the control, a pronounced MFE is observed in the H6. In Figure 4-6C the $\Delta\Delta A$ spectra measured at 1 μs and 2 μs PPD show a positive MFE for a 30 mT field, which suggest a triplet-born RP, consistent with the suggested photocycle (for details on the interpretation of the sign of MFEs see Section 1.4.1).

The spectral shape of the $\Delta\Delta A$ measured at 1 μs and 2 μs PPD is almost identical to the ΔA spectrum measured at 100 μs PPD time (see Figure 4-9). This supports the assignment of the spectrum to $FH^\bullet$ and the proposed formation of a magnetically sensitive SC RP between the F and His.

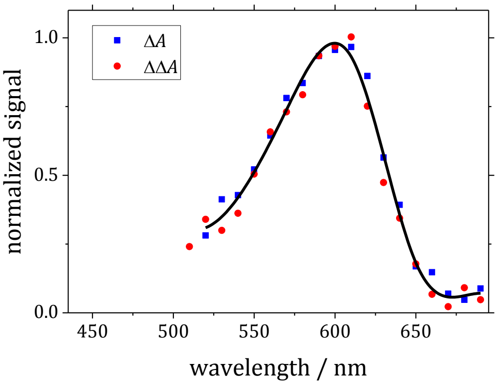

Figure 4-9: Comparison of the Δ*A* spectrum of H6 recorded at 100 µs PPD time (blue) with the ΔΔ*A* spectrum recorded at 1 µs (red) (see Figure 4-6B and C). A spline fit of the average is shown as a solid black line. The similarity of the two spectra lends support to the assignment of the spectral feature centred on 600 nm to $FH^{\bullet}$ and the proposed formation of a magnetically sensitive RP comprising $FH^{\bullet}$.

No significant ΔΔ*A* signal is observed in the wavelength region beyond 650 nm. This provides strong evidence that, as in the control maquette, $^3F^*$ is not a magnetically sensitive species.

4.3 Photochemistry of flavomaquettes with varying donor-acceptor distance

In this section the dependency of the ET rate on the donor-acceptor distance is investigated in detail, using a series of three maquettes with increasing flavin-Trp distance (see Figure 4-10).

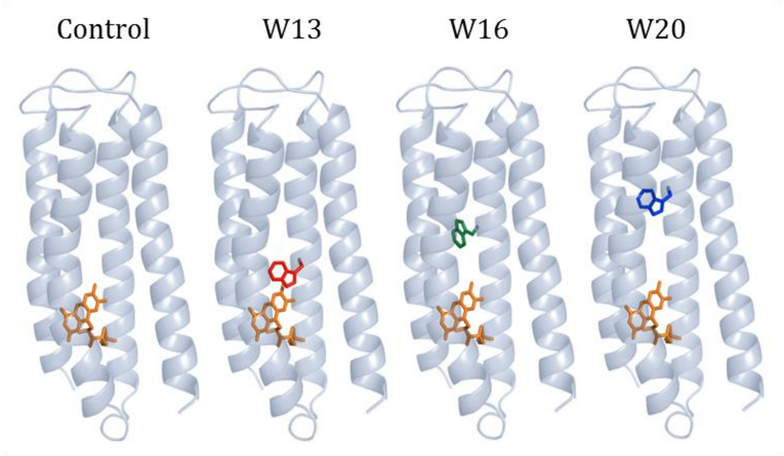

Figure 4-10: Schematic representation of the control maquette, which does not contain a redox active amino acid and a series of three maquettes with one Trp at increasing distance from the flavin: W13 (red), W16 (green), and W20 (blue). Reprinted with permission from Zollitsch *et al.* Copyright 2018 American Chemical Society.[94]

Given the distances of approximately 5.6 Å to 16.8 Å between the flavin and the Trp in W13, W16, and W20, ET is expected to take place in all three designs, albeit at significantly different rates. Figure 4-11 shows the photocycle proposed for W20, W16, and W13, where, following photoexcitation and ISC, a SC RP (RP1) is formed between the flavin and the Trp through ET. After the SC RP is formed in the triplet spin state, conserving its precursor spin state, it undergoes magnetically sensitive S-T interconversion. Spin-selective charge recombination from the singlet state and change in protonation state to form RP2, which is not spin selective, are competing reaction pathways for RP1.

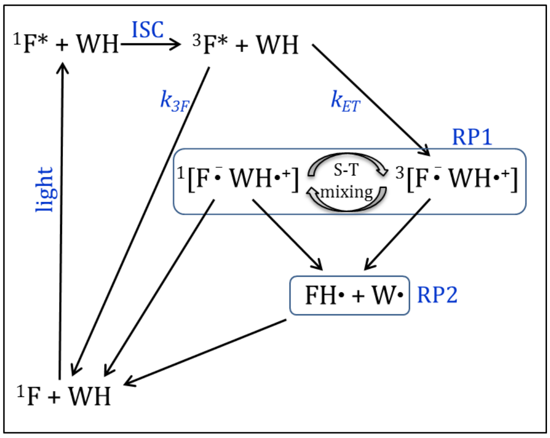

Figure 4-11: Photochemical reaction scheme proposed for W20, W16, and W13. Upon light excitation of the flavin ground state $^1F^*$ is formed. Fast ISC and reduction by a nearby Trp leads to the formation of a RP comprised of $F^{\bullet -}$ and $WH^{\bullet +}$ (RP1). RP1 undergoes magnetically sensitive coherent singlet-triplet mixing and can either recombine or change protonation state to form RP2. Since charge recombination occurs only from the singlet state, an external magnetic field has an effect on both the lifetime of RP1 and the quantum yield of RP2.[83]

According to the Moser-Dutton ruler introduced in Section 1.1.2, the ET rate constant depends exponentially on the donor-acceptor distance. The rate constants for the ET between the Trp and $^3F^*$ have been estimated based on the Moser-Dutton ruler to be 2.6 $\times 10^{11}$ s^{-1}, 1.1 $\times 10^{8}$ s^{-1}, and 4.9 $\times 10^{4}$ s^{-1} for W13, W16, and W20 respectively.[42] In this estimate, the distance of the β-carbons (5.6 Å, 11.2 Å, and 16.8 Å for W13, W16, and W20) have been used as an approximation for the edge-to-edge distance R in the Moser-Dutton ruler (see Equation 1.1).

Note that unlike natural flavoproteins, the flavomaquettes do not contain a specific binding pocket for the flavin cofactor, and the covalent attachment of the flavin to a Cys sidechain is flexible. Although the distances between the β-carbons of the respective amino acids are potentially good estimates for the average flavin-Trp distance, the flexibility of the maquette structure itself and the length and flexibility of the covalent link used to attach the RF to the cysteine (see Figure 2-8) are expected to give rise to a distribution of possible flavin-Trp distances rather than one distinct distance. The presence of multiple flavomaquette conformers with varying flavin-Trp distances results in dynamic inhomogeneity of the maquettes, such that conformers with shorter flavin-Trp distances are expected to exhibit larger ET rate constants and *vice versa*.

For simplicity, the ET pathway from the singlet is not included in the scheme, since there is no direct evidence for that process in the data presented in this section. We cannot, however, exclude the possibility of ET from the singlet state due to the limited time resolution of the experiment. The formation of singlet-born RP competes with ISC and is most likely in maquettes with short flavin-Trp distances, *i.e.* W13. It is not surprising that no singlet-born RPs are observed, since the lifetime, of singlet-born RPs in maquette conformers with short flavin-Trp distances are likely to be on a (sub-) nanosecond timescale, and these species are hence too short-lived to be detected by the experiments performed in this work.

4.3.1 The Δ*A* spectra of W13, W16, and W20

The Δ*A* spectra of W20, W16, and W13 measured as a function of PPD times are shown in Figure 4-12A, B, and C respectively. The same data as in Figure 4-12A, B, and C is shown in Figure 4-12D, E, and F, but on the same *y*-scale, so that the difference in the magnitude of the Δ*A* signal can be more easily compared between the maquettes with different flavin-Trp separation.

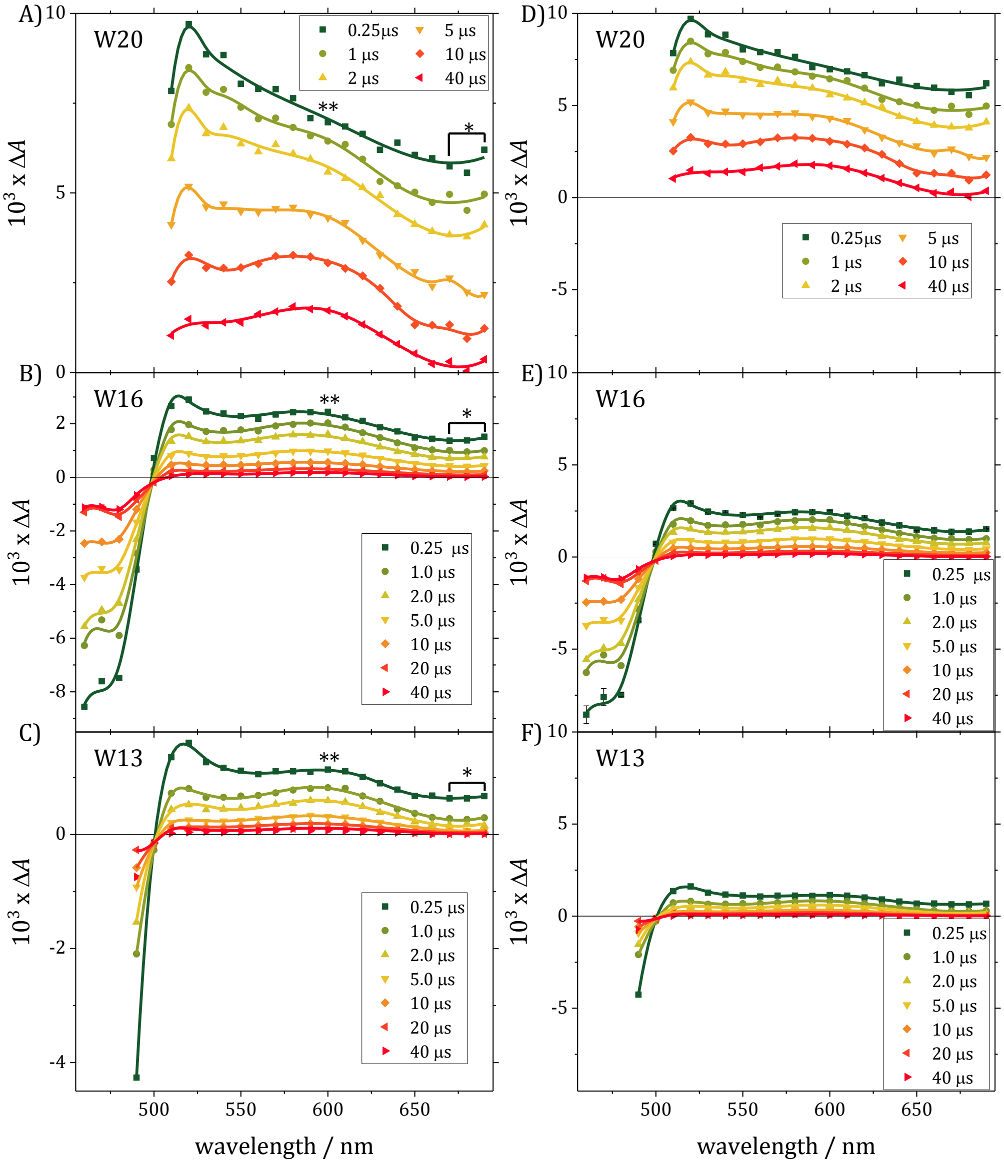

Figure 4-12: ΔA spectra of A) W20, B) W16, and C) W13 recorded under standard conditions (see Table 2-1) as a function of PPD delay time. The ΔA at 670 nm to 690 nm (where ^{3}F* absorbs predominantly) and 600 nm are marked with * and **, respectively. The solid lines represent spline fits to guide the eye. The data shown in D), E), and F) is the same as in A), B), and C) but on identical *y*-scales to facilitate comparison of the magnitude of the ΔA signal between maquettes.

As in the control, a broad absorbance between 520 nm and 690 nm is observed, along with a negative ΔA signal below 510 nm associated with the bleaching of the ground state.

In contrast to the control, the Δ*A* spectra of all three Trp containing maquettes exhibit a pronounced Δ*A* feature with a maximum at ~600 nm in addition to the broad featureless Δ*A* attributed to the 3F*.[t] A similar Δ*A* band, peaking at 600 nm, was observed in the H6 maquette and attributed to the formation of $FH^\bullet$ (see Figure 4-6). The absence of a pronounced Δ*A* feature in the control and the presence of a strong Δ*A* band in all maquettes containing a redox active amino acid in the vicinity of the flavin chromophore lends further support to the assignment of that absorption feature to $FH^\bullet$.

Despite the similarities in spectral shape, the Δ*A* signals of W20, W16, and W13 decay at significantly different rates. While more than 40% of the Δ*A* signal observed after 0.25 µs PPD time in W20 is still present after 10 µs PPD time, in both W16 and W13 the signal has decreased by ~80% after 10 µs.

$^3F^*$ is expected to be the dominant absorber in the wavelength range between 670 nm and 690 nm (marked with * in Figure 4-12).[59, 100-102] The temporal evolution of the average Δ*A* observed at 670 nm, 680 nm and 690 nm, Δ*A*(670 nm – 690 nm), of the control, W13, W16, and W20 is illustrated in Figure 4-13A. The decay of the Δ*A*(670 nm – 690 nm) of Trp containing flavomaquettes is significantly faster than in the control. This reflects the additional quenching pathway of $^3F^*$, reduction by Trp through ET, available to Trp containing maquettes. This interpretation is supported by the fact that the lifetime of the Δ*A*(670 nm – 690 nm) signal decreases with decreasing distance between the flavin and Trp, consistent with the prediction of the Moser-Dutton ruler (see Figure 4-13A).[31]

---

[t] A small residual Δ*A* signal with a spectral shape similar to that of $FH^\bullet$ is observed in the control and attributed to a photodegradation intermediate structurally similar to $FH^\bullet$. Despite the similarity in the spectral shape of the Δ*A* signal, it is distinctly different in magnitude as well as the time scale over which it is detectable. For more details see Section 4.1.1.

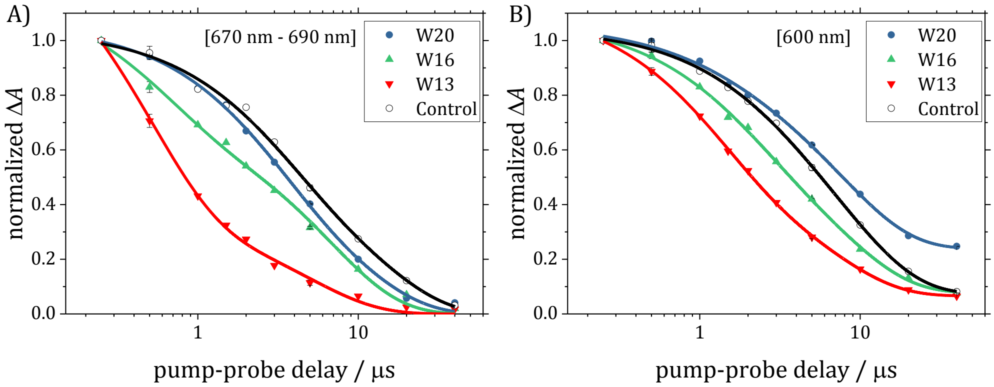

Figure 4-13: Normalized Δ*A* signals of W20, W16, W13, and the control, measured under standard conditions (see Table 2-1) as a function of PPD times measured A) as the average Δ*A* at 670 nm, 680 nm, and 690 and B) at 600 nm. The solid lines are shown to guide the eye. Representative error bars are shown at 0.5 μs PPD times as one SEM.

The Δ*A* signal measured at 600 nm, Δ*A*(600 nm), is marked with ** in Figure 4-12 and shown in Figure 4-13B as a function of PPD time. At 600 nm both FH$^\bullet$ and ^{3}F* contribute significantly to the overall ΔA.[100] Consequently, the decrease in Δ*A*(600 nm) due to the decrease in ^{3}F* concentration is partly compensated by the increase in the Δ*A* due to the formation of FH$^\bullet$. Hence, in Trp containing maquettes, the decay of Δ*A*(600 nm) is faster than the decay of Δ*A*(670 nm – 690 nm), while in the control the rate of decay of Δ*A*(600 nm) and Δ*A*(670 nm – 690 nm) is very similar and in both cases a measure for the decrease in ^{3}F* concentration. Furthermore, the lifetime of the RP is expected to increase with increasing flavin-Trp distance. This consistent with the observation of a decay component of the Δ*A*(600 nm) in W20 with a lifetime much larger than in the W13 and W16 maquettes (see Figure 4-13B). Note that there is no long-lived component observed in W20 between 670 nm to 690 nm where ^{3}F* absorbs predominantly but not FH$^\bullet$. This is consistent with the assignment of the respective absorption regions and the suggested formation of a long-lived flavin-Trp RP.

A clear difference in the magnitude of the Δ*A* observed in W20, W16, and W13 is visible in Figure 4-12D, E, and F. The Δ*A* measured after 0.25 μs PPD time in W13 is almost an order of magnitude smaller than in W20. The difference in Δ*A* reflects the difference in the lifetime of the transient species. In W13 both the quenching of ^{3}F* through ET to form flavin-Trp RPs and the charge recombination of the RP is expected to be much faster than in W20 and intermediate in W16. Given the short donor acceptor distance (~6 Å) in W13, ET and charge recombination are likely to take place largely before first data points are recorded at 0.25 μs PPD and only a fraction of the transient species formed are left after 0.25 μs. A larger fraction of transient species remaining after 0.25 μs is expected in W16 and W20 given their larger flavin-Trp distance, which explains the observed trend in the Δ*A* magnitude.

4.3.2 Global target analysis of the Δ*A* spectra of W13, W16, and W20

In the previous section the Δ*A* of the Trp containing maquettes is discussed qualitatively and rationalized with regard to the proposed photoreaction cycle. In this section, the Δ*A* of W20, W16, and W13 is analysed using global target analysis in order to gain more quantitative insight into the kinetic processes. A spectral model is used based on the method presented in Section 2.2 and described in more detail below.

4.3.2.1 Spectral model

The analysis of the Δ*A* presented in Section 4.3.1 provides evidence that the photocycle in Figure 4-11 appropriately describes the photochemistry of the Trp containing maquettes. Based on this finding, Δ*A* is analysed using a spectral model based on reference spectra of the following transient species: 3F*, $W^\bullet$, $F^{\bullet-}$, and $FH^\bullet$ (see Figure 4-14).[u]

---

[u] Note that some species, such as $WH^{\bullet+}$ and $^1F^*$ are not included. Reasons for that will be explained in the remainder of this section.

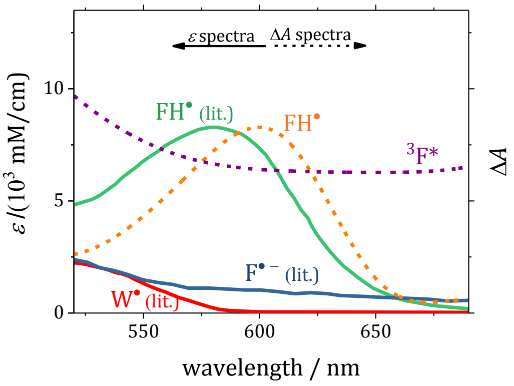

Figure 4-14: Reference spectra of various excited flavin and Trp species used in the spectral deconvolution. Spectra with solid lines are taken from literature.[69, 100-101] Differential absorbence spectra for $^3F^*$ (purple) and $FH^\bullet$ (orange) are obtained through ΔA and MFE studies on the control and H6 rsepectively.

The spectra shown as solid lines for $W^\bullet$ (red), $F^{\bullet-}$ (blue), and $FH^\bullet$ (green) were obtained from the literature. The spectrum for:

- $W^\bullet$ was measured by Solar *et al.* by pulse radiolysis of Trp in aqueous solution.[69]
- $F^{\bullet-}$ was obtained through photoexcitation of a similarly substituted and protein bound flavin by Raibekas *et al.*[101]
- $FH^\bullet$ was recorded by Ghisla *et al.* through the reduction of protein bound 8-OH-FMN.[100] The purpose of this spectrum is to illustrate the relative magnitudes of extinction coefficents of excited flavin and Trp species in this wavelength range. Note that this spectrum is not used as reference spectrum in the global target analysis.

The reference spectra for $^3F^*$ (purple) and $FH^\bullet$ (orange) were determined in this work through global target analysis of the ΔA of the control and MFE studies on the H6 maquette respectively (see Section 4.1 and 4.2). Note that the spectra taken from literature, shown as solid lines, are in units of [10^3 mM/cm], while the spectra obtained from data in this work, shown as dashed lines, are in arbitrary ΔA units.

Despite the formation of $^1F^*$ upon photoexcitation, no significant $^1F^*$ concentration is expected after 0.25 μs PPD time due to fast ISC.[97] This is supported by evidence from TA experiments with picosecond time resolution performed by Jarocha *et al.* (unpublished data) and time-correlated single photon counting measurements.[42]

With a pK_a of 4.3, the $WH^{\bullet +}$ radical is likely to deprotonate on a nanosecond timescale at the pHs used here.[69, 82]

The data (ΔA and MFE) presented in this work support the assignment of the reference spectra to the observed ΔA spectra. But, given the similarity of the absorption of $FH^{\bullet}$ and $WH^{\bullet +}$, the presence of $WH^{\bullet +}$ cannot be excluded entirely, based solely on the data presented in this work. More evidence supporting the assignment of the ΔA spectra will be presented in the following sections, and further picosecond TA measurements are planned to investigate the deprotonation of $WH^{\bullet +}$ directly.

4.3.2.2 Results and discussion

Figure 4-15 shows the ΔA data (symbols) and the result of the global target analysis (lines) of W20, W16, W13, and the control. Good agreement between the ΔA and the fit was achieved at all PPD times in all four maquettes *i.e.* the ΔA data of the Trp containing maquettes can be rationalized adequately by the presence of the $^3F^*$, RP1 ($[F^{\bullet -}\ W^{\bullet}]$), and RP2 ($[FH^{\bullet}\ W^{\bullet}]$), consistent with the proposed photocycle (see Figure 4-11).

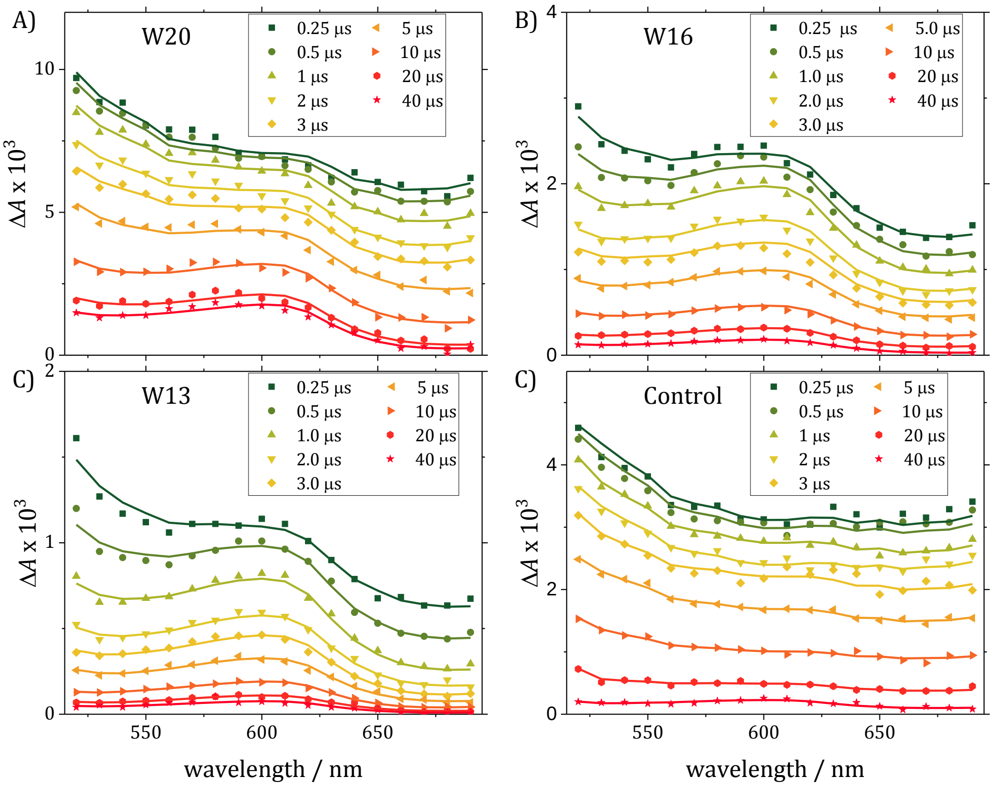

Figure 4-15: Differential absorbance (Δ*A*) spectra (symbols) and fit spectra (lines) of A) W20, B) W16, W13 and C) the control recorded under standard conditions (see Table 2-1) as a function of PPD delay time.

The concentration profiles of $^3F^*$, $F^{\bullet-}$, $FH^{\bullet}$, and $W^{\bullet}$, as estimated through global target analysis, are summarized in Figure 4-16 for W20, W16, W13, and the control maquette.

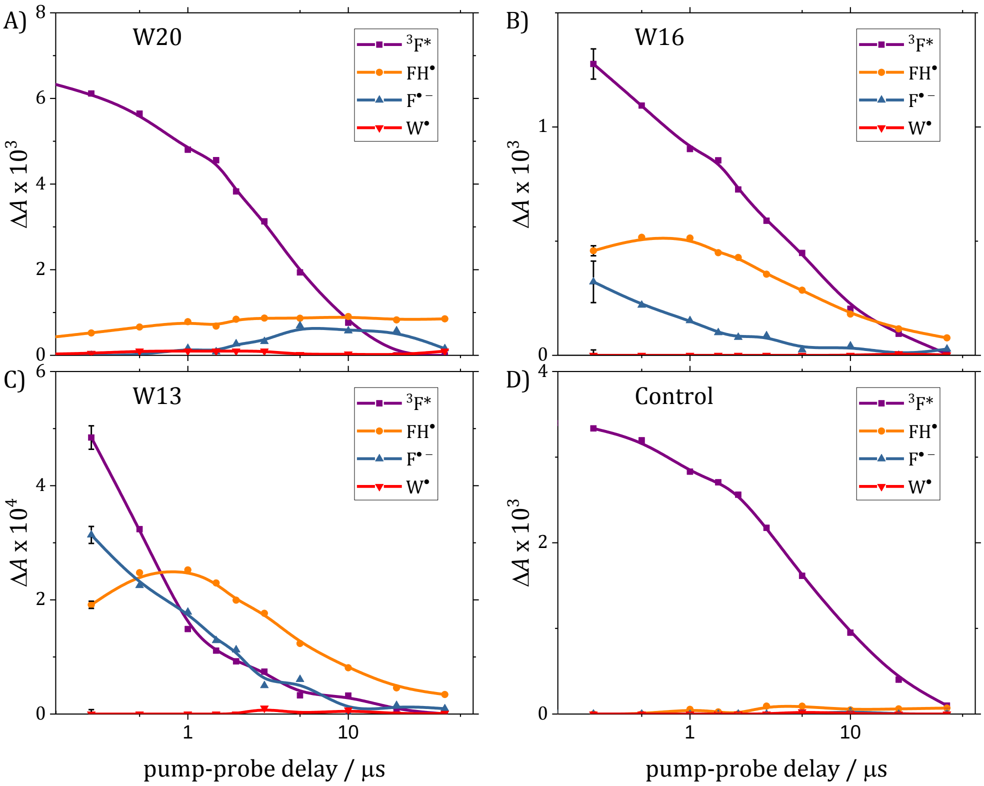

Figure 4-16: The contribution coefficients c_i for i = ^{3}F*, F$^{\bullet-}$, FH$^\bullet$, and W$^\bullet$, as a function of PPD time for A) W20, B) W16, C) W13, and D) the control maquette. The c_i are directly proportional to the concentration of species i and hence facilitate the analysis of the time dependence of the concentration of the respective species (see text and Section 2.2.2 for more detail). Representative uncertainties are shown for t = 0.25 μs; those in panels (A) and (D) are smaller than the size of the symbols. The solid lines represent spline fits to guide the eye. A comparison between the c_i of ^{3}F* and FH$^\bullet$ of all four maquettes is shown in Figure 4-17 and Figure 4-18.

At early PPD times, the contribution of ^{3}F* is the largest in all maquettes. This reflects both a high relative concentration of ^{3}F* at early PPD times and the fact that ^{3}F* absorbs strongly in the observed wavelength region.

In contrast W$^\bullet$ contributes very little to the overall Δ*A*, which can be attributed to the fact that W$^\bullet$ generally absorbs relatively weakly between 520 nm and 690 nm. The magnitude of the contribution of W$^\bullet$ is still less than expected, according to the extinction coefficient estimated based on the spectrum measured of W$^\bullet$ by Solar *et al.* (see Figure 4-14).[42, 69] This could be rationalized by an enzymichromic shift towards shorter wavelengths, which is commonly observed in Trp radicals, further reducing the overall absorption of $W^{\bullet}$ in the observed wavelength region.[68, 70-72, 87]

In W20 the largest contribution is attributed to $^3F^*$ (~90% at 0.25 μs PPD time) which decays exponentially, followed by $FH^{\bullet}$ (~10% at 0.25 μs PPD time). By comparison, in W16 and W13A, a significantly larger fraction is associated with the radical species $F^{\bullet-}$ and $FH^{\bullet}$ at early PPD times. Both radicals together account for ~40% and ~50% of the overall ΔA respectively at 0.25 μs PPD time. This trend of increasing relative RP quantum yield is consistent with the expected trend of increasingly large ET rate constants with decreasing flavin-Trp distance. In W16 and W13 the $F^{\bullet-}$ contribution decays within 10 μs while the $FH^{\bullet}$ contribution persists beyond the 40 μs time frame of the measurement. These findings are in good agreement with the suggested photocycle and provide evidence for the formation of a relatively short-lived $F^{\bullet-}$ radical which protonates to form a longer lived $FH^{\bullet}$ radical.

As expected, in the control maquette only $^3F^*$ contributes significantly to the overall ΔA.

Although the ΔA data of all three Trp maquettes is consistent with the same proposed reaction cycle, it is clear from Figure 4-16, that their kinetic parameters vary significantly. In the following subsection, the lifetime of the $^3F^*$ is examined to gain quantitative insight into the differences in the ET rates. In the subsequent subsection the rate of RP2 formation and RP2 lifetimes are compared between the different maquette designs based on the respective $FH^{\bullet}$ time profiles.[v]

Excited Triplet $^3F^*$

To allow a straight forward easy comparison of the rate of decrease in $^3F^*$ concentration, the normalized c_{3F} time traces of W20, W16, W13, and the control are shown in Figure 4-17. It is clear from the figure that the rate of decay within the first 5 μs follows the expected trend: (slowest) control < W20 < W16 < W13 (fastest). This trend reflects the fact that the introduction of a Trp in the vicinity of the flavin opens up an additional

---

[v] The overall absorption of $^3F^*$ and $FH^{\bullet}$ is approximately an order of magnitude higher than that of $W^{\bullet}$ and $F^{\bullet-}$ in the observed wavelength region. $W^{\bullet}$ and $F^{\bullet-}$ also lack a distinctive spectral feature in the observed wavelength region. Consequently the contribution of these species obtained from the spectral deconvolution cannot be resolved with the same certainty as the $^3F^*$ and $FH^{\bullet}$. Therefore the remainder of the analysis will focus on $^3F^*$ and $FH^{\bullet}$ when making qualitative comparisons between the different flavomaquette designs.

reaction pathway, which becomes increasingly dominant with decreasing flavin-Trp distance.

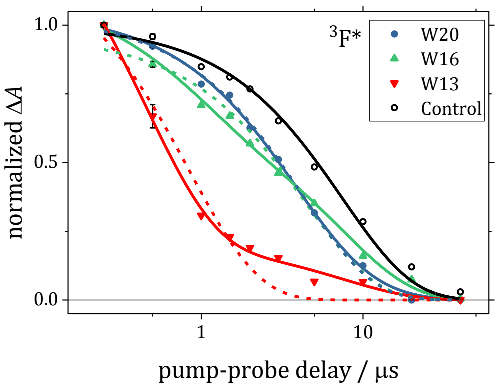

Figure 4-17: Normalized time-profiles of the ^{3}F* concentration for W20 (blue), W16 (green), W13 (red), and the control (black) as estimated by global target analysis described in Section 2.2 and the beginning of this section. All signals are scaled to the amplitude of ^{3}F* measured at 0.25 µs. The error bars shown at 0.5 µs show the estimated standard deviations and are representative of the uncertainty at all PPD times. The dashed and solid lines represent exponential fits (see text for more details) and the results are summarized in Table 4-1.

In the control only one major reaction pathway is considered in the loss of ^{3}F*:

$$ {}^3\mathrm{F}^* \xrightarrow{k_{3\mathrm{F}}} {}^1\mathrm{F} \qquad 4.5 $$

and the decrease in ^{3}F* concentration in the control is approximated by a single exponential decay function:

$$ \left[\,{}^3\mathrm{F}^*\,\right] = \left[\,{}^3\mathrm{F}^*\,\right]_0 e^{-k_{3\mathrm{F}}t}. \qquad 4.6 $$

The rate constant $k_{3\mathrm{F}}$ = 0.133 ±0.008 µs^{-1} for the control is estimated by fitting the $c_{3\mathrm{F}}$ time profile shown as a black line in Figure 4-17. Small deviations from this simplistic model (compare black scatter and black line in Figure 4-17) are expected, since only a single rate constant is used as approximation to describe the decrease in $\left[\,{}^3\mathrm{F}^*\,\right]$, which can react via multiple deactivation pathways including ISC and bimolecular reactions, such as quenching of ^{3}F* by triplet oxygen.[23, 27]

In maquettes containing the redox active amino acid Trp, ET is considered as an additional reaction pathway:

$$ {}^{3}\mathrm{F}^{*} \xrightarrow{k_{\mathrm{ET}}} \mathrm{F}^{\bullet -}. \qquad 4.7$$

Assuming irreversible first order reaction, the concentration of $^{3}F^{*}$ can than be described based on 4.5 and 4.7 as:

$$\left[\,{}^{3}\mathrm{F}^{*}\,\right] = \left[\,{}^{3}\mathrm{F}^{*}\,\right]_{0} e^{-(k_{3\mathrm{F}}+k_{\mathrm{ET}})t} = \left[\,{}^{3}\mathrm{F}^{*}\,\right]_{0} e^{-k_{2}t}, \qquad 4.8$$

where $k_2 = k_{3\mathrm{F}} + k_{\mathrm{ET}}$. Fits of the normalized $c_{3\mathrm{F}}$ using Equation 4.8 are shown as dashed lines in Figure 4-17. These single exponential fits are unsatisfactory in both W13 and W16 and, for example, do not reflect the long-lived component in W13 or the fast decay at early PPD times in W16 adequately. The deviation of a single exponential decay as described by Equation 4.8 is attributed to the aforementioned dynamic heterogeneity due to the presence of conformers with different flavin-Trp distances.

Estimations based on the Moser-Dutton ruler and the β-carbon distance predict an ET rate constant of 0.26 ps^{-1} in W13 and a rate constant for the charge recombination of 0.63 ps^{-1}.[42] This suggests that any conformer with an edge-to-edge distance similar to the β-carbon distance should have a lifetime far shorter than 0.25 µs, which is the PPD time where the first data point is recorded. Although the estimated rate constants for ET and charge recombination are based on rather crude approximations, this demonstrates that the observed RP is unlikely one with a flavin-Trp edge-to-edge distance of only 5.6 Å, the β-carbon distance in W13, but rather a conformation where the flavin and Trp are pointing away from each other, increasing the flavin-Trp separation.

As mentioned before, the flexibility of the maquette structure and the flavin attachment allows for a range of conformations with different flavin Trp distances. We therefore do not expect a distinct decay rate constant to describe the ET associated with a single maquette conformer and flavin-Trp edge-to-edge distance. Instead we expect the presence of maquette conformers which exhibit a range of Flavin-Trp edge-to-edge distances and consequently a range of ET rate constants. As a result, the observed decrease in $^{3}F^{*}$ is better described by a linear combination of exponential decays of the form of Equation 4.8 weighted by the relative concentration of the respective conformers.

To approximate the dynamic heterogeneity two subsections of maquette are considered: A) maquettes with large flavin-Trp distances where $k_{\mathrm{ET}} \ll k_{3\mathrm{F}}$, and B) maquettes where k_{ET} is on the same order of magnitude or faster than $k_{3\mathrm{F}}$.[w]

A) The subset of maquettes where $k_{\mathrm{ET}} \ll k_{3\mathrm{F}}$ are inactive, in the sense that no flavin-Trp RPs are formed. Thus this subset of maquettes is expected to react similarly to the control maquette. From the kinetic analysis of the control maquette, the rate constant for the loss of ^{3}F* in the absence of the electron donor Trp has been calculated to be 0.133 ±0.008 μs^{-1}. For conformers with large flavin-Trp distances where $k_{3\mathrm{F}}$ is much larger than k_{ET} we can therefor approximate the change in ^{3}F concentration with

$$[\,^3\mathrm{F}^*\,] = [\,^3\mathrm{F}^*\,]_0 e^{-(k_{3\mathrm{F}}+k_{\mathrm{ET}})t} \approx [\,^3\mathrm{F}^*\,]_0 e^{-k_{3\mathrm{F}}t}. \qquad 4.9$$

B) In maquettes where k_{ET} is on the same order of magnitude or faster than $k_{3\mathrm{F}}$, RP formation competes efficiently with other deactivation pathways and the decrease in ^{3}F* is described by:

$$[\,^3\mathrm{F}^*\,] = [\,^3\mathrm{F}^*\,]_0 e^{-(0.133\,\mu s^{-1}+k_{\mathrm{ET}})t}. \qquad 4.10$$

To describe the temporal evolution of the overall ^{3}F* concentration, the $c_{3\mathrm{F}}$ of the Trp containing maquettes (see Figure 4-17) is approximated by the linear combination of Equation 4.9 and 4.10 to account for the respective active and inactive maquette subsets:

$$[\,^3\mathrm{F}^*\,] = [\,^3\mathrm{F}^*\,]_{\mathrm{A}} e^{-k_{3\mathrm{F}}t} + [\,^3\mathrm{F}^*\,]_{\mathrm{B}} e^{-(0.133\,\mu s^{-1}+k_{\mathrm{ET}})t} \qquad 4.11$$

$[\,^3\mathrm{F}^*\,]_{\mathrm{A}}$ and $[\,^3\mathrm{F}^*\,]_{\mathrm{B}}$ represent the initial concentration of maquettes in an inactive (A) and active (B) state respectively. The results of fitting $c_{3\mathrm{F}}$ using Equation 4.11 are shown as solid lines for W20, W16, and W13 in Figure 4-17. The fits using Equation 4.11 represent the evolution of the decay traces more accurately than the fits based on Equation 4.8 (dashed lines). The most obvious improvements are observed in the fit of W13, and are significantly less marked for W20 and intermediate for W16. This trend reflects that, due to the exponential dependency of the ET rate constant on the edge-to-edge distance (R),

---

[w] Alternatively dynamic heterogeneity due to the presence of a distribution of conformers can be accounted for by introducing an exponential stretch factor.[39] This approach did not lead to satisfactory fits due to the limited time resolution and number of time points at early PPD times in W13.

the ET rate is more sensitive to a difference in *R* at small *R*. The resulting parameters of the fits are summarized in Table 4-1.

Table 4-1: Rate constants and pre-exponential factors obtained from fitting the decay of ^{3}F* and FH$^\bullet$.

	$^\#[\,^3F^*\,]_A$	k_{3F} /μs^{-1}	$^\#[\,^3F^*\,]_B$	k_{ET} /μs^{-1}
Control	1.00 ±0.02	0.133 ±0.008	–	–
W20	0.29 ±0.14	0.133*	0.71 ±0.14	0.171 ±0.054
W16	0.62 ±0.03	0.133*	0.38 ±0.04	1.09 ±0.29
W13	0.13 ±0.01	0.133*	0.87 ±0.04	2.10 ±0.18

* k_{3F} was fixed at 0.133 μs^{-1} (the value obtained from the control maquette).
\# The amplitudes have been scaled so that $[\,^3F^*\,]_A + [\,^3F^*\,]_B = 1$.

Note that $[\,^3F^*\,]_A$ and $[\,^3F^*\,]_B$ represent estimates of the ^{3}F* contribution at t = 0 assuming instantaneous formation of ^{3}F*, while the c_{3F} time profiles presented in Figure 4-17 have been normalized with respect to the c_{3F} at 0.25 μs PPD time.

The rate constants k_{ET} follow the expected trend: k_{ET} is largest for W13 (2.10 ±0.18 μs^{-1}) in which the flavin-Trp distance is smallest and smallest in W20 (0.171 ±0.054 μs^{-1}), for which the flavin-Trp distance is largest.

The rate constant k_{ET} for W20 is in good agreement with the estimated rate constant based on the Moser-Dutton ruler. The measured rate constant in W20 suggests an edge-to-edge distance of 15.9 Å according to the Moser-Dutton ruler. In W16 and W13 the measured rate constants are significantly smaller than expected. This reflects both the flexibility in the flavomaquette structure and the bias of the experiment towards long-lived species due to the inacessibility of Δ*A* data at PPD times earlier than 0.25 μs.

Due to the limited time resolution of the CRDS experiment, no data points earlier than 0.25 μs PPD time are included in the kinetic analysis. Consequently, the experiment is blind to short-lived species *i.e.* RPs formed between flavin and Trp at short donor-acceptor distances. It is clear from the shape of the decay trace of W13 in Figure 4-17 that a significant fraction of the ^{3}F* is lost before the first data point is recorded. This has important implications regarding the interpretation of k_{ET} in W13 since a considerable fraction of the ^{3}F* is reduced by Trp on a timescale inaccessible to the performed experiment. The observed rate constant is therefore interpreted as the rate constant describing the ET of a subset of maquettes, while it cannot be excluded that a fraction of W13 maquettes is undergoing ET at a much faster rate, which could not be time resolved. This hypothesis is supported by the estimate for the rate constant of charge recombination based on the Moser-Dutton ruler, single pass TA experiments with picosecond time resolution performed by Jarocha *et al.* (unpublished data), and time-correlated single photon counting measurements[42].

In both W20 and W13 less than 30% of the initial concentration is attributed to the inactive state, *i.e.* decaying with the rate constant k_{3F}, while the majority (~70% and ~90% respectively) is associated with the active state and a faster decay constant reflecting the reduction of ^{3}F* through ET from Trp. In W16 the majority (62%) of the contribution of ^{3}F* is associated with the decay rate constant of k_{3F} while only 38% decays with the rate constant $k_2 = k_{\mathrm{3F}} + k_{\mathrm{ET}}$. This suggests that in W16 a relatively large fraction is redox inactive, which is surprising given the intermediate β-carbon distance in W16.

<u>Neutral FH$^\bullet$ radical</u>

In Figure 4-18 the c_{FH} for W20 (blue), W16 (green), W13 (red), and the control (black) is plotted as a function of PPD time. For better comparison the intensities are scaled relative to the c_{3F} measured at 0.25 μs PPD time analogous to the data presented in Figure 4-17.

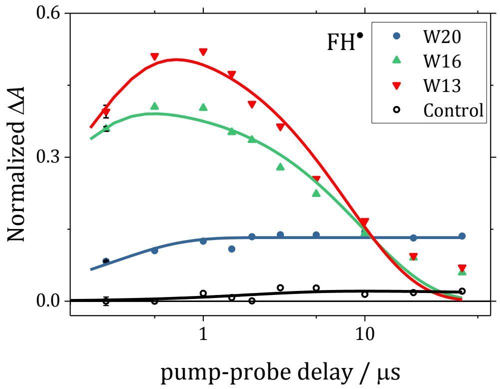

Figure 4-18: Time-profiles of FH• from W20 (blue), W16 (green), W13 (red), and the control (black) estimated by global target analysis described in Section 2.2 and the beginning of this section. All signals are scaled relative to the amplitude of $^3F^*$ measured at 0.25 μs. The error bars shown at 0.5 μs show the estimated standard deviations and are representative of the uncertainty at all PPD times. The solid lines represent exponential fits (see text for more details).

In all three Trp containing maquettes a significant fraction of FH• is already formed after 0.25 μs when the first measurement is made. This is evidence for formation of FH• and therefore ET and protonation of $F^{\bullet-}$ on a timescale faster than the time resolution of the performed experiment.

The time dependence of FH• is more complex than that of $^3F^*$ discussed in the previous section since on the observed time scale both its formation and decay have to be considered. The solid lines in Figure 4-18 show fits of the FH• time-profiles to a simplified version of Scheme 1 including ^1F, $^3F^*$, $F^{\bullet-}$, and FH• and irreversible first-order reaction kinetics. Although the agreement is satisfactory for PPD times less than 10 μs, the model is unable to account for the W13 and W16 data at the later times. The overall inherently complex time dependence of the FH• concentration and the observed multiphasic decrease in c_{FH}, prohibits a straightforward quantitative comparison, but it is obvious from closer inspection of c_{FH} that the FH• concentration exhibits a multiphasic decay, with more than half of the FH• reacting on a 1–5 μs timescale and the rest having a lifetime longer than 10 μs. Observing similar lifetimes of FH• in W13 and W16 is not too surprising given similar magnitudes of k_{ET} (~2.1 μs^{-1} and ~1.1 μs^{-1} respectively).

In W20, by contrast, the FH• concentration plateaus at around 3 μs and remains constant for the next 40 μs. This qualitatively different evolution reflects a significantly different rate of charge recombination in W20 compared to both W16 and W13. This is consistent with the qualitatively different k_{ET} observed in W20 (~0.17 μs^{-1}).

Comparing the c_{FH} at PPD times between 0.25 μs and 10 μs of the three Trp-maquettes, it is clear that the relative yield of FH$^{\bullet}$ decreases markedly with increasing F-W distance. This is as expected, given the more efficient competition of ET with other processes at closer donor-acceptor distances. However, note that the concentration of FH$^{\bullet}$ at PPD times larger than 20 μs is higher in W20 than in W16 and W13, which reflects the longer lifetime of FH$^{\bullet}$ in W20.

In the *de novo* designed maquette W20 with flavin-Trp distance of ~16 Å, the RP2 lifetime exceeds the time window of the experiment (0.25 μs to 40 μs), while in maquettes with shorter flavin-Trp distances the majority of flavin-Trp RPs have reacted within 10 μs. Such long RP lifetimes as in W20 are also observed in the wild type cryptochromes with similar RP separations (*c.f.* results of Section 3.2.1). The control over the lifetime of the RP by tuning the donor-acceptor distance and the similarity achieved between W20 and natural cryptochromes in that regard, demonstrates the potential of the maquettes as a model system for cryptochromes.

Also visible in Figure 4-18, for the control maquette, is a slowly formed signal from a small amount of a neutral flavin radical arising from a photo-reaction of the isoalloxazine ring and the ribityl chain of the riboflavin consistent with the results presented in Section 4.1.1.[26, 103-104]

4.4 Dependency of MFEs in flavoproteins on the donor-acceptor distance

In Section 4.3 it was shown that the proposed photoreaction cycle shown in Figure 4-11 is appropriate for W20, W16, and W13, and that the rate at which ET and charge recombination occur in the maquettes strongly depends on the flavin-Trp separation. As explained in Section 1.4, the manifestation and lifetime of MFEs depend decisively on the relative rates of spin relaxation, spin-selective charge recombination, and formation of

RP2. It therefore does not come as a surprise that the MFE exhibits a pronounced dependency on the donor-acceptor distance.

In this section, the effects of magnetic fields on the photochemistry of the three Trp containing maquettes W20, W16, and W13 are investigated.[x] In the first subsection the time and wavelength dependence of the MFE is investigated to identify the transient species whose concentration is sensitive to magnetic fields. In the second subsection the MFE is analysed as a function of B which sheds light on spin dynamic processes taking place in the SC RP.

4.4.1 MFEs as a function of wavelength and time

The $\Delta\Delta A$ spectra recorded at various PPD times for W20, W16, and W13 are shown in Figure 4-19A, B, and C respectively. The $\Delta\Delta A$ data for W16 and W13 reveal large MFEs, while the $\Delta\Delta A$ observed in W20 is negligible for most PPD times. For that reason, the MFE of W13 and W16 will be compared first and then the results for W20 will be discussed separately in the following section. For better comparability between all three maquettes, the data of W20 is already included in the figures presented in the section on W16 and W13 and repeated in the subsequent subsection.

W16 and W13

The $\Delta\Delta A$ measured in W16 and W13, see Figure 4-19, show a positive MFE between 510 nm and 650 nm, with spectral features that match the absorption spectra of flavin and tryptophan radicals (*c.f.* Figure 4-14), and a negative MFE at wavelengths shorter than 510 nm. The sign change between 500 nm and 510 nm matches the onset of the ground-state absorption (see Figure 2-9B), and can be readily rationalized by considering that an increase in the concentration of transient flavin species upon application of a magnetic field is accompanied by a decrease in the concentration of the flavin ground state.

---

[x] The MFE is measured as the absolute subtraction $\Delta\Delta A = \Delta A(B) - \Delta A(B\text{=}0)$ or as percentage MFE, $\%MFE = \Delta\Delta A/\Delta A(B\text{=}0)$. See Section 2.3 for more details.

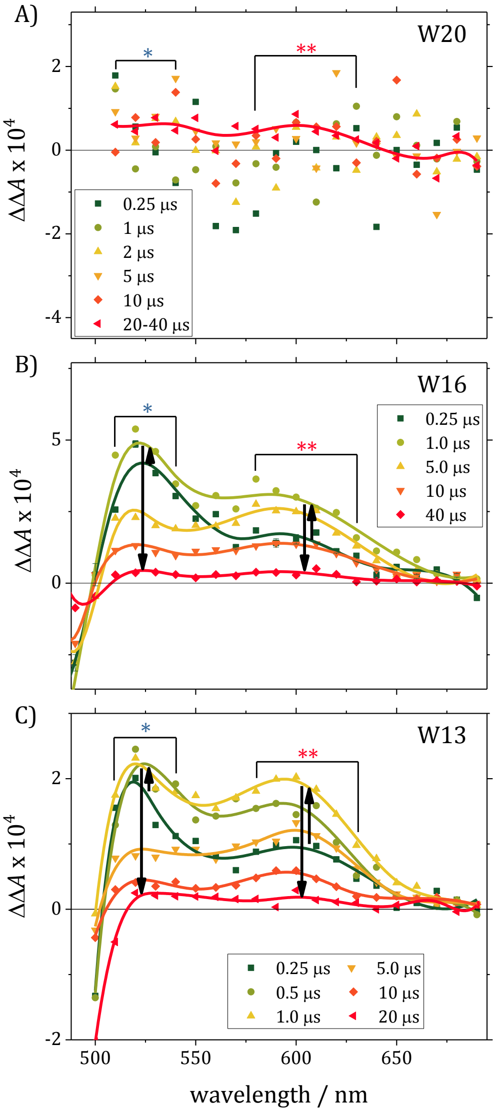

Figure 4-19: A), B), and C) the $\Delta\Delta A = \Delta A(B{=}30\ \mathrm{mT}) - \Delta A(0\ \mathrm{mT})$ spectra of W20, W16, and W13 respectively recorded under standard conditions (see Table 2-1) as a function of PPD delay time. The wavelength regions 510 nm to 540 nm and 580 nm to 630 nm are marked with * and ** respectively. Solid lines are spline fits to guide the eye. Red triangles and the solid line in A) represent the average of the $\Delta\Delta A$ recorded at 20 µs and 40 µs and the spline fit to that average to guide the eye, respectively.

It is important to note that the sign of the MFE is opposite to the MFE observed in cryptochromes. In cryptochromes, ET on a picosecond timescale between $^1F^*$ and $\mathrm{Trp_A}$ outcompetes ISC and leads to an S-born RP. Application of a magnetic field may lead to a reduction in the S-T interconversion efficiency and consequently to negative MFEs via the hyperfine mechanism. As explained in more detail in Sections 1.3 and 1.4, an opposite effect is expected for T-born SC RP. Hence the observed sign of the MFE provides evidence for the proposed formation of T-born SC RPs in the maquettes.

For both W16 and W13, no significant $\Delta\Delta A$ signal is observed between 670 nm and 690 nm, where the transient absorption is dominated by $^3F^*$, despite the detection of a large ΔA signal in that wavelength region (*c.f.* Figure 4-12). In contrast to the ΔA spectra where all absorbing species contribute to the overall absorbance, only species whose concentration depends on B contribute to the $\Delta\Delta A$ spectra.

The spectral shapes of the $\Delta\Delta A$ signals and their evolutions with time are similar in W13 and W16. The relative $\Delta\Delta A$ signal intensity shifts from being strongest at 520 nm at early PPD times (green) to being strongest at 600 nm at later PPD times (orange to red). This shift in relative intensities is consistent with the proposed reaction schemes and reflects the formation of $FH^\bullet$ from $F^{\bullet-}$. For better comparison of the evolution of the $\Delta\Delta A$ at those wavelengths, the normalized average of the $\Delta\Delta A$ measured between 510 nm and 540 nm (blue) and between 580 nm and 630 nm (red) is plotted as a function of PPD time in Figure 4-20.

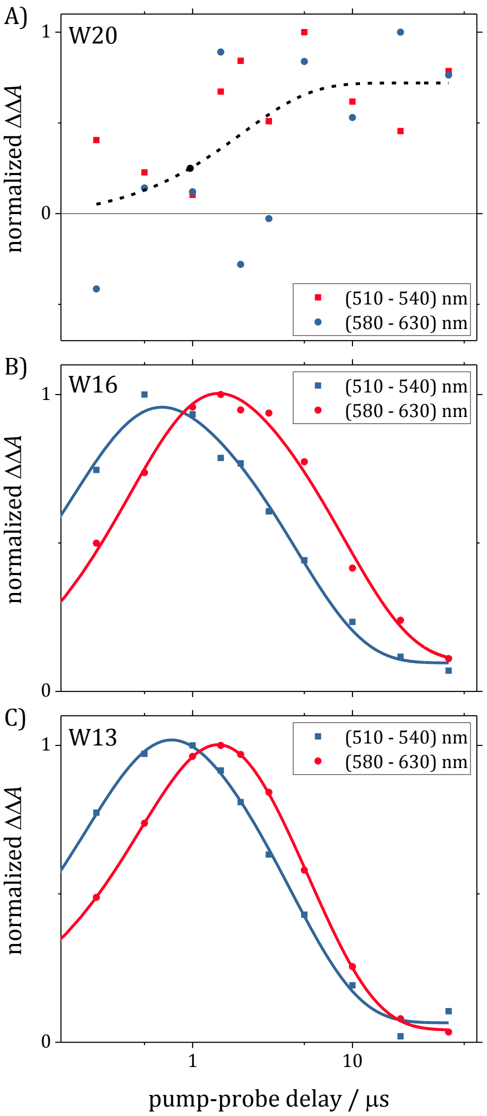

Figure 4-20: A), B), and C) average of the $\Delta\Delta A$ = $\Delta A(B$=30 mT) − ΔA(0 mT) recorded under standard conditions (see Table 2-1) between 510 nm to 540 nm (blue) and 580 nm to 630 nm (red) of W20, W16, and W13 as a function of PPD delay time. Solid lines are biphasic exponential fits to guide the eye. The dashed line in A) is a single exponential fit to the average of the $\Delta\Delta A$(510 nm - 540 nm) and $\Delta\Delta A$(580 nm - 630 nm) to guide the eye.

It is obvious from this presentation that the $\Delta\Delta A$(510 nm – 540 nm) signal passes through a maximum earlier than the $\Delta\Delta A$(580 nm – 630 nm) and that the $\Delta\Delta A$(580 nm – 630 nm) persists for longer. These are important observations for two reasons:

A) This provides further evidence for the assignment of the spectral features in the global analysis presented in Section 4.3.2, especially that at 600 nm. Since both $WH^{\bullet+}$ and $FH^{\bullet}$ exhibit an absorption band with a maximum at around 600 nm of similar shape, an assignment to either species would be justifiable solely based on that consideration. But the fact that a faster decrease in $\Delta\Delta A$ signal in the region where $F^{\bullet-}$ and $W^{\bullet}$ absorb (~510 nm) and a later maximum in the $\Delta\Delta A$ signal in the region where $WH^{\bullet+}$ and $FH^{\bullet}$ absorb can readily be rationalized by the protonation process of initially formed $F^{\bullet-}$. On the other hand, a deprotonation reaction of the initially formed $WH^{\bullet+}$ would lead to the exact opposite trend, *i.e.* a faster decay at 600 nm and a more persistent $\Delta\Delta A$ signal at 510 nm.

B) This provides strong evidence for the hypothesis that the MFE is passed on from the magnetically sensitive RP1 to RP2 which inherits the MFE. This is important since, as described in more detail in Section 1.4, there is an inherent limitation on the lifetime of the magnetically sensitive species, due to the necessity of efficient competition between the spin selective charge recombination and spin decoherence processes. Since under continuous illumination, as is likely the case in a natural environment where the sun or the stars would act as light sources, the lifetime of transient species is decisive for its concentration levels in equilibrium. It has been suggested that in natural cryptochromes this restriction on the lifetime of the magnetically sensitive species is circumvented by passing on the MFE to a longer lived transient species (RP2) which is not immediately sensitive to magnetic fields but inherits the MFE from a magnetically sensitive precursor. This “storage effect” of the MFE is therefore potentially a crucial feature of natural cryptochromes to act as magneto sensor and has been observed in cryptochromes *in vitro* in previous and this work (see Section 3.2.1).[15]

Despite the general similarities of the $\Delta\Delta A$ observed in W16 and W13, the effect of different flavin-Trp distances on the lifetime of the RP2 is also reflected in the time dependence of the $\Delta\Delta A$. In W16, 80% of the maximum magnitude of $\Delta\Delta A$(580 nm – 630 nm) is still observed after 5 µs and 24% after 10 µs, while in W13 only 60% is observed after 5 µs and only 8% after 10 µs. This is consistent with the expected trend of a shorter lifetime of the RP2 with shorter donor-acceptor distance.

In addition to the difference in the lifetime of the MFE, an effect of the difference in the flavin-Trp distance on the magnitude of the $\Delta\Delta A$ and %*MFE* is observed. In Figure 4-21 the

$\Delta\Delta A$ and $\%MFE$ averaged between 510 nm and 620 nm are shown for the three Trp containing maquettes. The $\Delta\Delta A$ in W16 is almost twice as large as the $\Delta\Delta A$ in W13, although the $\%MFE$ is larger in W13. The relatively small $\Delta\Delta A$ despite large $\%MFE$ in W13 is likely the consequence of an overall relatively low concentration of radicals and consistent with the hypothesis that a significant fraction of RP has undergone charge recombination before 0.25 µs.

Both W16 and W13 exhibit a significant $\Delta\Delta A$ already at 0.25 µs which increases up to 1 µs before decaying largely within 10 µs. As expected, the evolution of the ΔΔA is similar to that of $FH^{\bullet}$ (c.f. Figure 4-18). The relatively small decrease in $\Delta\Delta A$ between 20 µs and 40 µs after a decrease by ~60% between 2 µs and 10 µs is consistent with the observation of a long-lived ΔA component attributed to a subset of maquette conformers with comparatively large flavin-Trp separation.

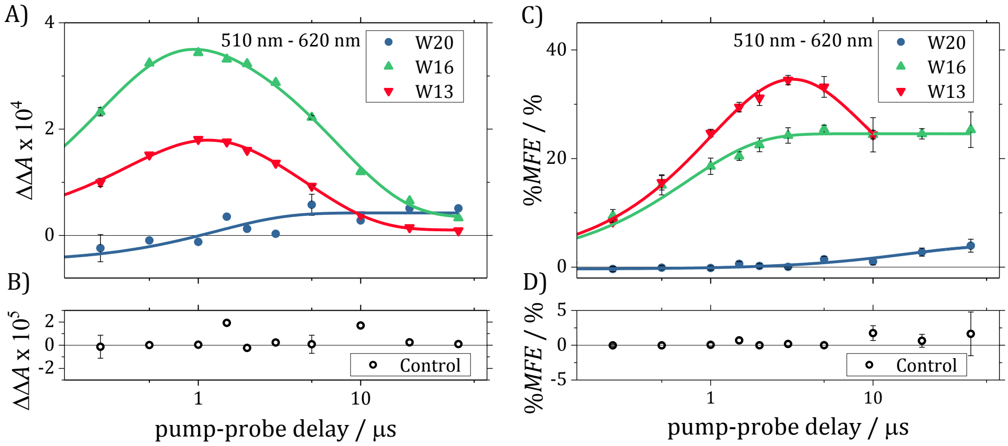

Figure 4-21: Average MFE, recorded as a function of PPD delay time under standard conditions (see Table 2-1) between 510 nm to 620 nm and expressed as $\Delta\Delta A = \Delta A(B\text{=}30\ \mathrm{mT}) - \Delta A(0\ \mathrm{mT})$ in A) for W20, W16, W13 and B) for the control; and as $\%MFE$ in C) and D). Solid lines are biphasic exponential fits to guide the eye.

The time dependence of $\%MFE$ is both a function of the $\Delta\Delta A$ and the ΔA, and therefore includes the differetial absorbance of non-magnetically sensitive species such as $^3F^*$. The large $\%MFE$ in W13 (35%) is the result of both very efficient competition between charge recombination and spin decoherence as well as a relatively low $^3F^*$ concentration.

W20

In W20 a much weaker MFE is observed compared to W13 and W16. Most $\Delta\Delta A$ data points are scattered around zero (see Figure 4-19A and repeated below in Figure 4-22A) and only at late PPD times, illustrated as red triangles, a small MFE is observed. An average of the $\Delta\Delta A$ measured at 20 µs and 40 µs is shown in Figure 4-22A. Likewise, the average $\Delta\Delta A$ measured between 510 nm and 540 nm and between 580 nm and 630 nm is shown below in Figure 4-22B as well as in Figure 4-20A to facilitate easy comparison between all three maquettes.

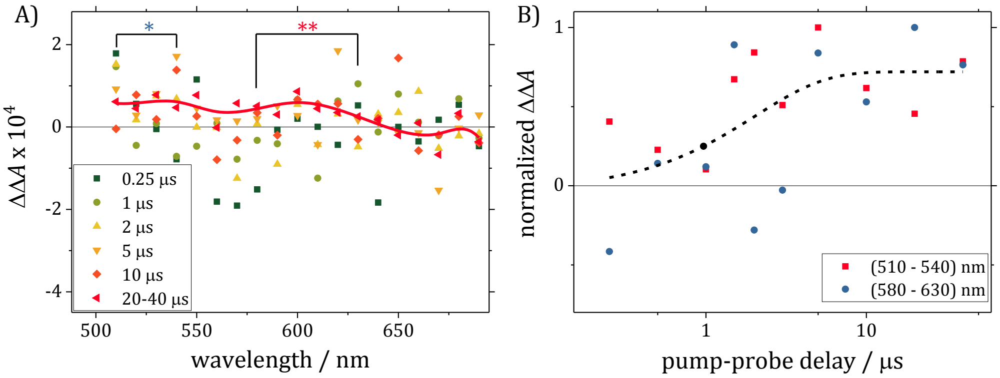

Figure 4-22: A) the $\Delta\Delta A = \Delta A(B{=}30\text{ mT}) - \Delta A(0\text{ mT})$ spectra of W20 recorded under standard conditions (see Table 2-1) as a function of PPD delay time. The wavelength regions 510 nm to 540 nm and 580 nm to 630 nm are marked with * and ** respectively. Red triangles and the solid line in A) represent the average of the $\Delta\Delta A$ recorded at 20 µs and 40 µs and the spline fit to that average to guide the eye. B) average of the $\Delta\Delta A$ between 510 nm to 540 nm (blue) and 580 nm to 630 nm (red) of W20. The dashed line is a single exponential fit to the average of the $\Delta\Delta A$(510 nm - 540 nm) and $\Delta\Delta A$(580 nm - 630 nm) to guide the eye.

The $\Delta\Delta A$ action signal is negligible at all PPD times between 640 nm and 690 nm, and is only positive at late PPD times between 510 nm and 630 nm. The %*MFE* averaged between 510 nm and 620 nm after 40 µs PPD time is (4 ±1)% (see Figure 4-21). These results are consistent with the results from Section 4.3, where strong evidence for the formation of a flavin-Trp RP with a lifetime exceeding the timeframe of the experiment is presented.

Although W20 clearly exhibits the smallest $\Delta\Delta A$ signal between 0.25 µs and 20 µs of all Trp containing maquettes, it plateaus between 5 µs and 40 µs, while both the $\Delta\Delta A$ signals of

W16 and W13 decrease significantly in that timeframe. Note that as a result, the $\Delta\Delta A$ in W20 is largest at 40 µs PPD time, as can be seen in Figure 4-21A.

The results of this section demonstrate that the maquette framework facilitates the investigation of MFEs of flavin-Trp based RPs observed in Cry. This includes both

- large and short-lived MFEs, similar to those observed in the *Dm*Cry W394F and *Er*Cry W369F mutants with shortened Trp ET chain, by using maquette structures with relatively short flavin Trp distances.
- small and long-lived MFEs, similar to those observed in the cryptochromes with intact ET chain such as *Dm*Cry WT and *Er*Cry WT, by using maquette structures with relatively large flavin Trp distances (*c.f.* Chapter 3).

4.4.2 MFEs as a function of magnetic field

The magnetically altered reaction yield (MARY) as a function of B is shown in Figure 4-23 for W20, W16, and W13. The MARY profiles show the $\%MFE$ measured at 600 nm and 0.5 µs PPD time. The $\%MFE$ in W13 and W16 are of comparable magnitude and significantly larger than in W20. This is consistent with the results of the independently measured $\%MFE$ data shown in Figure 4-21. The magnetic field strength, $B_{1/2}$, at which the $\%MFE$ reaches half of its maximum magnitude, is characteristic of the magnetically sensitive RP depending both on intramolecular properties such as hyperfine couplings and the RP environment.[29] Lorentzian fits to the MARY profiles shown in Figure 4-23 yield $B_{1/2}$ values of 14.4 ±0.7 mT (W13), 13.6 ±0.4 mT (W16), and 16.3 ±5.4 mT (W20).

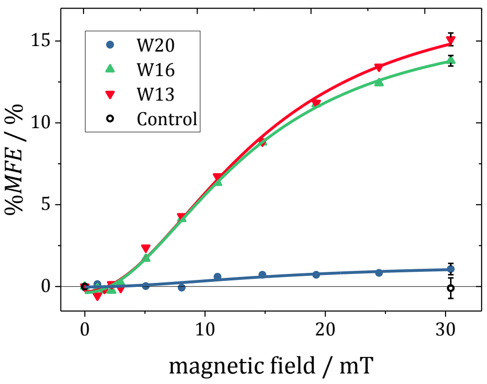

Figure 4-23: MARY spectra for W20 (blue), W16 (green), W13 (red), and the control (black) measured under standard conditions (see Table 2-1) at 600 nm and 0.5 μs PPD time. Representative error bars are shown at B = 30 mT and illustrate one SEM. Lorentzian fits are shown as solid lines from which $B_{1/2}$ values of 14.4 ±0.7 mT (W13), 13.6 ±0.4 mT (W16), and 16.3 ±5.4 mT (W20) are derived.

The similarity of the $B_{1/2}$ values is consistent with the fact that the same magnetically sensitive RP is formed in all three Trp containing maquettes, respectively- but nonetheless surprising as electron spin interactions may play in important role in the broadening of MARY spectra and depend on the RP separation.

The radical pair partners are very similar in all cases and consequently the respective hyperfine interaction constants are similar in the respective SC RP. Therefore, it wouldn't in general be surprising if the $B_{1/2}$ values for such RP turned out to be similar. But the estimate for the $B_{1/2}$ solely based on the hyperfine interactions, *e.g.* by using the Weller formula, underestimates the $B_{1/2}$ significantly. Based on the Weller formula, the $B_{1/2}$ of a flavin-Trp radical pair has been estimated by Maeda *et al.* to be 3 mT and therefore significantly smaller than the $B_{1/2}$ value of the flavomaquettes reported here.[15, 73] It has been shown previously and in this work, that under some circumstances, such as in a protein environment or in aqueous solutions with increased viscosity, the $B_{1/2}$ of a flavin/Trp based radical pair can greatly exceed the Weller estimate.[15, 29]

The broadening of the MARY spectra is interpreted as the result of spin-relaxation which is driven by the modulation of the interaction of the spin with its environment. Although the hyperfine interaction of the electron spin with the flavin and Trp nuclei are expected to be very similar, other interactions, such as the exchange and dipolar interaction, are dependent on the RP separation and are therefore different in W20, W16, and W13. It is not straightforward to deduce which spin-relaxation mechanism is dominant from the available data, and a coincidental similarity of $B_{1/2}$ values, despite the obvious differences of the RP formed in W20, W16, and W13, cannot be excluded.

For MFEs to manifest themselves through the hyperfine mechanism, the unpaired electron spins of the magnetically sensitive RP must not experience dipolar or exchange interactions strong enough to inhibit hyperfine driven singlet-triplet mixing. Both dipolar and exchange interaction are large at short RP separations but decrease with RP separation (see Section 1.3.3). The employed technique is sensitive only to transient species with a sufficiently long lifetime and consequently selective to RPs formed at longer donor-acceptor distance. The data presented in this work suggests that the observed RPs are formed at flavin-Trp separations significantly larger than the proposed β-carbon distance, which explains the observation of MFEs even in W13.

4.5 Conclusions

In this chapter, the photophysical processes in the first artificial protein magnetic sensor are presented and characterized. These represent model system for the cryptochromes, the magnetic sensitivity of which is thought to lie at the heart of the magnetoreception of some animals. The Trp containing maquettes exhibit a photochemistry analogous to their natural counterparts, where, upon photoexcitation a SC flavin-Trp RP [$F^{\bullet-}$ $WH^{\bullet+}$] is formed.

Using global target analysis of the control maquette ΔA data, the lifetime of $^3F^*$ in the absence of a redox active amino acid is determined to be ~7.5 μs. In the presence of Trp or His, the lifetime is significantly reduced and RP formation is observed. In order to investigate the dependency of the photochemistry and MFEs of flavoproteins on the intramolecular flavin-Trp separation, a series of three maquettes with different flavin-Trp distances was investigated. The distances between the attachment site of the flavin and the β-carbon of the Trp range from 5.6 Å in W13 to 16.8 Å in W20, and the expected trend of decreasing ET rate constants with increasing flavin-Trp is observed.

As in the Cry, the flavin and Trp RP partners were identified as the magnetically sensitive species, while no effects of magnetic fields on the concentration of $^3F^*$ was detected.

The maquette model systems reproduce two important aspects of Cry photochemistry: A) the formation of magnetically sensitive flavin-Trp RP1 and B) the formation of a RP2 through (de-)protonation, which inherits the MFE and has the potential to “store” it. The latter is most obvious in W20 where, analogous to the *Er*Cry4 WT, a RP is observed which exhibits magnetic sensitivity and a lifetime exceeding 40 μs.

As well as marked similarities to the Cry photochemistry, some significant differences in the behaviour of maquettes have been observed. The most striking difference is the opposite sign of the MFE observed in maquettes and Crys, which reflects the triplet/singlet-nature of the SC RP formed in maquettes/Cry. The second is the substantial dynamic heterogeneity, attributed to the less rigid structure and binding of the flavin chromophore of the maquette and hence the presence of multiple maquette conformers with various flavin-Trp distances.

In the Trp containing maquettes the observed ET rates could be rationalized by considering two general categories of conformations: A) where ET is fast, i.e. RP formation competes efficiently with other quenching processes of $^3F^*$ and B) where ET is slow $k_{ET} \ll k_{3F}$. The rate constant of ET in W20 (0.17 ±0.05 μs^{-1}) matches the predicted rate constant based on the Moser-Dutton ruler, while the measured ET rate constants in W16 and W13 are significantly smaller than expected.

Solely considering the edge-to-edge distance, driving force, and reorganization energy, ET and BET in W13 are estimated to take place well before 0.25 µs. The fact that, nonetheless, flavin-Trp RPs are observed on the timescale of the experiment (0.25 µs to 40 µs) is evidence for the structural flexibility and the presence of maquette conformers with edge-to-edge distances significantly larger than the β-carbon distance of the flavin attachment site and the Trp.

The $B_{1/2}$ values of W20, W16, and W13 are similar to one another (~14 mT) and much larger than the $B_{1/2}$ estimated for flavin-Trp RPs through the Weller formula based on the relevant hyperfine interactions (~3 mT). Similar $B_{1/2}$ values have been observed in protein based flavin-Trp RP and attributed to spin relaxation driven by modulation of the electron exchange interaction.[15] The similarity of $B_{1/2}$ values of W20, W16, and W13 is surprising given the obvious differences in the RP separation. The similarity could be an indication that it is the modulation of the anisotropic hyperfine interactions, rather than the exchange interaction.

Finally, maquettes containing more than one Trp are of great interest and recently made available to us by Dutton *et al.* These maquette systems exhibit an ET chain comprised of two or three Trps and constitute a vital and promising step towards modelling the ET chain in Cry more closely.

Appendix

A1 Amino acid sequences: Control

The amino acid sequence of the control is shown below, starting from the N terminus. The cysteine (**C**) at position 9 on Helix 2, used to attach the RF chromophore, is highlighted orange:[42]

Helix 1	GEIQKQFEDALQKFEEALNQFEDLKQL
Loop	GGSGSGSGG
Helix 2	EIQKQFEDCLQKFEEALNQFEDLKQL
Loop	GGSGSGSGG
Helix 3	EIQKQFEDALQKFEEALNQFEDLKQL
Loop	GGSGSGSGG
Helix 4	EIQKQFEDALQKFEEALNQFEDLKQL

A2 Amino acid sequences: H6, W13, W16, and W20

The amino acid sequence of the H6, W13, W16, and W20 is shown below, starting from the N terminus. The cysteine (**C**) at position 9 on Helix 2, used to attach the RF chromophore, is highlighted orange. The amino acids **F**, **F**, **A**, and **F** at positions 6, 13, 16, and 20, highlighted (purple, red, green, and blue), are replaced by the amino acid H or W in the maquettes H6, W13, W16, and W20:[42]

Helix 1	EIQKQFEDALQKFEEALNQFEDLKQL
Loop	GGSGSGSGG
Helix 2	EIQKQFEDCLQKFEEALNQFEDLKQL
Loop	GGSGSGSGG
Helix 3	EIQKQFEDALQKFEEALNQFEDLKQL
Loop	GGSGSGSGG
Helix 4	EIQKQFEDALQKFEEALNQFEDLKQL

Bibliography

1. Wiltschko, W.; Wiltschko, R., Magnetic Versus Celestial Orientation in Migrating Birds. *Trends in Ecology & Evolution* **1988,** *3* (1), 13-15.

2. Wiltschko, W.; Wiltschko, R., Magnetic orientation and magnetoreception in birds and other animals. *Journal of Comparative Physiology a-Neuroethology Sensory Neural and Behavioral Physiology* **2005,** *191* (8), 675-693.

3. Quinn, T. P.; Merrill, R. T.; Brannon, E. L., Magnetic-Field Detection in Sockeye Salmon. *Journal of Experimental Zoology* **1981,** *217* (1), 137-142.

4. Phillips, J. B., 2 Magnetoreception Pathways in a Migratory Salamander. *Science* **1986,** *233* (4765), 765-767.

5. Gegear, R. J.; Casselman, A.; Waddell, S.; Reppert, S. M., Cryptochrome mediates light-dependent magnetosensitivity in Drosophila. *Nature* **2008,** *454* (7207), 1014-U61.

6. Schulten, K.; Swenberg, C. E.; Weller, A., Biomagnetic Sensory Mechanism Based on Magnetic-Field Modulated Coherent Electron-Spin Motion. *Zeitschrift Fur Physikalische Chemie-Frankfurt* **1978,** *111* (1), 1-5.

7. Hore, P. J.; Mouritsen, H., The Radical-Pair Mechanism of Magnetoreception. *Annual Review of Biophysics, Vol 45* **2016,** *45*, 299-344.

8. Weber, S.; Schleicher, E., Flavins and Flavoproteins Methods and Protocols Preface. *Flavins and Flavoproteins: Methods and Protocols* **2014,** *1146*, Vii-Viii.

9. Macheroux, P.; Kappes, B.; Ealick, S. E., Flavogenomics - a genomic and structural view of flavin-dependent proteins. *Febs Journal* **2011,** *278* (15), 2625-2634.

10. Chaves, I.; Pokorny, R.; Byrdin, M.; Hoang, N.; Ritz, T.; Brettel, K.; Essen, L. O.; van der Horst, G. T. J.; Batschauer, A.; Ahmad, M., The Cryptochromes: Blue Light Photoreceptors in Plants and Animals. *Annual Review of Plant Biology, Vol 62* **2011,** *62*, 335-364.

11. van der Horst, G. T. J.; Muijtjens, M.; Kobayashi, K.; Takano, R.; Kanno, S.; Takao, M.; de Wit, J.; Verkerk, A.; Eker, A. P. M.; van Leenen, D.; Buijs, R.; Bootsma, D.; Hoeijmakers, J. H. J.; Yasui, A., Mammalian Cry1 and Cry2 are essential for maintenance of circadian rhythms. *Nature* **1999,** *398* (6728), 627-630.

12. Ritz, T.; Adem, S.; Schulten, K., A model for photoreceptor-based magnetoreception in birds. *Biophysical Journal* **2000,** *78* (2), 707-718.

13. Moller, A.; Sagasser, S.; Wiltschko, W.; Schierwater, B., Retinal cryptochrome in a migratory passerine bird: a possible transducer for the avian magnetic compass. *Naturwissenschaften* **2004,** *91* (12), 585-588.

14. Maeda, K.; Henbest, K. B.; Cintolesi, F.; Kuprov, I.; Rodgers, C. T.; Liddell, P. A.; Gust, D.; Timmel, C. R.; Hore, P. J., Chemical compass model of avian magnetoreception. *Nature* **2008,** *453* (7193), 387-U38.

15. Maeda, K.; Robinson, A. J.; Henbest, K. B.; Hogben, H. J.; Biskup, T.; Ahmad, M.; Schleicher, E.; Weber, S.; Timmel, C. R.; Hore, P. J., Magnetically sensitive light-induced reactions in cryptochrome are consistent with its proposed role as a magnetoreceptor. *Proceedings of the National Academy of Sciences of the United States of America* **2012,** *109* (13), 4774-4779.

16. Heyers, D.; Manns, M.; Luksch, H.; Gunturkun, O.; Mouritsen, H., A Visual Pathway Links Brain Structures Active during Magnetic Compass Orientation in Migratory Birds. *Plos One* **2007,** *2* (9).

17. Mouritsen, H.; Janssen-Bienhold, U.; Liedvogel, M.; Feenders, G.; Stalleicken, J.; Dirks, P.; Weiler, R., Cryptochromes and neuronal-activity markers colocalize in the retina of

migratory birds during magnetic orientation. *Proceedings of the National Academy of Sciences of the United States of America* **2004,** *101* (39), 14294-14299.

18. Wiltschko, W.; Munro, U.; Ford, H.; Wiltschko, R., Red-Light Disrupts Magnetic Orientation of Migratory Birds. *Nature* **1993,** *364* (6437), 525-527.

19. Wiltschko, W.; Wiltschko, R., The effect of yellow and blue light on magnetic compass orientation in European robins, Erithacus rubecula. *Journal of Comparative Physiology a-Sensory Neural and Behavioral Physiology* **1999,** *184* (3), 295-299.

20. Gunther, A.; Einwich, A.; Sjulstok, E.; Feederle, R.; Bolte, P.; Koch, K. W.; Solov'yov, I. A.; Mouritsen, H., Double-Cone Localization and Seasonal Expression Pattern Suggest a Role in Magnetoreception for European Robin Cryptochrome 4. *Current Biology* **2018,** *28* (2), 211-223.

21. Schleicher, E.; Weber, S., Radicals in Flavoproteins. *Epr Spectroscopy: Applications in Chemistry and Biology* **2012,** *321*, 41-65.

22. Salzmann, S.; Tatchen, J.; Marian, C. M., The photophysics of flavins: What makes the difference between gas phase and aqueous solution? *Journal of Photochemistry and Photobiology a-Chemistry* **2008,** *198* (2-3), 221-231.

23. Knowles, A.; Mautner, G. N., Flavin-Sensitized Photooxidation of Nucleotides .3. Participation of Oxygen. *Photochemistry and Photobiology* **1972,** *15* (2), 199-207.

24. Tsentalovich, Y. P.; Lopez, J. J.; Hore, P. J.; Sagdeev, R. Z., Mechanisms of reactions of flavin mononucleotide triplet with aromatic amino acids. *Spectrochimica Acta Part a-Molecular and Biomolecular Spectroscopy* **2002,** *58* (9), 2043-2050.

25. Kao, Y. T.; Tan, C.; Song, S. H.; Ozturk, N.; Li, J.; Wang, L. J.; Sancar, A.; Zhong, D. P., Ultrafast dynamics and anionic active states of the flavin cofactor in cryptochrome and photolyase. *Journal of the American Chemical Society* **2008,** *130* (24), 7695-7701.

26. Li, G. F.; Glusac, K. D., Light-triggered proton and electron transfer in flavin cofactors. *Journal of Physical Chemistry A* **2008,** *112* (20), 4573-4583.

27. Moore, W. M.; Mcdaniels, J. C.; Hen, J. A., Photochemistry of Riboflavin .6. Photophysical Properties of Isoalloxazines. *Photochemistry and Photobiology* **1977,** *25* (6), 505-512.

28. Kennis, J. T. M.; Crosson, S.; Gauden, M.; van Stokkum, I. H. M.; Moffat, K.; van Grondelle, R., Primary reactions of the LOV2 domain of phototropin, a plant blue-light photoreceptor. *Biochemistry* **2003,** *42* (12), 3385-3392.

29. Evans, E. W.; Li, J.; Storey, J. G.; Maeda, K.; Henbest, K. B.; Hore, P. J.; Mackenzie, S. R.; Timmel, C., Sensitive fluorescence-based detection of magnetic field effects in photoreactions of flavins. *Phys. Chem. Chem. Phys.* **2015**.

30. Jones, M. L.; Kurnikov, I. V.; Beratan, D. N., The nature of tunneling pathway and a verage packing density models for protein-mediated electron transfer. *Journal of Physical Chemistry A* **2002,** *106* (10), 2002-2006.

31. Moser, C. C.; Anderson, J. L. R.; Dutton, P. L., Guidelines for tunneling in enzymes. *Biochimica Et Biophysica Acta-Bioenergetics* **2010,** *1797* (8), 1573-1586.

32. Moser, C. C.; Keske, J. M.; Warncke, K.; Farid, R. S.; Dutton, P. L., Nature of Biological Electron-Transfer. *Nature* **1992,** *355* (6363), 796-802.

33. Edelman, G. M.; Gally, J. A., Degeneracy and complexity in biological systems. *Proceedings of the National Academy of Sciences of the United States of America* **2001,** *98* (24), 13763-13768.

34. Dutton, P. L.; Moser, C. C., Engineering enzymes. *Faraday Discussions* **2011,** *148*, 443-448.

35. Lichtenstein, B. R.; Farid, T. A.; Kodali, G.; Solomon, L. A.; Anderson, J. L.; Sheehan, M. M.; Ennist, N. M.; Fry, B. A.; Chobot, S. E.; Bialas, C.; Mancini, J. A.; Armstrong, C. T.; Zhao, Z.; Esipova, T. V.; Snell, D.; Vinogradov, S. A.; Discher, B. M.; Moser, C. C.; Dutton, P. L., Engineering oxidoreductases: maquette proteins designed from scratch. *Biochem Soc Trans* **2012,** *40* (3), 561-6.

36. Sharp, R. E.; Moser, C. C.; Rabanal, F.; Dutton, P. L., Design, synthesis, and characterization of a photoactivatable flavocytochrome molecular maquette.

Proceedings of the National Academy of Sciences of the United States of America **1998,** *95* (18), 10465-10470.

37. Regan, L.; Degrado, W. F., Characterization of a Helical Protein Designed from 1st Principles. *Science* **1988,** *241* (4868), 976-978.

38. Kodali, G.; Mancini, J. A.; Solomon, L. A.; Episova, T. V.; Roach, N.; Hobbs, C. J.; Wagner, P.; Mass, O. A.; Aravindu, K.; Barnsley, J. E.; Gordon, K. C.; Officer, D. L.; Dutton, P. L.; Moser, C. C., Design and engineering of water-soluble light-harvesting protein maquettes. *Chemical Science* **2017,** *8* (1), 316-324.

39. Goparaju, G.; Fry, B. A.; Chobot, S. E.; Wiedman, G.; Moser, C. C.; Dutton, P. L.; Discher, B. M., First principles design of a core bioenergetic transmembrane electron-transfer protein. *Biochimica Et Biophysica Acta-Bioenergetics* **2016,** *1857* (5), 503-512.

40. Watkins, D. W.; Jenkins, J. M. X.; Grayson, K. J.; Wood, N.; Steventon, J. W.; Le Vay, K. K.; Goodwin, M. I.; Mullen, A. S.; Bailey, H. J.; Crump, M. P.; MacMillan, F.; Mulholland, A. J.; Cameron, G.; Sessions, R. B.; Mann, S.; Anderson, J. L. R., Construction and in vivo assembly of a catalytically proficient and hyperthermostable de novo enzyme. *Nature Communications* **2017,** *8*.

41. Farid, T. A.; Kodali, G.; Solomon, L. A.; Lichtenstein, B. R.; Sheehan, M. M.; Fry, B. A.; Bialas, C.; Ennist, N. M.; Siedlecki, J. A.; Zhao, Z.; Stetz, M. A.; Valentine, K. G.; Anderson, J. L.; Wand, A. J.; Discher, B. M.; Moser, C. C.; Dutton, P. L., Elementary tetrahelical protein design for diverse oxidoreductase functions. *Nature Chemical Biology* **2013,** *9* (12), 826-33.

42. Bialas, C.; Jarocha, L. E.; Henbest, K. B.; Zollitsch, T. M.; Kodali, G.; Timmel, C. R.; Mackenzie, S. R.; Dutton, P. L.; Moser, C. C.; Hore, P. J., Engineering an Artificial Flavoprotein Magnetosensor. *Journal of the American Chemical Society* **2016,** *138* (51), 16584-16587.

43. Woodward, J. R., Radical pairs in solution. *Progress in Reaction Kinetics and Mechanism* **2002,** *27*, 165–207.

44. Steiner, U. E.; Ulrich, T., Magnetic-Field Effects in Chemical-Kinetics and Related Phenomena. *Chemical Reviews* **1989,** *89* (1), 51-147.

45. Schulten, K.; Wolynes, P. G., Semi-Classical Description of Electron-Spin Motion in Radicals Including Effect of Electron Hopping. *Journal of Chemical Physics* **1978,** *68* (7), 3292-3297.

46. Brocklehurst, B., Magnetic fields and radical reactions: recent developments and their role in nature. *Chemical Society Reviews* **2002,** *31* (5), 301-311.

47. Hore, P. J., *Nuclear Magnetic Resonance*. 2 ed.; Oxford University Press: Oxford, 1995.

48. Efimova, O.; Hore, P. J., Role of exchange and dipolar interactions in the radical pair model of the avian magnetic compass. *Biophysical Journal* **2008,** *94* (5), 1565-1574.

49. Brocklehurst, B., Spin Correlation in Geminate Recombination of Radical Ions in Hydrocarbons .1. Theory of Magnetic-Field Effect. *Journal of the Chemical Society-Faraday Transactions Ii* **1976,** *72*, 1869-1884.

50. Timmel, C. R.; Till, U.; Brocklehurst, B.; McLauchlan, K. A.; Hore, P. J., Effects of weak magnetic fields on free radical recombination reactions. *Molecular Physics* **1998,** *95* (1), 71-89.

51. Rodgers, C. T., Magnetic field effects in chemical systems. *Pure and Applied Chemistry* **2009,** *81* (1), 19-43.

52. Kattnig, D. R.; Solov'yov, I. A.; Hore, P. J., Electron spin relaxation in cryptochrome-based magnetoreception. *Physical Chemistry Chemical Physics* **2016,** *18* (18), 12443-12456.

53. Evans, E. W.; Dodson, C. A.; Maeda, K.; Biskup, T.; Wedge, C. J.; Timmel, C. R., Magnetic field effects in flavoproteins and related systems. *Interface Focus* **2013,** *3* (5).

54. Solov'yov, I. A.; Schulten, K., Reaction Kinetics and Mechanism of Magnetic Field Effects in Cryptochrome. *Journal of Physical Chemistry B* **2012,** *116* (3), 1089-1099.

55. Kattnig, D. R.; Evans, E. W.; Déjean, V.; Dodson, C. A.; Wallace, M. I.; Mackenzie, S. R.; Timmel, C. R.; Hore, P. J., Chemical amplification of magnetic field effects relevant to avian magnetoreception. *Nature Chemistry* **2016**.

56. Evans, E. W.; Kattnig, D. R.; Henbest, K. B.; Hore, P. J.; Mackenzie, S. R.; Timmel, C. R., Sub-millitesla magnetic field effects on the recombination reaction of flavin and ascorbic acid radicals. *The Journal of Chemical Physics* **2016,** *145* (8), 085101.

57. Langenbacher, T.; Immeln, D.; Dick, B.; Kottke, T., Microsecond Light-induced Proton Transfer to Flavin in the Blue Light Sensor Plant Cryptochrome. *Journal of the American Chemical Society* **2009,** *131* (40), 14274-14280.

58. Paulus, B.; Bajzath, C.; Melin, F.; Heidinger, L.; Kromm, V.; Herkersdorf, C.; Benz, U.; Mann, L.; Stehle, P.; Hellwig, P.; Weber, S.; Schleicher, E., Spectroscopic characterization of radicals and radical pairs in fruit fly cryptochrome - protonated and nonprotonated flavin radical-states. *FEBS J* **2015**.

59. Sheppard, D. M. W.; Li, J.; Henbest, K. B.; Neil, S. R. T.; Maeda, K.; Storey, J.; Schleicher, E.; Biskup, T.; Rodriguez, R.; Weber, S.; Hore, P. J.; Timmel, C. R.; Mackenzie, S. R., Millitesla magnetic field effects on the photocycle of an animal cryptochrome. *Sci Rep* **2017,** *7*.

60. Maeda, K.; Neil, S. R.; Henbest, K. B.; Weber, S.; Schleicher, E.; Hore, P. J.; Mackenzie, S. R.; Timmel, C. R., Following radical pair reactions in solution: a step change in sensitivity using cavity ring-down detection. *Journal of the American Chemical Society* **2011,** *133* (44), 17807-15.

61. Neil, S. R. T.; Li, J.; Sheppard, D. M. W.; Storey, J.; Maeda, K.; Henbest, K. B.; Hore, P. J.; Timmel, C. R.; Mackenzie, S. R., Broadband Cavity-Enhanced Detection of Magnetic Field Effects in Chemical Models of a Cryptochrome Magnetoreceptor. *Journal of Physical Chemistry B* **2014,** *118* (15), 4177-4184.

62. Henbest, K. B.; Maeda, K.; Hore, P. J.; Joshi, M.; Bacher, A.; Bittl, R.; Weber, S.; Timmel, C. R.; Schleicher, E., Magnetic-field effect on the photoactivation reaction of Escherichia coli DNA photolyase. *Proceedings of the National Academy of Sciences of the United States of America* **2008,** *105* (38), 14395-14399.

63. Okeefe, A.; Deacon, D. A. G., Cavity Ring-down Optical Spectrometer for Absorption-Measurements Using Pulsed Laser Sources. *Review of Scientific Instruments* **1988,** *59* (12), 2544-2551.

64. Ouyang, B.; Jones, R. L., Understanding the sensitivity of cavity-enhanced absorption spectroscopy: pathlength enhancement versus noise suppression. *Applied Physics B-Lasers and Optics* **2012,** *109* (4), 581-591.

65. Brown, S. S.; Ravishankara, A. R.; Stark, H., Simultaneous kinetics and ring-down: Rate coefficients from single cavity loss temporal profiles. *Journal of Physical Chemistry A* **2000,** *104* (30), 7044-7052.

66. Ruckebusch, C.; Sliwa, M.; Pernot, P.; de Juan, A.; Tauler, R., Comprehensive data analysis of femtosecond transient absorption spectra: A review. *Journal of Photochemistry and Photobiology C-Photochemistry Reviews* **2012,** *13* (1), 1-27.

67. vanStokkum, I. H. M., Parameter precision in global analysis of time-resolved spectra. *Ieee Transactions on Instrumentation and Measurement* **1997,** *46* (4), 764-768.

68. Kanski, R.; Murray, C. J., Enzymichromism - Determination of the Dielectric-Properties of an Enzyme Active-Site. *Biophysical Journal* **1993,** *64* (2), A370-A370.

69. Solar, S.; Getoff, N.; Surdhar, P. S.; Armstrong, D. A.; Singh, A., Oxidation of Tryptophan and N-Methylindole by N3., Br2-, and (Scn)2- Radicals in Light-Water and Heavy-Water Solutions - a Pulse-Radiolysis Study. *Journal of Physical Chemistry* **1991,** *95* (9), 3639-3643.

70. Aubert, C.; Mathis, P.; Eker, A. P. M.; Brettel, K., Intraprotein electron transfer between tyrosine and tryptophan in DNA photolyase from Anacystis nidulans. *Proceedings of the National Academy of Sciences of the United States of America* **1999,** *96* (10), 5423-5427.

71. Miller, J. E., Radical formation and electron transfer in biological molecules, *DPhil Thesis*, California Institute of Technology. **2003**.

72. Miller, J. E.; Gradinaru, C.; Crane, B. R.; Di Bilio, A. J.; Wehbi, W. A.; Un, S.; Winkler, J. R.; Gray, H. B., Spectroscopy and reactivity of a photogenerated tryptophan radical in a structurally defined protein environment. *Journal of the American Chemical Society* **2003,** *125* (47), 14220-14221.

73. Weller, A.; Nolting, F.; Staerk, H., A Quantitative Interpretation of the Magnetic-Field Effect on Hyperfine-Coupling-Induced Triplet Formation from Radical Ion-Pairs. *Chemical Physics Letters* **1983,** *96* (1), 24-27.

74. Rodgers, C. T.; Norman, S. A.; Henbest, K. B.; Timmel, C. R.; Hore, P. J., Determination of radical re-encounter probability distributions from magnetic field effects on reaction yields. *Journal of the American Chemical Society* **2007,** *129* (21), 6746-6755.

75. Cintolesi, F.; Ritz, T.; Kay, C. W. M.; Timmel, C. R.; Hore, P. J., Anisotropic recombination of an immobilized photoinduced radical pair in a 50-mu T magnetic field: a model avian photomagnetoreceptor. *Chemical Physics* **2003,** *294* (3), 385-399.

76. Maeda, K.; Miura, T.; Arai, T., A practical simulation and a novel insight to the magnetic field effect on a radical pair in a micelle. *Molecular Physics* **2006,** *104* (10-11), 1779-1788.

77. Qin, S. Y.; Yin, H.; Yang, C. L.; Dou, Y. F.; Liu, Z. M.; Zhang, P.; Yu, H.; Huang, Y. L.; Feng, J.; Hao, J. F.; Hao, J.; Deng, L. Z.; Yan, X. Y.; Dong, X. L.; Zhao, Z. X.; Jiang, T. J.; Wang, H. W.; Luo, S. J.; Xie, C., A magnetic protein biocompass. *Nature Materials* **2016,** *15* (2), 217-226.

78. Nohr, D.; Franz, S.; Rodriguez, R.; Paulus, B.; Essen, L. O.; Weber, S.; Schleicher, E., Extended Electron-Transfer in Animal Cryptochromes Mediated by a Tetrad of Aromatic Amino Acids. *Biophysical Journal* **2016,** *111* (2), 301-11.

79. Zoltowski, B. D.; Vaidya, A. T.; Top, D.; Widom, J.; Young, M. W.; Crane, B. R., Structure of full-length Drosophila cryptochrome. *Nature* **2011,** *480* (7377), 396-U156.

80. Levy, C.; Zoltowski, B. D.; Jones, A. R.; Vaidya, A. T.; Top, D.; Widom, J.; Young, M. W.; Scrutton, N. S.; Crane, B. R.; Leys, D., Updated structure of Drosophila cryptochrome. *Nature* **2013,** *495* (7441), E3-E4.

81. Kao, Y. T.; Saxena, C.; He, T. F.; Guo, L. J.; Wang, L. J.; Sancar, A.; Zhong, D. P., Ultrafast dynamics of flavins in five redox states. *Journal of the American Chemical Society* **2008,** *130* (39), 13132-13139.

82. Posener, M. L.; Adams, G. E.; Wardman, P.; Cundall, R. B., Mechanism of Tryptophan Oxidation by Some Inorganic Radical-Anions - Pulse-Radiolysis Study. *Journal of the Chemical Society-Faraday Transactions I* **1976,** *72*, 2231-2239.

83. Immeln, D.; Weigel, A.; Kottke, T.; Lustres, J. L. P., Primary Events in the Blue Light Sensor Plant Cryptochrome: Intraprotein Electron and Proton Transfer Revealed by Femtosecond Spectroscopy. *Journal of the American Chemical Society* **2012,** *134* (30), 12536-12546.

84. Kutta, R. J.; Archipowa, N.; Johannissen, L. O.; Jones, A. R.; Scrutton, N. S., Vertebrate Cryptochromes are Vestigial Flavoproteins. *Scientific Reports* **2017,** *7*.

85. Magerl, K.; Stambolic, I.; Dick, B., Switching from adduct formation to electron transfer in a light-oxygen-voltage domain containing the reactive cysteine. *Physical Chemistry Chemical Physics* **2017,** *19* (17), 10808-10819.

86. Berndt, A.; Kottke, T.; Breitkreuz, H.; Dvorsky, R.; Hennig, S.; Alexander, M.; Wolf, E., A novel photoreaction mechanism for the circadian blue light photoreceptor Drosophila cryptochrome. *Journal of Biological Chemistry* **2007,** *282* (17), 13011-13021.

87. Shafaat, H. S.; Leigh, B. S.; Tauber, M. J.; Kim, J. E., Spectroscopic Comparison of Photogenerated Tryptophan Radicals in Azurin: Effects of Local Environment and Structure. *Journal of the American Chemical Society* **2010,** *132* (26), 9030-9039.

88. Conrad, K. S.; Manahan, C. C.; Crane, B. R., Photochemistry of flavoprotein light sensors. *Nature Chemical Biology* **2014,** *10* (10), 801-809.

89. Mataga, N.; Chosrowjan, H.; Taniguchi, S.; Tanaka, F.; Kido, N.; Kitamura, M., Femtosecond fluorescence dynamics of flavoproteins: Comparative studies on flavodoxin, its site-directed mutants, and riboflavin binding protein regarding ultrafast electron transfer in protein nanospaces. *Journal of Physical Chemistry B* **2002,** *106* (35), 8917-8920.

90. Brazard, J.; Usman, A.; Lacombat, F.; Ley, C.; Martin, M. M.; Plaza, P.; Mony, L.; Heijde, M.; Zabulon, G.; Bowler, C., Spectro-Temporal Characterization of the Photoactivation Mechanism of Two New Oxidized Cryptochrome/Photolyase Photoreceptors. *Journal of the American Chemical Society* **2010,** *132* (13), 4935-4945.

91. Liu, B.; Liu, H. T.; Zhong, D. P.; Lin, C. T., Searching for a photocycle of the cryptochrome photoreceptors. *Current Opinion in Plant Biology* **2010,** *13* (5), 578-586.

92. Banerjee, R.; Schleicher, E.; Meier, S.; Viana, R. M.; Pokorny, R.; Ahmad, M.; Bittl, R.; Batschauer, A., The signaling state of Arabidopsis cryptochrome 2 contains flavin semiquinone. *Journal of Biological Chemistry* **2007,** *282* (20), 14916-14922.

93. Immeln, D.; Schlesinger, R.; Heberle, J.; Kottke, T., Blue light induces radical formation and autophosphorylation in the light-sensitive domain of Chlamydomonas cryptochrome. *Journal of Biological Chemistry* **2007,** *282* (30), 21720-21728.

94. Zollitsch, T. M.; Jarocha, L. E.; Bialas, C.; Henbest, K. B.; Kodali, G.; Dutton, P. L.; Moser, C. C.; Timmel, C. R.; Hore, P. J.; Mackenzie, S. R., Magnetically sensitive radical photochemistry of non-natural flavoproteins. *Journal of the American Chemical Society* **2018**.

95. Huvaere, K.; Skibsted, L. H., Light-Induced Oxidation of Tryptophan and Histidine. Reactivity of Aromatic N-Heterocycles toward Triplet-Excited Flavins. *Journal of the American Chemical Society* **2009,** *131* (23), 8049-8060.

96. Muszkat, K. A.; Wismontskiknittel, T., Reactivities of Tyrosine, Histidine, Tryptophan, and Methionine in Radical Pair Formation in Flavin Triplet Induced Protein Nuclear Magnetic-Polarization. *Biochemistry* **1985,** *24* (20), 5416-5421.

97. Korvinson, K. A.; Hargenrader, G. N.; Stevanovic, J.; Xie, Y.; Joseph, J.; Maslak, V.; Hadad, C. M.; Glusac, K. D., Improved Flavin-Based Catalytic Photooxidation of Alcohols through Intersystem Crossing Rate Enhancement. *Journal of Physical Chemistry A* **2016,** *120* (37), 7294-7300.

98. Sichula, V.; Kucheryavy, P.; Khatmullin, R.; Hu, Y.; Mirzakulova, E.; Vyas, S.; Manzer, S. F.; Hadad, C. M.; Glusac, K. D., Electronic Properties of N(5)-Ethyl Flavinium Ion. *Journal of Physical Chemistry A* **2010,** *114* (46), 12138-12147.

99. Sakai, M.; Takahashi, H., One-electron photoreduction of flavin mononucleotide: Time-resolved resonance Raman and absorption study. *Journal of Molecular Structure* **1996,** *379*, 9-18.

100. Ghisla, S.; Mayhew, S. G., Identification and Properties of 8-Hydroxyflavin - Adenine-Dinucleotide in Electron-Transferring Flavoprotein from Peptostreptococcus-Elsdenii. *European Journal of Biochemistry* **1976,** *63* (2), 373-390.

101. Raibekas, A. A.; Fukui, K.; Massey, V., Design and properties of human D-amino acid oxidase with covalently attached flavin. *Proceedings of the National Academy of Sciences of the United States of America* **2000,** *97* (7), 3089-3093.

102. Aubert, C.; Vos, M. H.; Mathis, P.; Eker, A. P. M.; Brettel, K., Intraprotein radical transfer during photoactivation of DNA photolyase. *Nature* **2000,** *405* (6786), 586-590.

103. Moore, W. M.; Colson, S. D.; Spence, J. T.; Raymond, F. A., Photochemistry of Riboflavin .1. Hydrogen Transfer Process in Anaerobic Photobleaching of Flavins. *Journal of the American Chemical Society* **1963,** *85* (21), 3367-3372.

104. Holmstrom, B.; Oster, G., Riboflavin as an Electron Donor in Photochemical Reactions. *Journal of the American Chemical Society* **1961,** *83* (8), 1867-1871.